

Modelling and control for structural load mitigation of wind turbines

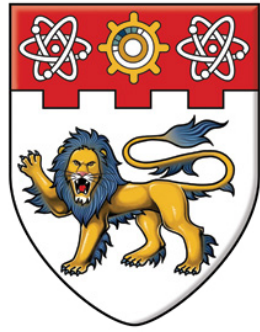
Girsang, Irving Paul

2016

Girsang, I. P. (2016). Modelling and control for structural load mitigation of wind turbines.
Doctoral thesis, Nanyang Technological University, Singapore.

<https://hdl.handle.net/10356/67010>

<https://doi.org/10.32657/10356/67010>



NANYANG
TECHNOLOGICAL
UNIVERSITY

**MODELLING AND CONTROL FOR STRUCTURAL
LOAD MITIGATION OF WIND TURBINES**

IRVING PAUL GIRSANG

SCHOOL OF MECHANICAL AND AEROSPACE ENGINEERING

2016

**MODELLING AND CONTROL FOR STRUCTURAL
LOAD MITIGATION OF WIND TURBINES**

IRVING PAUL GIRSANG

School of Mechanical and Aerospace Engineering

A thesis submitted to the Nanyang Technological University
in partial fulfillment of the requirement for the degree of
Doctor of Philosophy

2016

Abstract

The number of installed wind turbines have been steadily growing at an average annual rate of 17% globally for the past 5 years. In 2015 alone, 63 GW has been installed worldwide, which is 21% more capacity than that was installed in 2014. This has been possible by larger and taller wind turbines that allow for more energy capture. Further, such large turbines are found suitable for near-equator regions and now entering Asia, which saw 23% growth in installed capacity in 2015 from 2014. This trend marks the remarkable progress of wind energy industry and highlights several key challenges that need to be solved by both research and industrial communities in order to sustain and advance the growth.

To keep up with the trend of increasing turbine sizes and hence structural flexibility, it is important to ensure mitigation of its structural loads in order to keep the cost of wind energy low by lessening the maintenance requirements and improving the overall turbine reliability. As the saying goes, “wind energy is renewable but wind turbines are not”.

Two of the most flexible and costly wind turbine components are the blades and the drivetrain. Further, the downtime to replace the blades or the drivetrain components, in case of failure, ranges from 4 to 7 days, which can amount to huge loss of production.

Compared with upgrading the mechanical system to preserve the components’ lifetime, advanced control systems have been identified as more attractive and cheaper cost reducing strategies. Further, wind turbines as large flexible structures operating in uncertain environments fit nicely into the problem sphere of modern control engineering. Implementing sophisticated control strategies can assure safe and optimal operation in terms of load mitigation and power enhancement under a range of wind conditions. In this thesis, a number of novel controller designs are developed to mitigate fatigue loads on wind turbines’ blades and drivetrain. The controllers are designed to attenuate loads in ways that have not been paid much attention before and verified to yield superior

load attenuation as compared with the ones have been achieved so far.

A novel individual pitch controller (IPC) has been designed based on the knowledge of mitigated blade loads at a yaw misaligned condition. To ensure easy implementation, the proposed IPC is still to operate in the typical turbine configuration, in which the turbine is aligned with the wind direction. This thesis shows that the proposed IPC yield slight improvement in the power quality and significant reduction in the fatigue blade loads as compared with that of baseline industrial-standard collective pitch controller (CPC) and IPC at various turbulent wind conditions. Compared with the baseline CPC, the proposed controller is shown to contribute at least a 31.54% reduction in the blade out-of-plane fatigue load

To mitigate the drivetrain loads, a stochastic disturbance accommodating controller (SDAC) has been designed to regulate the collective blade pitch angle to stabilize the turbine that is otherwise unstable using the previous designs of disturbance accommodating controller (DACs) due to the unmodelled dynamic coupling between the drivetrain and other turbine components. The proposed SDAC is shown to improve the power quality up to 20.8%, while resulting in lower drivetrain load up to 22.5% as compared with the industrial-standard CPC.

A new integrated wind turbine model that couples high-fidelity aerodynamic, structural, drivetrain and electrical models is proposed. This new integration allows for consideration of the grid conditions, including various mitigation responses to the grid, in calculating the wind turbine loads. Essential insights can also be gained into the drivetrain dynamics, particularly in terms of predicting transient loadings and possible resonant excitations. The integrated model can save the design costs by allowing dynamic interactions to be taken into account before assembling the hardware. In this thesis, the case of choosing flexible drivetrain components to minimize the transmitted loads on the gearbox are highlighted.

The high-fidelity wind turbine model has enabled the design and validation of various controllers focusing on mitigating the internal drivetrain loads. A new controller has been designed that avoids resonance load of wind turbine drivetrain. The controller introduces additional virtual inertia through the generator torque to shift the eigenfrequency of the drivetrain only when it passes through its inherent resonance. Obviating resonance directly improves the power quality by mitigating the fluctuations in the output power. Another new controller has been designed to mitigate the drivetrain load when the grid frequency significantly drops. The new controller is

based on the concept of damper harmonic oscillator to alleviate the transient drivetrain vibrations during such grid event.

To God be the glory, great things He hath done.

Acknowledgements

I would like to express my sincere gratitude to my advisor, Dr. Jaspreet Singh Dhupia, who is now at the University of Auckland. Without him, the works in this thesis could hardly have been done. He has been the most instrumental person for my research achievements. He provided guidance, advice, expertise, encouragement and support, which are invaluable for the completion of my study.

My deep gratitude to Asst. Prof. Tegoeh Tjahjowidodo for his kind, patient, yet persistent push for me to complete the critical last phase of my thesis.

I would like to greatly and gratefully acknowledge the scholarship from the Energy Innovation Programme Office, which has allowed me to pursue my doctoral study.

My gratitudes to Dr. Eduard Muljadi and Dr. Mohit Singh from the National Renewable Energy Laboratory, and Prof. Lucy Y. Pao from the University of Colorado Boulder for their involvement and support in this research, especially during my internship at the National Wind Technology Center.

I would also like to address my gratitude to the people of the Energy Research Institute at NTU: Dr. Srikanth Narasimalu, James Moses, and Mary Ann for allowing me to present my works in the institute, also for many of their kind help and valuable inputs.

I would like to thank my kind friends: Hong Liu, Jidong, Aaron, Liza, Darryl, Kristo, Indra, Kevin, Eric, Jemmy, Yulius, and Chatharin, for giving me support, companionship, and encouragement along this exciting journey.

Thank you to The Blue Circle Pte. Ltd. for the opportunity to change the world one turbine at a time and for giving me some time off to work on my thesis.

Finally, I would like to say heartfelt thank you to my parents and younger sister for their continuous prayers, love, and care throughout my life.

Table of Contents

List of Figures	xii
List of Tables	xvii
1 Introduction	1
1.1 Motivations	1
1.2 Objectives	4
1.3 Contributions of the Thesis	6
1.4 Organization of the Thesis	7
2 Basics on Modelling Wind Turbine Loads	9
2.1 Introduction	9
2.2 FAST Aeroelastic Tool	9
2.2.1 Wind Inflow	10
2.2.2 Aerodynamics	11
2.2.3 Structural Dynamics	12
2.2.4 MATLAB/Simulink Module	12
2.2.5 Linearization of Wind Turbine Model	13
2.3 Turbine Types	14
2.4 Generator Types	14
2.5 Control Objectives	17
2.6 Damage Equivalent Load	21
3 Pitch Controller to Mitigate Load due to Unmodeled Dynamics	23
3.1 Introduction	23

3.2	Turbine and Actuator Models	24
3.3	Collective Pitch Controllers	25
3.3.1	Baseline GSPI Controller	25
3.3.2	SDAC	26
3.4	Simulation Results and Discussions	30
3.4.1	Simulation with Step Wind Inputs	30
3.4.2	Simulation with Turbulent Wind Inputs	31
3.5	Chapter Conclusions	37
4	Pitch Controller to Mitigate Load considering Yaw Misalignment	39
4.1	Introduction	39
4.2	Baseline Pitch Controllers	40
4.3	Effects of Yaw Misalignment	41
4.4	Proposed Controller Design	45
4.5	Simulation Results	50
4.5.1	Speed regulation	52
4.5.2	Structural loads	55
4.6	Chapter Conclusions	64
5	Torsional Models of Wind Turbine Drivetrain	65
5.1	Introduction	65
5.2	Model Overview	66
5.3	Five-mass Model of Drivetrain	67
5.4	Two-mass Model of Drivetrain	68
5.5	Pure Torsional Model of Gearbox with Constant Meshing Stiffness	68
5.5.1	Parallel Gear Stage	69
5.5.2	Planetary Gear Stage	71
5.6	Eigenfrequency Analysis and Validations	71
5.6.1	Eigenfrequencies of Purely Torsional Gearbox Model	71
5.6.2	Eigenfrequencies of Overall Drivetrain Model	73
5.7	Model Integration with FAST	76

5.8	Simulation Results	78
5.8.1	Transient Response due to Wind Excitation	79
5.8.2	Transient Response Resulting From Grid Excitation	80
5.9	Chapter Conclusions	83
6	Torque Controller to Mitigate Load due to Resonance	85
6.1	Introduction	85
6.2	Campbell Diagram	85
6.3	Controller Designs	86
6.3.1	Baseline SDC	87
6.3.2	Virtual Inertia Controller (VIC)	88
6.4	Simulation Results	89
6.5	Chapter Conclusions	93
7	Torque Controller to Mitigate Load while Providing Inertial Response	95
7.1	Introduction	95
7.2	Generator Model	96
7.3	Torque Controller for Inertial Response	97
7.4	Structural Loads due to Inertial Response	100
7.5	Chapter Conclusions	105
8	Concluding Remarks	107
8.1	Thesis Conclusions	107
8.2	Recommendations	110
	List of Publications	125

List of Figures

1.1	Trend of sizes and rating of installed WTs, reproduced from [3].	2
1.2	WT in the midst of vertical wind shear.	3
1.3	Failure characteristics of WT components	4
2.1	Schematic of interactions among WT components.	10
2.2	TurbSim-generated wind field grids, reproduced from [13].	11
2.3	Relationship between mean wind velocity and its standard deviation for IEC wind classification.	11
2.4	Turbulent wind with mean hub-height wind velocity of 18 m/s with turbulence classes (a) A and (b) C.	12
2.5	Open-loop Simulink model for simulating the FAST nonlinear WT.	13
2.6	Schematic of type 1 WTs.	15
2.7	Schematic of type 2 WTs.	15
2.8	Schematic of type 3 WTs.	16
2.9	Schematic of type 4 WTs.	16
2.10	Typical power curve of type 3 WT.	18
2.11	Power coefficient of a type 3 WT.	19
2.12	Schematic of the baseline CPC.	19
2.13	Motions of WT components from (a) front and (b) side views.	21
3.1	Two-mass model of WT drivetrain	24
3.2	Schematic for simulation using GSPI controller.	26
3.3	Schematic for simulation using SDAC.	29

3.4	Deterioration in system responses for $\mathbf{Q} = \mathbf{0}$ (a) with ideal (limitless) pitch actuator and (b) with actual pitch actuator.	32
3.5	Noisy input and output responses due to large \mathbf{Q}	33
3.6	Similar generator speed responses of GSPI and SDAC after tuning the \mathbf{Q}	34
3.7	Estimated and actual wind velocity of SDAC.	35
3.8	Performance comparisons between GSPI and SDAC under turbulent wind.	36
4.1	Schematic of the baseline IPC.	40
4.2	Top view of wind shear and yaw misalignment on WT in Fig. 1.2.	42
4.3	Simulated blade OOP loads under combined influences of wind shear and yaw misalignment for the baseline CPC: (a) peak-to-peak range (b) normalized peak-to-peak range.	43
4.4	Simulated blade OOP loads under class C turbulent winds with different mean wind velocities.	44
4.5	Designed closed-loop eigenvalues based on lower-order WT model (4 DOFs) and actual closed-loop eigenvalues based on fully flexible WT model (16 DOFs).	49
4.6	Bode plots from the disturbances to the components of blade-root OOP bending moment under the designed MIMO IPC.	50
4.7	Gain-scheduling of the proposed controller.	51
4.8	Back-calculation scheme for the proposed controller.	51
4.9	Comparison of the controllers in term of RMS generator speed error at various (a) mean wind velocities and (b) turbulence intensities.	53
4.10	Comparison of the controllers in term of maximum generator speed error at various (a) mean wind velocities and (b) turbulence intensities.	54
4.11	Comparison of the DEL of blade-root OOP bending moment of blade 1 at various (a) mean wind velocities and (b) turbulence intensities.	56
4.12	Power spectral density (in Nm) of a blade OOP load at 18 m/s (5%).	57
4.13	Power spectral density (in Nm) of a blade OOP load at 18 m/s (5%) around the WT rotational speed.	58

4.14 Comparison of the DEL of blade-root IP bending moment of blade 1 at various (a) mean wind velocities and (b) turbulence intensities.	59
4.15 Comparison of the DEL of tower-base FA at various (a) mean wind velocities and (b) turbulence intensities.	61
4.16 Power spectral density (in Nm) of a tower-base FA load at 18 m/s (C).	62
4.17 Comparison of the DEL of tower-base SS at various (a) mean wind velocities and (b) turbulence intensities.	63
4.18 Power spectral density (in Nm) of a tower-base SS load at 20 m/s (C).	64
5.1 Five-mass model of WT drivetrain built in Simscape/SimDriveline.	67
5.2 (a) Parallel gear stage, (b) dynamic model representation, and (c) model representation in Simscape/SimDriveline.	69
5.3 Planetary gear stage with 3 planet gears.	70
5.4 Torsional model of planetary gear stage with M planet gears.	70
5.5 Input-output configuration on SimDriveline model for eigenfrequency analysis. . . .	72
5.6 FRF of three-planet planetary gear stage for the gearbox presented in [75].	72
5.7 Transient rotor speed and torque from field measurements during generator startup. .	74
5.8 Transient rotor speed and torque from field measurements during generator upshift. .	75
5.9 Transient rotor speed and torque from field measurements during braking event. . .	75
5.10 Integration of the SimDriveline drivetrain model with FAST.	77
5.11 Rotor speed response at wind velocity of 7.25 m/s.	78
5.12 Transient response comparison of the rotor torque.	78
5.13 Steady-state response comparison of the rotor torque.	79
5.14 Generator torque excitations resulting from a voltage drop on the grid.	81
5.15 (a) Transmitted loads onto the gears because of grid excitation and (b) its frequency components.	81
5.16 Transmitted loads onto the second parallel gear stage under various HSS stiffness values and (b) its frequency components.	82
6.1 Campbell diagram of the GRC drivetrain with respect to the blade-pass frequency and its harmonics.	86

6.2	Control schematic of the DFIG rotor side converter to mitigate resonance load. . . .	87
6.3	Schematic implementation of SDC.	87
6.4	Schematic implementation of VIC.	88
6.5	Sinusoidal wind excitation at varying frequency.	89
6.6	Controller comparisons in terms of transmitted drivetrain load under sinusoidal wind excitation: (a) without controller and with SDC, (b) without controller and with VIC, and (c) with SDC and VIC.	90
6.7	Drivetrain responses under constant wind velocity of 7.25 m/s: (a) WT rotor speed, (b) generator output power, and (c) drivetrain torsional load.	91
6.8	Drivetrain responses under constant wind velocity of 7.25 m/s: (a) WT rotor speed, (b) generator output power, and (c) drivetrain torsional load.	92
7.1	DFIG model taking measured grid frequency input.	96
7.2	A frequency dip measured at Western Interconnection.	96
7.3	Torque controller for the rotor side converter of DFIG.	97
7.4	Speed response of type 3 WT at different tuning parameters.	99
7.5	Total power delivered to the grid at different tuning parameters.	99
7.6	Generator torque and transmitted gear load during the inertial response.	100
7.7	Loads on the tower-top during the inertial response.	101
7.8	Coupling between drivetrain torque and tower-top SS moment, adapted from [17]. .	101
7.9	Loads on the tower-base during the inertial response.	102
7.10	Generator responses in terms of torque and output power during inertial response with and without damped oscillator.	103
7.11	Gear transmitted load during inertial response with and without damped oscillator.	103
7.12	Parameters of the compensating torque based on damped harmonic oscillator. . . .	105
8.1	Contributions of the thesis: integration of drivetrain model as well as designs of pitch and generator torque controllers.	108

List of Tables

2.1	Key Specifications of NREL 5-MW Reference WT	14
2.2	Key Specifications of GRC WT	14
2.3	Slopes of the SN curves	22
5.1	Parameters of the 750-kW DFIG	66
5.2	Parameters of GRC Drivetrain	67
5.3	Comparisons with Eigenfrequencies Reported in [75]	73
5.4	Eigenfrequencies of GRC Drivetrain with Torsional Gearbox Model	74
7.1	DELs of WT's Components	104

Chapter 1

Introduction

1.1 Motivations

With global climate changing, people have become much more interested in renewable energy and wind energy is one of the most cost-competitive ones. Recent research has indicated that the wind energy industry has the ability to produce electricity in the price range of 5-8 cents (in USD) per kWh, which is comparable with the cost of some fossil fuel electricity sources [1]. This remarkable trend has led to wind energy playing an increasingly important role in the energy mix. Nowadays, the wind power generation capacity all over the world is enough to cover 4% of the global electricity demand [2].

In recent years, wind energy industry has grown substantially and so have the size and rating of the manufactured wind turbines (WTs), as shown in Fig. 1.1. The growth of these WTs has been driven by more captured energy from larger rotor swept area and higher wind velocity at higher altitude as their size increases. To this date, WTs have become the largest rotating structures in the world [4], making the entire process related to WTs (i.e., design, installation, operation and maintenance) dealing with very large and flexible components. To further decrease the cost of wind energy, emphasis on load mitigation has to be included in the design and integration of WT components. Reducing the structural loads of the WT will significantly decrease the cost of wind energy by lessening the maintenance requirements and improving the overall WT reliability.

Implementing sophisticated control strategies can assure safe and optimal operation in terms of load mitigation and power enhancement under a range of wind conditions. Compared with upgrading the mechanical system to preserve the WT lifetime, advanced control systems are more attractive and cheaper cost reducing strategies [5]. Using advanced control strategies to make more

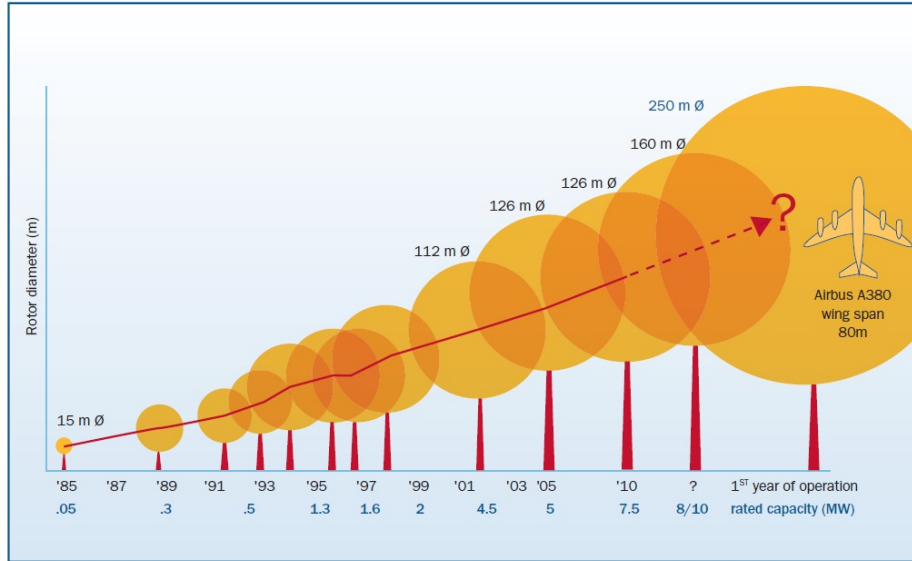


Figure 1.1: Trend of sizes and rating of installed WT's, reproduced from [3].

reliable WT's and upgrade their performance can increase the quality of the power generation and reduce the downtime as well as the operation and maintenance costs. Further, WT's as large flexible structures operating in uncertain environments fits nicely into the problem sphere of advanced control engineering.

The WT blades are the primary components that capture the available wind energy and convert it into rotational kinetic energy. However, as the blades become longer to increase the area of energy capture, they become more flexible and suffer from higher structural loads amidst the vertical wind shear. The vertical wind shear is a common atmospheric phenomenon wherein the wind velocity increases with height, as illustrated in Fig. 1.2. Therefore, each blade experiences cyclic loading as it rotates in the rotor plane that is being exposed to this kind of wind variation. Further, in cases where the increase in WT rotor is more than that in hub-height, vertical wind shear across larger rotor swept area creates higher inflow variations resulting in increasing load variations on the longer and more flexible blades (i.e., higher fatigue loads).

Emphasis on blade load mitigation, especially in high wind velocities, has been included in the design of modern WT controllers. However, in all designs, the wind is assumed to have no misalignment with respect to the rotor plane. While it has been shown that yaw misalignment at certain angular positions can mitigate the blade load variations [6], it will be beneficial to include the benefit of yaw misalignment on the design of WT controllers to further mitigate the blade loads.

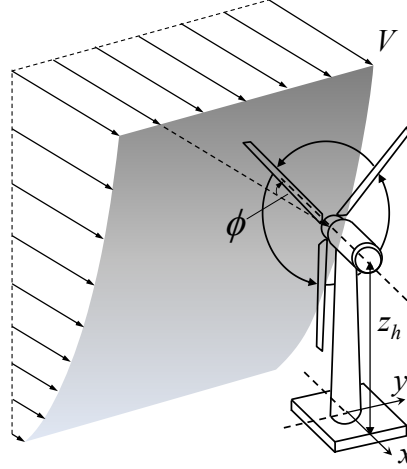


Figure 1.2: WT in the midst of vertical wind shear.

The drivetrain is the subsequent assembly of components that transmit the kinetic energy and convert it to electric energy. Similar to the blades, larger WT structures yield more flexible drivetrains that lead to higher failure rates due to fatigue. The most comprehensive study to date on the long term reliability and availability of WTs reveals that failures in drivetrain components as well as the blades are among the top four factors affecting the WT availability, as shown in Fig. 1.3 [7,8]. The drivetrain and blade failures are sources of considerable costs because they often require unplanned corrective maintenance leaving the WT out of service for a long time.

Besides being exposed to the uncertain aerodynamic environment on one end, the WTs are increasingly exposed to the uncertainties in the power grid on the other end. As the number of installed WTs increases to raise the contribution of wind energy to meet the overall energy demand, it brings up the roles of WTs in maintaining the stability and reliability of the power grid. This is evident from the continuing revisions to the existing grid codes developed by system operators all over the world [9–11]. One of such revisions requires WTs to provide ancillary services to the power system to help maintaining the grid frequency. Advancements in state-of-the-art technologies in the forms of high-efficiency generators, power electronics, and especially modern controllers have enabled WTs to provide the services. However, the resulting drivetrain loadings have not been well considered in the controller designs.

Aeroelastic tools have been developed to model and simulate the dynamics of WTs in response to various operating conditions and controller designs. While the structural model in these tools contains sufficient detail to accurately describe the dynamic loads of the blades and tower, the

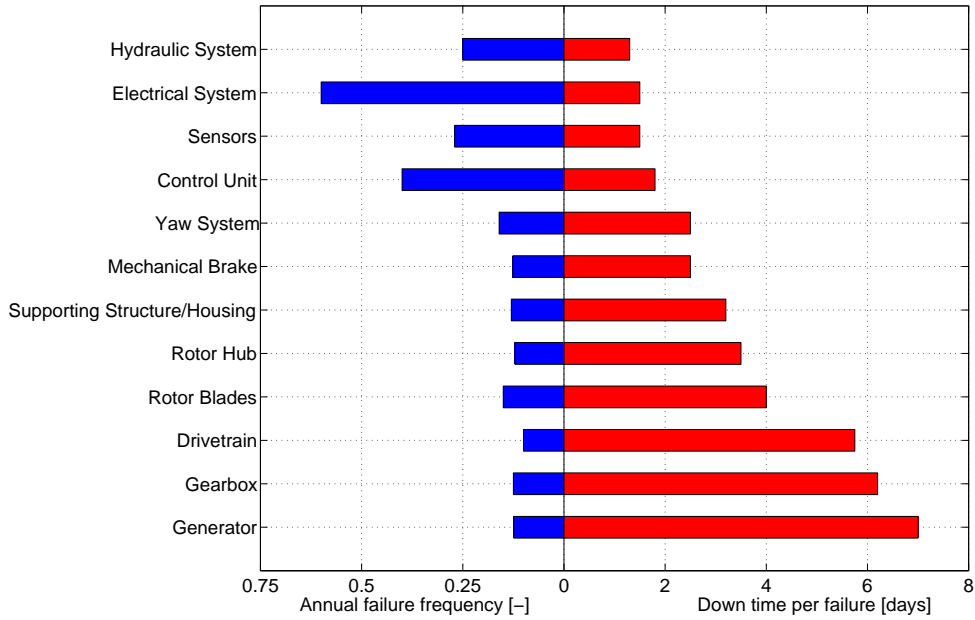


Figure 1.3: Comparison of WT components according to its annual failure rates and its down time per failure [8].

drivetrain model is reduced to a two degree of freedom (DOF) system, resulting in restricted detail in describing various configurations and complex dynamic behaviors of different drivetrain designs. Although dynamic models of WT drivetrain with various levels of fidelity have been developed, they have mostly been used in a decoupled framework; thus, providing very little insights on the dynamic interactions between the drivetrain and other WT components. Insights into the drivetrain internal dynamics in relation to the overall WT dynamic response amidst realistic wind and grid conditions are prominent in designing controllers to mitigate the WT loads due to wind and grid excitations.

1.2 Objectives

In order to fulfill the identified needs due to the progressively increasing size and flexibility of WT structures, this thesis comprises investigations on controller designs and performance validations to mitigate the WT blade and drivetrain loads. This thesis aims to contribute towards more cost-efficient WTs through load mitigating controllers so that the WTs components need not to be over-dimensioned and their effective lifetime can be preserved. The blade and drivetrain loads are the WT structural loads considered in this thesis. Each of these loads are discussed separately in

this thesis according to the operating region of the WT.

The thesis does not investigate WT loads under extreme wind conditions (e.g., sudden extreme gust, typhoon, etc.). Extreme event controllers (EECs) are another active area of research. The main function of EECs are to accurately identify the occurrence of extreme event(s) and then to bring the WT into parking (i.e., to stop the turbine) as quickly and safely as possible.

The key objectives of this thesis are as follow

- To design collective pitch controller (CPC) to mitigate the drivetrain loads

At high wind velocities above the rated wind velocity, the blades are pitched to ensure that aerodynamic power is being extracted at the WT rating while the generator torque is kept constant at its rated value. Because the blade pitch angle directly affects the aerodynamic torque transmitted to the drivetrain, it is important to design the CPC so that the aerodynamic torque does not excite the unstable modes of the WT system.

- To design individual pitch controller (CPC) to mitigate the blade loads

CPCs are inherently not able to take into account the blade load variations caused by the vertical wind shear. Therefore, individual pitch controller (IPC) is required. In all IPC designs so far, the wind field has been assumed to have no misalignment with respect to the rotor plane. It will be beneficial to integrate the knowledge of reduced blade load variation at a yaw misaligned condition to design a better load-mitigating IPC.

- To integrate high-fidelity drivetrain model with high-fidelity aerodynamic, structural, and electrical models

For wind velocities below the rated wind velocity, the WT operates to capture as much wind energy as possible. At such operating conditions, there is an optimum WT rotor speed, which is a function of the oncoming wind velocity, that ensures maximum energy capture. This optimum WT rotor speed is achieved by controlling the generator torque while the blade pitch angles are fixed at the optimum value. While achieving the desired optimum speed, the WT drivetrain is being exposed to various aerodynamic excitations on one hand and grid excitations on the other. To gain insights on the internal drivetrain dynamics under such condition, a high-fidelity WT model is required.

- To design generator torque controller to mitigate resonance load

Within the range of WT's operating speed, there can be a rotational speed in which the WT undergoes resonant vibrations as the aerodynamic excitation matches an eigenfrequency of the drivetrain. The generator torque can be controlled to alleviate such condition. While the controller is commonly designed to add damping to the drivetrain, significant loads are still exerted on the damped eigenfrequency. Therefore, an alternative design is needed.

- To design generator torque controller to mitigate transient load during inertial response

To allow WTs to provide the inertial response, many works have proposed the implementation of supplementary control loops so that additional energy from the kinetic energy stored in the rotating mass of the WT is injected to the grid during a frequency drop. However, the inertial response excites transient vibrations on the WT structures. Therefore, a controller can be designed to alleviate the additional costs of inertial response.

1.3 Contributions of the Thesis

The main contributions of this thesis are summarized below along with their associated publications:

- A stochastic disturbance accommodating controller (SDAC) to regulate the collective blade pitch angle to stabilize the WT that is otherwise unstable due to the unmodelled dynamic coupling between the drivetrain and other WT components. The proposed SDAC is shown to yield output power closer to the rated value amidst turbulent wind while resulting in lower drivetrain load as compared with the industrial standard PI controller [J1, C1, C3].
- A new multi-input-multi- output (MIMO) IPC that is designed based on the knowledge of mitigated blade load at a yaw misaligned condition. The proposed IPC is still to operate in the typical turbine configuration, in which the WT is aligned with the wind direction. It has been shown that the proposed IPC yields lower fatigue blade loads as compared with that of some baseline CPC and IPC at various turbulent wind conditions [J4, C5, C6].
- A new integrated WT model coupling high-fidelity aerodynamic and structural models, high-fidelity drivetrain model, and high-fidelity electrical models in MATLAB/Simulink environment. The model can simulate WT responses under different wind and grid conditions with

essential insights into the internal drivetrain dynamics, particularly in terms of predicting transient loadings and possible resonant excitations. The model can be used to design the various flexible components of the drivetrain so that transmitted loads on the gearbox can be reduced [J3, C2, T1].

- A new controller that avoids resonance load of WT drivetrain due harmonic excitations. The controller introduces additional virtual inertia in the generator torque to shift the eigenfrequency of the drivetrain only when it passes through its inherent resonance. Beyond the characteristic resonant region, there is no compensating torque required and the maximum power capture controller remains during normal operation. It solves a drawback of typical damper controller that induces additional load at another operating condition besides resonance [J2, T1].
- A new controller to mitigate the drivetrain load during inertial response. As the kinetic energy stored in the rotating mass of the WT must be injected to the grid during a frequency drop, significant fatigue loadings are experienced by the WT drivetrain. The controller is designed based on the concept of damper harmonic oscillator to alleviate the transient drivetrain vibrations. The high-fidelity integrated WT model have enabled accurate design of the harmonic oscillator [J5, C4].

The publications indicated above are listed in Appendix A.

1.4 Organization of the Thesis

This thesis comprises nine chapters. Chapter 2 describes the different components of the WT model used for simulations and investigations. It covers the models of the wind fields, WT structures, and generators. WT operating regions, based on which the control objectives are set, are also outlined. Performance metrics in the form of damage equivalent load (DEL) of WT structural components is defined at the end of this chapter.

The first part of this thesis is made of Chapters 3 and 4, which present the design of pitch controllers for operations above the rated wind velocity. Chapter 3 presents the design of CPC to mitigate the drivetrain load due to the unmodelled dynamic coupling between the drivetrain and

other WT components. The controller is designed based on the principle of disturbance accommodating control. Works on the disturbance accommodating controller designs for WT applications are reviewed in this chapter. Chapter 4 presents the design of individual pitch controller (IPC) to mitigate the blade load variations amidst vertical wind shear. The controller design considers the benefit of yaw misalignment, which has not been considered in the previous designs of IPC. The effectiveness of each proposed controller in comparison with some baseline CPCs and IPCs is presented at the end of each chapter.

The second part is made of Chapters 5 to 7, which present the design of generator torque controllers for operation below the rated wind velocity. Chapter 5 presents the design of high-fidelity torsional model of WT drivetrain. Compared with other gearbox and drivetrain models reviewed in this chapter, the presented model is coupled with high-fidelity WT structure and generator models, resulting in high-fidelity integrated WT model that is helpful in design considerations. Eigenfrequencies of the presented model are validated in this chapter against the experimental data, field measurement data as well as reported values of other works. Chapter 6 presents the generator torque controller that injects additional inertia to the drivetrain so that the closed-loop eigenfrequency is shifted and resonance is avoided. The effectiveness of the presented controller is compared with the widely used stress damper controller. Chapter 7 presents the generator torque controller to mitigate the drivetrain load while the WT is providing the recently required operation of inertial response. The inertial response requirement results in torque spike that exerts loads on various WT components investigated in this chapter. Such loads have not been much considered and this chapter proposes a damped harmonic oscillator to alleviate such issues.

Finally, Chapter 8 summarises the general conclusions of this thesis, highlights its main contributions, and proposes future research directions.

Chapter 2

Basics on Modelling Wind Turbine Loads

2.1 Introduction

This chapter describes the existing knowledge on modelling structural loads of a WT. Figure 2.1 explains the interactions among the WT components and multi-disciplinary approach required to study WT dynamics. The contribution of this thesis (i.e., integration of drivetrain dynamic model and designs of WT controllers) are highlighted in bold, italic, and underlined labels. Those areas will be elaborated in the following chapters of this thesis. Wind turbines operate at distinct regions according to the oncoming wind velocity. The WT structural loads at each operating region, which is quantified in terms of damage equivalent loads (DELs) of the structure, highly depend on the implemented controller and type of utilized generator. The operating regions, control systems, generator types, and DELs are also discussed in this chapter.

2.2 FAST Aeroelastic Tool

The U.S. National Renewable Energy Laboratory (NREL) sponsored the development, verification, and validation of various computer-aided-engineering (CAE) tools for prediction of WT loads and responses. One tool based on aeroelasticity, which is the study of interactions among the inertial, elastic, and aerodynamic forces when an elastic body is exposed to a fluid flow, stands out. The tool named FAST, which stands for Fatigue, Aerodynamics, Structures, and Turbulence, was developed through a subcontract between NREL and Oregon State University [12].

FAST has been certified in 2005 by an established independent certification body, through successful extensive field tests, to be suitable for “calculation of onshore wind turbine loads for

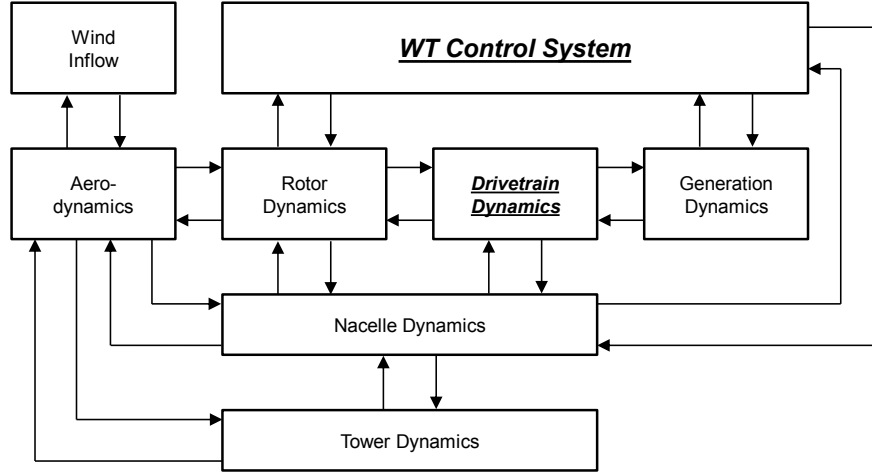


Figure 2.1: Schematic of interactions among WT components.

designs” [13]. This certification support the use of FAST as a virtual WT to simulate WT loads under various design considerations, including the controller designs. This has made FAST a well-known and widely used simulator for predicting both the extreme and fatigue loads of two- and three-bladed horizontal axis WTs.

2.2.1 Wind Inflow

The stochastic wind fields can be differentiated based on the mean wind velocity at the hub-height and the turbulence model used. TurbSim was used to generate wind input files representing turbulent wind fields used for simulations carried out in this study [14]. TurbSim uses a statistical model (e.g., IEC Kaimal spectral model) to numerically simulate the time series of three component wind velocity vectors at points in a two-dimensional vertical rectangular grid, as shown in Fig. 2.2. The TurbSim wind field grids in this thesis were generated at 20 Hz. The wind conditions march forward in a frozen field toward the WT; that is, the vertical grids do not evolve with time.

Turbulence intensity (TI) is a measure of the turbulence level in a wind field and is defined as

$$TI = \frac{V_{\text{std}}}{V_{\text{mean}}} \quad (2.1)$$

where V_{std} is the standard deviation of the wind velocity and V_{mean} is the mean wind velocity. Higher TI denotes high level of turbulence. International Electrotechnical Commission (IEC) divides the turbulent wind into three classes, where turbulence classes A and C have the highest and lowest

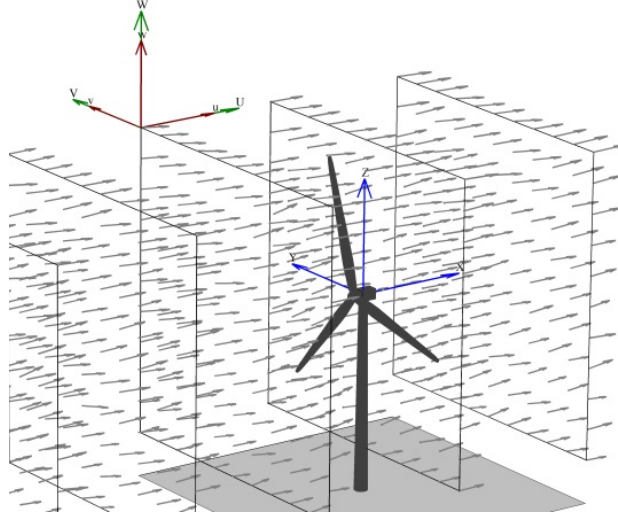


Figure 2.2: TurbSim-generated wind field grids, reproduced from [13].

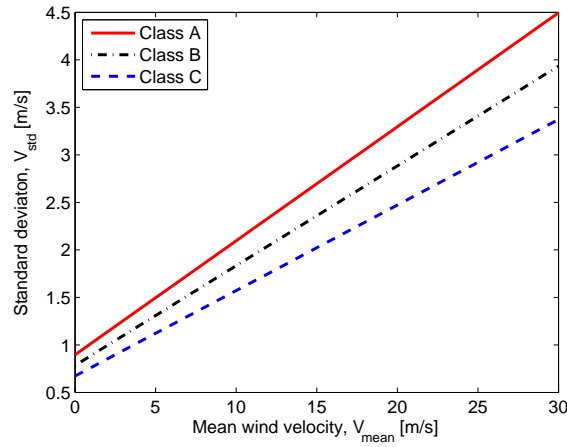


Figure 2.3: Relationship between mean wind velocity and its standard deviation for IEC wind classification.

turbulence intensities, as shown in Fig. 2.3 [15]. As examples, 10-minute longitudinal hub-height wind velocities generated using TurbSim with mean hub-height wind velocity of 18 m/s are shown in Fig. 2.4.

2.2.2 Aerodynamics

FAST is interfaced with the AeroDyn subroutine package to model and simulate the aerodynamic forces acting along the blades and tower under various wind conditions. AeroDyn contains an important model for dynamic stall based on the semi-empirical Beddoes-Leishman model, which is

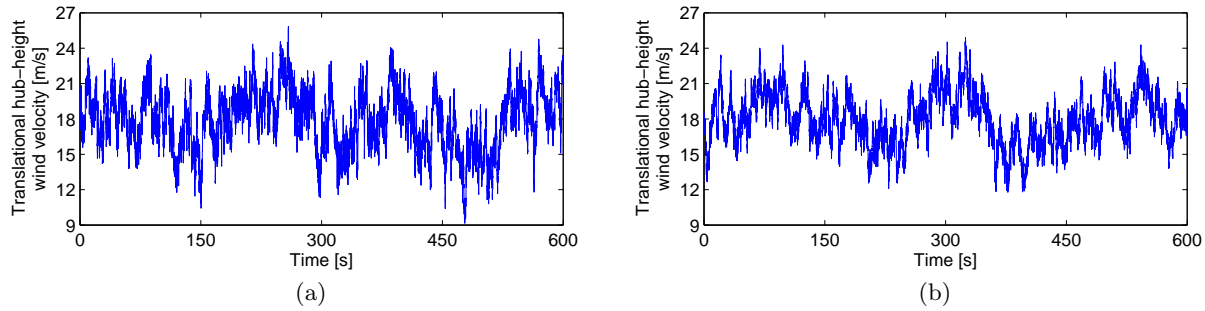


Figure 2.4: Turbulent wind with mean hub-height wind velocity of 18 m/s with turbulence classes (a) A and (b) C.

critical to accurately model yawed inflow conditions [16].

2.2.3 Structural Dynamics

FAST models a WT as a combination of rigid and flexible bodies. The rigid bodies are the ground, nacelle, hub, and optional tip brakes (point masses) on the blade. The flexible bodies include blades, tower, and drivetrain. The model connects these bodies with several degrees of freedom (DOFs). These include tower bending, blade bending, nacelle yaw, rotor teeter, rotor speed, and drivetrain torsional flexibility. The flexible tower has two modes each in the fore-aft and side-to-side directions. Each flexible blade has two flapwise modes and one edgewise mode. Each of these flexibilities can be turned on or off individually in the analysis by simply setting a switch in the input data file.

2.2.4 MATLAB/Simulink Module

The nonlinear FAST WT model is implemented in the MATLAB/Simulink environment as an S-function in the `.mex32` format shown in Fig. 2.5. The required WT parameters for running the FAST S-function is loaded from a predefined input `.fst` file. FAST uses Kane's method to set up equations of motion that are solved numerically using the assigned MATLAB/Simulink solver, such as fixed-step solvers: `ode1` (Euler), `ode4` (Runge-Kutta), or variable-step solvers: `ode45` (Dormand-Prince). Implementation of FAST in the MATLAB/Simulink environment allows the WT models to be versatily enhanced with high-fidelity drivetrain and/or generator models as well as coupled with variety of controller designs.

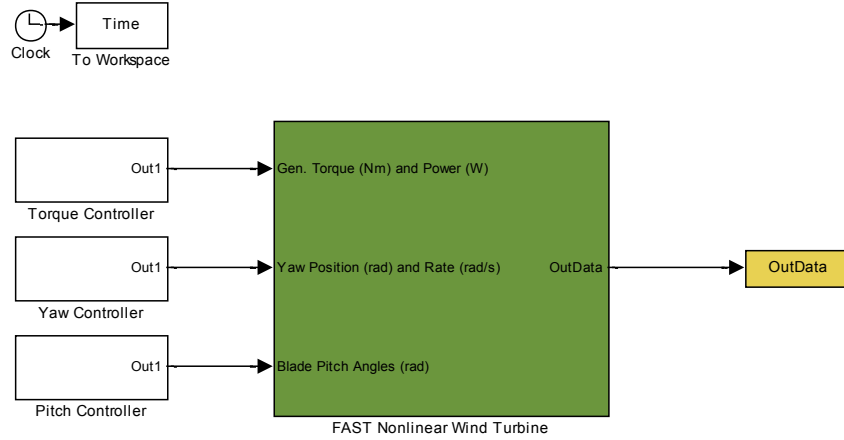


Figure 2.5: Open-loop Simulink model for simulating the FAST nonlinear WT.

2.2.5 Linearization of Wind Turbine Model

FAST can be used to linearize a WT at various operating conditions to obtain plant models required for controller design. FAST linearizes the WT at a predefined number of equally spaced rotor azimuth (i.e., rotor angular position) θ in the form

$$\Delta \dot{\mathbf{x}}_F = \mathbf{A}_F(\theta) \Delta \mathbf{x}_F + \mathbf{B}_F(\theta) \Delta \mathbf{u}_F + \mathbf{B}_{d,F}(\theta) \Delta \mathbf{u}_{d,F} \quad (2.2)$$

$$\Delta \mathbf{y}_F = \mathbf{C}_F(\theta) \Delta \mathbf{x}_F + \mathbf{D}_F(\theta) \Delta \mathbf{u}_F + \mathbf{D}_{d,F}(\theta) \Delta \mathbf{u}_{d,F} \quad (2.3)$$

where $\mathbf{A}_F, \mathbf{B}_F, \mathbf{B}_{d,F}, \mathbf{C}_F, \mathbf{D}_F, \mathbf{D}_{d,F}$ are azimuth-dependant state space model matrices, \mathbf{x}_F contains the WT states, \mathbf{u}_F is the control input to the WT, $\mathbf{u}_{d,F}$ is the disturbance input, \mathbf{y}_F is the measured output, and Δ represents the perturbation from the operating condition (i.e., $\mathbf{x} = \Delta \mathbf{x} + \mathbf{x}^{\text{op}}$).

The states in Eqs. (2.2)-(2.3) depend on the assumed DOFs of the WT model. In other words, the controller can be designed based on a plant model that assumes flexibility of certain parts of the WT while other parts are considered rigid.

The state-space model of Eq. (2.2) can be averaged to give the linear time invariant (LTI) model of the system, which is widely used for controller design

$$\Delta \dot{\mathbf{x}}_F = \mathbf{A} \Delta \mathbf{x}_F + \mathbf{B} \Delta \mathbf{u}_F + \mathbf{B}_d \Delta \mathbf{u}_{d,F} \quad (2.4)$$

$$\Delta \mathbf{y}_F = \mathbf{C} \Delta \mathbf{x}_F + \mathbf{D} \Delta \mathbf{u}_F + \mathbf{D}_d \Delta \mathbf{u}_{d,F} \quad (2.5)$$

Table 2.1: Key Specifications of NREL 5-MW Reference WT

Parameters	Values
Configuration, rating	3 blades, 5 MW
Gearbox, overall ratio	Multi-stage, 97
Rotor diameter	126 m
Hub-height	87.6 m
Generator rated speed	1,173.7 RPM
Generator rated torque	43,093.55 Nm
Pitch upper and lower limits	0° and 90°
Pitch rate limit	8°/s

Table 2.2: Key Specifications of GRC WT

Parameters	Values
Configuration, rating	3 blades, 750 kW
Gearbox, overall ratio	3 Stages, 81.49
Rotor, hub diameter	48.2 m, 1.2 m
Hub-height	54.8 m
Rated rotor speed	22.1 RPM
Maximum rotor C_P	0.43

where where $\mathbf{A}, \mathbf{B}, \mathbf{B}_d, \mathbf{C}, \mathbf{D}, \mathbf{D}_d$ are averaged state-space model matrices. Each matrix is averaged over N azimuth angles θ_l , e.g.

$$\mathbf{A} = \frac{1}{N} \sum_{l=1}^N \mathbf{A}_F(\theta_l) \quad (2.6)$$

2.3 Turbine Types

Two WTs are modeled in this thesis, each of which is dedicated for a part of the thesis. The `.fst` file attributed to each WT was loaded to FAST to simulate the responses. For the pitch controller designs, the NREL 5-MW reference WT [17] is considered, properties of which are listed in Table 2.1. For the generator torque controller designs and overall drivetrain study, the WT model is based on the 750-kW Gearbox Research Collaborative (GRC) WT [18] operating at the Ponnequin wind farm in northern part of Colorado, U.S.. Table 2.2 summarizes the important properties of this WT.

2.4 Generator Types

WTs can be classified to four basic types according to their generation technologies [19]:

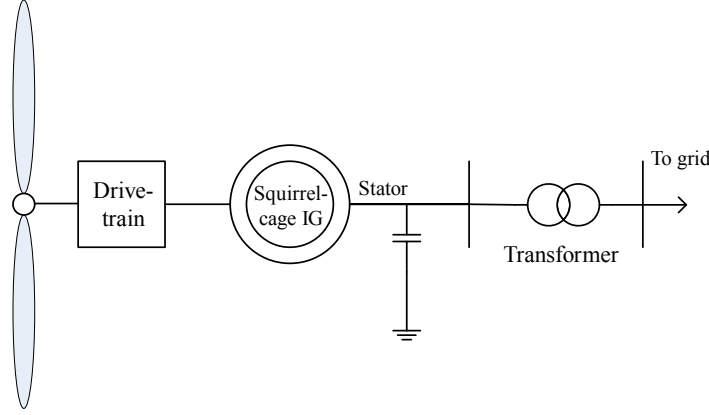


Figure 2.6: Schematic of type 1 WTs.

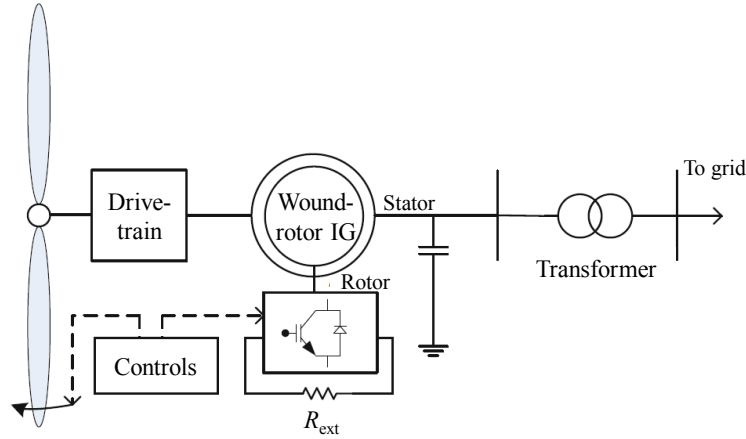


Figure 2.7: Schematic of type 2 WTs.

- Type 1: fixed-speed WTs

Fixed-speed WTs are the most basic utility-scale WTs in operation. The schematic of type 1 WTs is shown in Fig. 2.6, which is also known as the Danish concept. Type 1 WTs operate with very little variation in WT rotor speed and employ a squirrel-cage induction generator (IG) directly connected to the grid. Because of the limited speed range in which these WTs operate, they are prone to large torque spikes that may damage the drivetrain components and cause transients in the electrical circuitry. The aerodynamic energy capture of these WTs is also suboptimal because of their limited speed variation. These factors contribute to the fact that this WT type are no longer manufactured.

- Type 2: variable-slip WTs

Variable-slip WTs employ wound-rotor IGs that allow access to both the stator and rotor

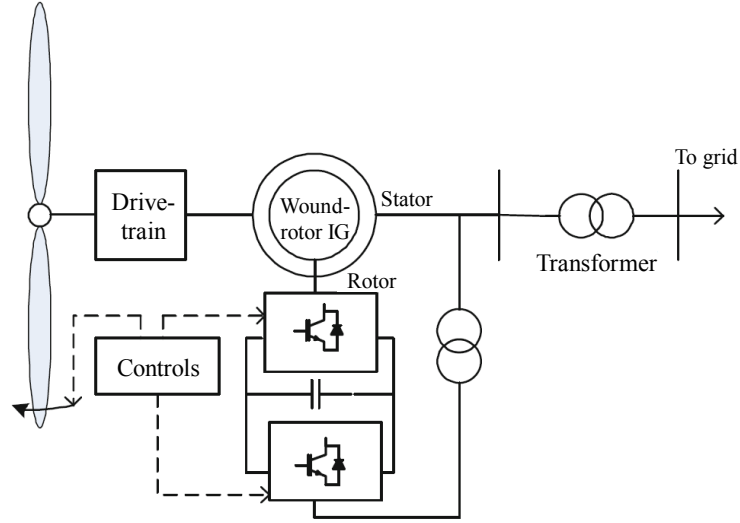


Figure 2.8: Schematic of type 3 WTs.

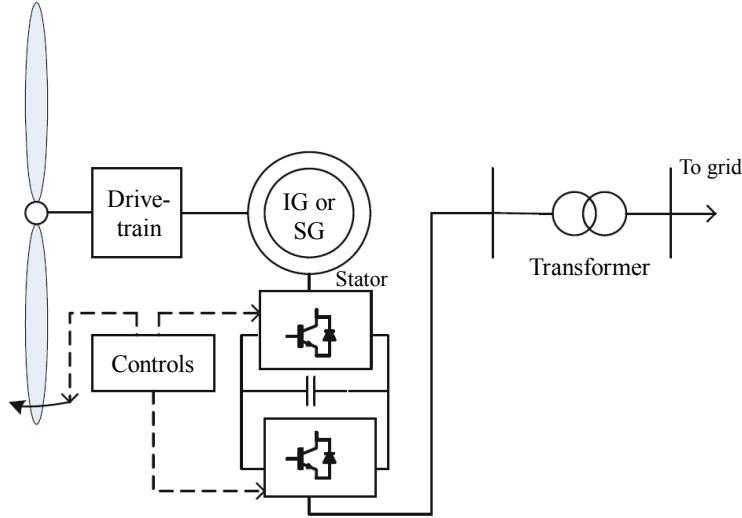


Figure 2.9: Schematic of type 4 WTs.

of the generator. The schematic of type 2 WTs is shown in Fig. 2.7, which is known as the Vestas OptiSlip concept. The rotor circuit is connected to an alternating current-direct current (AC-DC) converter and a fixed resistance. The converter is switched to control the effective resistance in the rotor circuit to widen the range of the operating slip variation, and hence speed variation, up to 10%. A controller is employed to vary the effective external rotor resistance for optimal power extraction. However, some power is lost as heat in the external rotor circuit resistance.

- Type 3: doubly-fed induction generator (DFIG) WTs

DFIG-based WTs remedy the problem of power loss in the rotor circuit of type 2 WTs by replacing the resistor with back-to-back AC/DC/AC converters in the rotor circuit. The schematic of type 3 WTs is shown in Fig. 2.8. Because the converters handle only the power in the rotor circuit, they do not need to be rated at the generator's full output power. The disadvantages of this technology, namely the higher cost and complexity, are offset by the ability to optimally extract the aerodynamic energy in a wind regime than the preceding technologies. This WT type has been the most widely installed one for onshore WTs. Its application is still expected to increase even into megawatt (MW)-rating WTs amidst the growing interest in the next WT type.

- Type 4: full-converter WTs

In full-converter WTs, the power conversion only flows from the WT rotor through the back-to-back AC/DC/AC converters to the grid. Thus, there is no direct connection to the grid and the converters have to be rated to handle the entire output power. The schematic of type 4 WTs is shown in Fig. 2.9. These WTs usually employ high pole-count permanent magnet synchronous generators (SGs) to allow low-speed operation, hence allowing the elimination of the gearbox; although using IGs is also possible. The interests in this technology are increasing, especially for MW-rating offshore WTs, although the expected increased reliability promised by this technology has not been well proven.

This thesis takes its focus on type 3 WTs as they are currently the most prominently implemented WTs in the market. DFIG models with different level of fidelity are available in the SimPowerSystems library of MATLAB/Simulink. As illustrated in Chapters 5 and 7, each model was accordingly selected and modified to fit the purpose of each investigation. The generator model is integrated with FAST to investigate the electromechanical interactions present in WT operations. Integration of FAST with other generator models are discussed in [20].

2.5 Control Objectives

The popular variable speed and variable pitch capabilities of type 3 utility scale WTs further promote the development of novel controllers. Type 3 WT operates in five major operating regions based on the output power of the generator as a function of the effective wind velocity, as shown

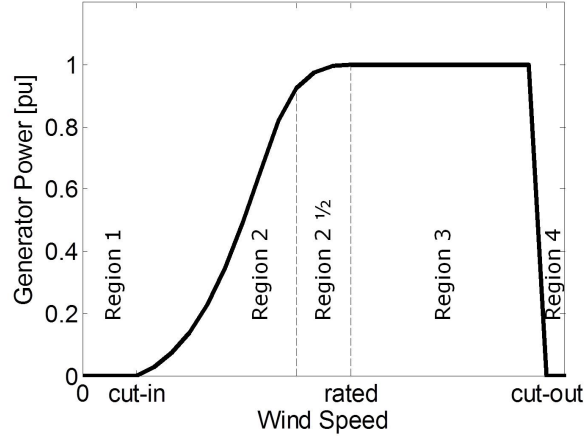


Figure 2.10: Typical power curve of type 3 WT,
1 pu (per unit) power = rated power of the generator.

in Fig. 2.10. The distinct output power requirement determines the main control objective of each region [21–25].

Region 1 lies below the cut-in wind velocity. In this region, the mean power available in the wind is insufficient to overcome electrical and mechanical losses. Region 2 lies between the cut-in and rated wind velocities. In this region, the WT operates to capture as much wind energy as possible by controlling the generator torque to reach the optimum WT rotor speed. The power captured by the WT rotor is given by

$$P_{\text{rot}} = \frac{1}{2} C_P(\lambda, \beta) \rho A V_l^3 \quad (2.7)$$

where ρ is the air density, V_l is the longitudinal wind velocity perpendicular to the WT rotor plane, A_{rot} is the rotor swept area, and C_P is the rotor power coefficient, which is a function of the tip speed ratio (TSR) λ and blade pitch angle β . The TSR is given by

$$\lambda = \frac{\omega_{\text{rot}} R}{V_l} \quad (2.8)$$

where ω_{rot} is the WT rotor rotational speed and R is the rotor radius.

To ensure maximum extraction of the wind power, it is imperative to ensure that the WT is operating at the maximum power coefficient $C_{P,\text{max}}$. Figure 2.11 shows the power coefficient curve of a type 3 WT. The maximum power extraction can be achieved by fixing the blade pitch angle at

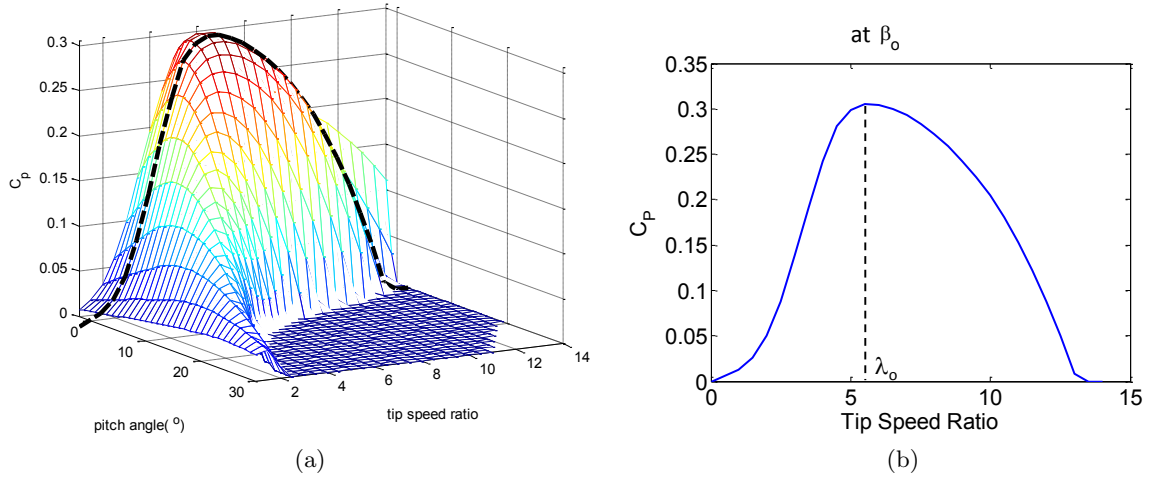


Figure 2.11: Power coefficient of a type 3 WT.

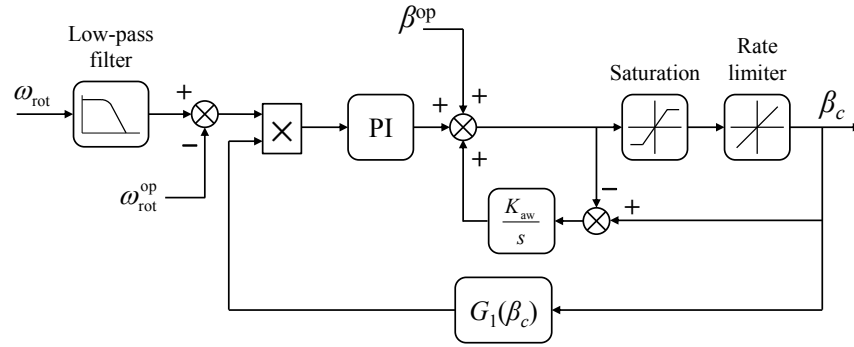


Figure 2.12: Schematic of the baseline CPC.

its optimum value β_o , as represented by the black dotted line in Fig. 2.11(a), and then regulating the rotor speed such that the TSR is optimum at λ_o , as shown in Fig. 2.11(b). The generator torque Q_{gen} of DFIG in region 2 is controlled as [26, 27]

$$Q_{gen} = k_{opt} \omega_{rot}^2 \quad (2.9)$$

$$k_{opt} = \frac{1}{2} \rho A R^3 \frac{C_{P,max}}{\lambda_o^3}$$

The quadratic torque control law given by Eq. (2.9) in steady-state causes the WT to operate at the optimum TSR λ_o . The dynamics of the WT considering a simple rigid body model relating

the net torque and WT angular acceleration is defined as

$$\begin{aligned}\dot{\omega}_{\text{rot}} &= \frac{1}{J} (Q_{\text{aero}} - Q_{\text{gen}}) \\ &= \frac{1}{2J} \rho A R^3 \omega_{\text{rot}}^2 \left(\frac{C_P}{\lambda^3} - \frac{C_{P,\text{max}}}{\lambda_o^3} \right)\end{aligned}\tag{2.10}$$

Because the WT overall inertia J , ρ , A , R , ω_{rot}^2 are not negative, the sign of $\dot{\omega}_{\text{rot}}$ depends on the sign of the difference within the parentheses. Because by definition $C_P \leq C_{P,\text{max}}$, if $\lambda > \lambda_o$ then $\dot{\omega}_{\text{rot}} < 0$, meaning that assuming constant wind, the WT will decelerate toward $\lambda = \lambda_o$ and vice versa.

Region 2 $\frac{1}{2}$ starts close to the rated wind velocity and helps to smooth the transition between regions 2 and 3. Region 3 lies between the rated and cut-out wind velocities. In this region, the WT operates to produce constant output power at its rated value in spite of varying wind velocity. The constant rated power can be achieved by operating the WT at constant generator torque and, thus, regulating constant generator speed through a feedback control, wherein the pitchable blades act as the control actuation. The predominant methods of regulating constant generator speed are based on the control methods utilizing collective blade pitch actuation (i.e., equal pitch angle for all blades). The collective pitch controller (CPC) commonly implemented in wind energy industry is based on a single-input-single-output (SISO) gain-scheduled PI (GSPI) controller as depicted in Fig. 2.12 [23, 28]. Its main objective is to maintain the rotor speed ω_{rot} at its rated value $\omega_{\text{rot}}^{\text{op}}$ in the presence of the continuously changing wind velocity. The rotor speed measurement is low-pass filtered to attenuate the effects of measurement noise and unmodeled dynamics [29–31]. The PI gains are scheduled through a function G_1 of the collective blade pitch angle β_c to account for the nonlinear WT aerodynamics [17]. A back-calculation scheme with an anti windup gain K_{aw} is implemented to prevent integral windup due to saturation of the pitch actuator. Finally, region 4, lies above the cut-out wind velocity. In this region, the WT is parked to prevent damages to the WT components due to enormous loads coming from extremely high wind velocity.

This thesis proposes control strategies to achieve the primary objectives of region 2 (below rated wind velocity) and 3 (above rated wind velocity) operations. Further, the proposed controller designs aim to mitigate fatigue loads of the WT components. The discussions commence with the designs of pitch controllers, in which the generator torque is kept constant, to mitigate the

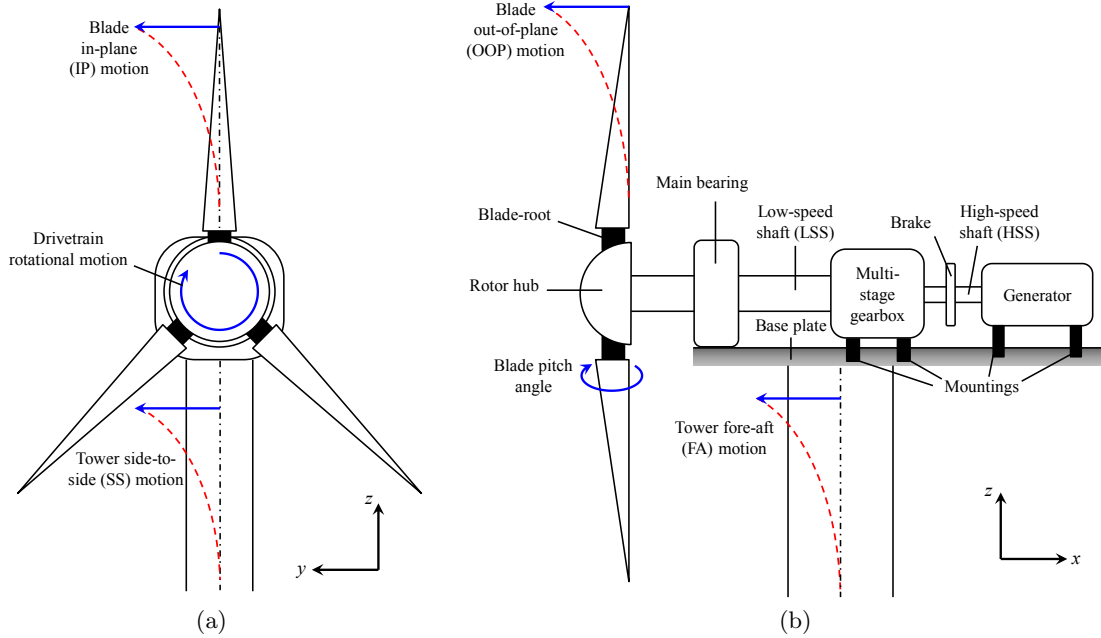


Figure 2.13: Motions of WT components from (a) front and (b) side views.

drivetrain and blade loads; followed by the designs of generator torque controllers, in which the blade pitch angles are kept constant, to mitigate the drivetrain loads.

2.6 Damage Equivalent Load

The critical WT loads considered in this thesis are in the directions of motions shown in Fig. 2.13. The front view shows the WT loads in the rotor plane while the side view shows the ones perpendicular to it. The blade in-plane (IP) motion results in bending moment at the blade-root (i.e., the connection between the blade and the hub) in the same direction. Similarly, the blade out-of-plane (OOP) motion results in blade-root OOP bending moment. The tower side-to-side (SS) and fore-aft (FA) motions result in SS and FA bending moment loads, respectively. They can be measured on the top of the tower (i.e., loads on the nacelle base plate) or at the base of the tower (i.e., loads on the WT foundation). Finally, the drivetrain rotational motion results in torque (i.e., torsional loads) transmitted through the shafts and gears.

To quantify the structural loads of the WT components in terms of fatigue loads, the 1 Hz DEL was calculated for each case. The concept of DEL has been widely used in WT application [32–34].

The DEL S_{eq} is defined as

$$S_{\text{eq}} = \left(\frac{1}{N_{\text{eq}}} \sum_i (n_i L_i^m) \right)^{\frac{1}{m}} \quad (2.11)$$

which represents a constant load amplitude S_{eq} that, for a chosen equivalent number of cycles N_{eq} , produces the same damage as an oscillatory load with n_i cycles each of which has a range of L_i . n_i and L_i are calculated using a rainflow counting algorithm [35] based on the Palmgren-Miner rule for linear accumulation of damage with m as the slope of the material cyclic stress to failure (i.e., the SN curve). In the rainflow counting algorithm, both mean and range of the load are taken into consideration. Thus, the WT control objective to reduce the DEL (i.e., to mitigate the fatigue load) is not limited only to reducing the load fluctuation.

In this thesis, the DELs were computed using the MLife code [36] based on the simulated time-series loads with $N_{\text{eq}} = t$, where t is the data length in second. The slopes of the SN curves are shown in Table 2.3 according to the materials commonly used to manufacture each WT component.

Table 2.3: Slopes of the SN curves

Components	Values
Tower	3
Drivetrain (i.e., shafts and gears)	8
Blades	10

Chapter 3

Pitch Controller to Mitigate Load due to Unmodeled Dynamics

3.1 Introduction

The formulation of disturbance accommodating controller (DAC) to maintain the WT output power at its rated during region 3 operation has been emerging during the last decade as an alternative to the typical PI controller shown in 2.12. DAC was firstly introduced by Johnson [37,38] and as its name suggests, DAC considers the dynamics of the process disturbance. For WT applications, DAC regards the oncoming wind as a persistent disturbance input and has been demonstrated through numerical simulations and field tests to successfully attenuate the effects of changing wind velocity [5, 29, 39–43]. However, as reported in [5], this approach is sensitive to modeling errors. Simulations using DAC that is designed based on a lower-order WT model assuming only the torsional flexibility of the drivetrain but implemented on a WT with higher-order dynamics (i.e., having flexibilities at other components, such as blades and towers) can lead to an unstable system response. Moreover, when measurement noise is present, additional low-pass filter is required to prevent noisy actuation signal. Otherwise, problems such as chattering and saturation of the actuator may arise.

This chapter presents a new control strategy based on the concept of stochastic disturbance accommodating control [44] for variable pitch (but not necessarily variable speed) WTs to compensate for the unmodeled dynamics, (i.e., the neglected modes during the design of the controller), changing wind velocity, and measurement noise. The term ‘stochastic’ stems from the assumption of a stochastic plant model having uncertainties due to the unmodeled dynamics and/or modeling errors. These inherent uncertainties can cause instability if only the nominal control feedback law is applied. To achieve stability, this approach proposes the use of tuned Kalman estimation in the

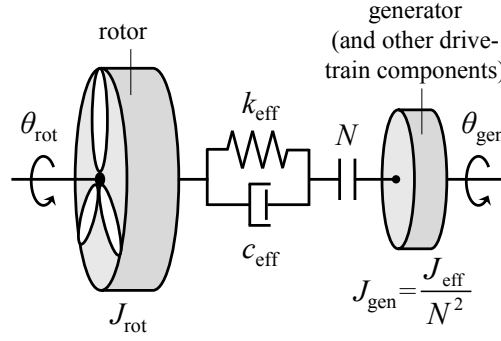


Figure 3.1: Two-mass model of WT drivetrain

feedback loop to estimate both plant and disturbance states from a noisy measurement signal. This work is motivated by some practical advantages of implementing the Kalman estimator including easy tuning of the estimator parameters (i.e., the noise covariance matrices) and a more economic implementation because Kalman estimator can be used directly to filter noisy measurements.

3.2 Turbine and Actuator Models

This chapter considers the NREL 5-MW reference WT, properties of which are listed in Table 2.1. For the design of the stochastic disturbance accommodating controller (SDAC), the WT was modelled considering only the flexibility of the drivetrain. This model is well-known as the two-mass model shown in Fig. 3.1. The other structural parts (i.e., the blades and towers) were assumed rigid. The WT model was linearized around the wind velocity of 16 m/s, which is referred throughout this chapter as the linearization wind velocity. State-space formulation for this assumed WT model can be expressed as

$$\Delta \dot{\mathbf{x}}_F = \mathbf{A}_F \Delta \mathbf{x}_F + \mathbf{B}_F \Delta u_F + \mathbf{B}_{d,F} \Delta u_{d,F} \quad (3.1)$$

where

$$\Delta \mathbf{x}_F = \left\{ \Delta \omega_{\text{rot}} \quad \Delta \theta_{\text{rot}} - \Delta \theta_{\text{gen}} \quad \Delta \omega_{\text{gen}} \right\}^T, \quad \Delta u_F = \Delta \beta_c, \quad \Delta u_{d,F} = \Delta V_l$$

The three states considered in vector $\Delta \mathbf{x}_F$ are the perturbed rotor angular velocity, torsional deflection of the drivetrain, and generator angular velocity, respectively. The control input Δu_F is the perturbed actual pitch angle $\Delta \beta_c$ and the disturbance input $\Delta u_{d,F}$ is the perturbed wind velocity ΔV_l . This model is referred as the three-state model in, such as [5].

Pitch actuators for WT's can be either hydraulic or electric motors. They are necessary to alter the pitch angle of each blade. However, FAST does not provide any models to represent the dynamics of pitch actuators. Therefore, a 2nd order actuator model is commonly used for piston servo system commonly installed in megawatt scale WT's [45–48]

$$\beta_c = \frac{\omega_n^2}{s^2 + 2\zeta\omega_n s + \omega_n^2} \beta_r \quad (3.2)$$

where β_r is the commanded reference pitch angle, which acts as the input to the actuator. As there is no actual implemented actuator for the NREL 5-MW reference WT, parameters of the actuator model were chosen to have similar cut-off frequency (the -3 dB frequency) to that of an operating WT in [24, 49] with $\omega_n = 30$ rad/s and $\zeta = 0.7$.

It is important to mention that in this chapter, the actuator model is implemented only for the evaluation of control performance. Due to a reason elaborated in the following section, the actuator model is not considered during the design of the controller. In other words, during the design stage, it is assumed that $\beta_c = \beta_r$.

3.3 Collective Pitch Controllers

In order to facilitate a fair comparison, wherein the same number of sensors is used for both controllers, the control schemes in this chapter take the generator speed measurement as its only input and give the collective pitch command as its output.

3.3.1 Baseline GSPI Controller

The GSPI controller shown in Fig. 2.12 is the baseline controller in simulating the response of the NREL 5-MW reference WT [30]. In designing this controller, the WT was modelled as one rigid inertia. Therefore, neither the WT structural flexibilities nor the actuator dynamics was considered. In the cases of realistic turbulent wind fields while the region 3 pitch controller is being implemented, the instantaneous wind velocity occasionally dips from region 3 to region 2 and it may stay there for some time before returning back to region 3. This scenario can cause the integral windup issues, and thus, an integral anti windup is implemented to tackle such problem. The overall schematic of this baseline control strategy is shown in Fig. 3.2.

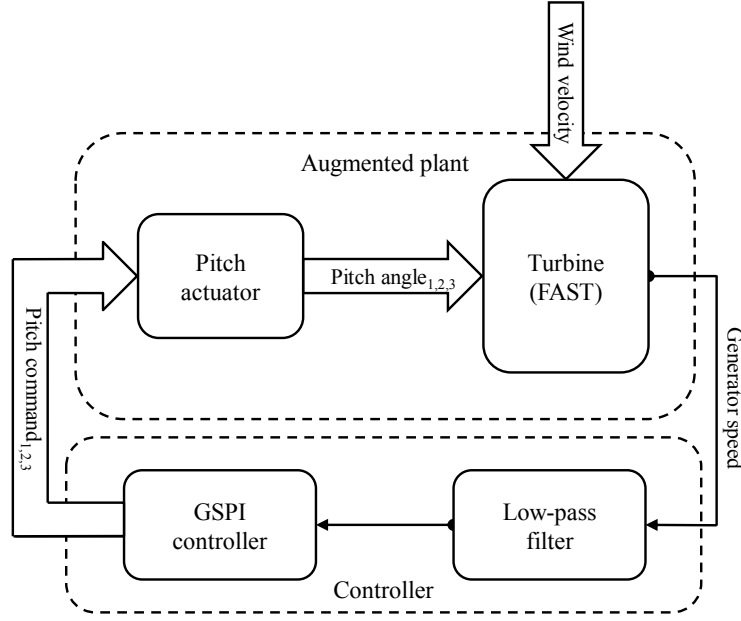


Figure 3.2: Schematic for simulation using GSPI controller.

3.3.2 SDAC

The SDAC is designed based on the linearized plant model shown in Eq. (3.1). Because $(\mathbf{A}_F, \mathbf{B}_F)$ is controllable, a feedback control law with static gain can be designed as the nominal control law in order to place the poles of the closed-loop system at the desired locations

$$\Delta \bar{u}_F = -\mathbf{G}_F \Delta \mathbf{x}_F \quad (3.3)$$

In the design of DAC for WT application, the wind variations can be modelled as persistent disturbances [37] while the effects of the unmodeled dynamics can be assumed to introduce Gaussian white process noise into the system. This results in disturbance dynamics that is modeled as

$$\Delta \dot{x}_{d,F} = A_d \Delta x_{d,F} + \mathcal{W} \quad (3.4)$$

$$\Delta u_{d,F} = C_d \Delta x_{d,F} \quad (3.5)$$

where \mathcal{W} is the zero mean Gaussian white process noise due to the unmodeled dynamics. In previous applications of DAC for WT system [5, 29, 39–43], there has been no consideration on the

unmodeled dynamics (i.e., no \mathcal{W} in Eq. (3.4)). Instead, the previous designs on DAC required a high-order dynamic model of the WT because only drivetrain model of Eq. (3.1) is not sufficient. Otherwise, the closed-loop system will be unstable, as shown later in Section 3.4.

In this work, the change in wind velocity is assumed to be a step persistent disturbance, which has been shown to be an adequate approximation of uniform wind velocity for WT controllers [5, 29, 39] with $A_d = 0$ (i.e., zero eigenvalue for persistent disturbance) and $C_d = 1$. To attenuate the effect of the disturbance input $\Delta u_{d,F}$ on the system dynamics, one can theoretically set an additional feedback control law based on Eqs. (3.1, 3.4, 3.5) as

$$\Delta u_F^* = -G_{d,F} \Delta x_{d,F} \quad (3.6)$$

where, for $C_d = 1$

$$G_{d,F} = (\mathbf{B}_F^T \mathbf{B}_F)^{-1} \mathbf{B}_F^T \mathbf{B}_{d,F}$$

Thus, the total DAC feedback law is stated as

$$\Delta u_F = \Delta \beta_c = \Delta \bar{u}_F + \Delta u_F^* = - \begin{bmatrix} \mathbf{G}_F & G_{d,F} \end{bmatrix} \begin{Bmatrix} \Delta \mathbf{x}_F \\ \Delta x_{d,F} \end{Bmatrix} \quad (3.7)$$

It is important to note that the actuator model is not considered during the controller design stage because it introduces a problem in the disturbance attenuation. It results in a steady-state error in the speed regulation if the controller gains are not carefully tuned, which could be explained as follows. If the actuator model was considered in controller design, an augmented (WT with actuator) plant model would be created, resulting in the following linearized state-space representation

$$\begin{aligned} \Delta \dot{\mathbf{x}}_p &= \mathbf{A}_p \Delta \mathbf{x}_p + \mathbf{B}_p \Delta \beta_r + \mathbf{B}_{d,p} \Delta u_{d,F} \\ \begin{Bmatrix} \Delta \dot{\mathbf{x}}_F \\ \Delta \dot{\mathbf{x}}_a \end{Bmatrix} &= \begin{bmatrix} \mathbf{A}_F & \mathbf{B}_F \\ 0 & \mathbf{A}_a \end{bmatrix} \begin{Bmatrix} \Delta \mathbf{x}_F \\ \Delta \mathbf{x}_a \end{Bmatrix} + \begin{bmatrix} 0 \\ \mathbf{B}_a \end{bmatrix} \Delta \beta_r + \begin{bmatrix} \mathbf{B}_{d,F} \\ 0 \end{bmatrix} \Delta u_{d,F} \end{aligned} \quad (3.8)$$

where

$$\begin{aligned} \Delta \dot{\mathbf{x}}_a &= \mathbf{A}_a \Delta \mathbf{x}_a + \mathbf{B}_a \Delta \beta_r \\ \begin{Bmatrix} \Delta \dot{\beta}_c \\ \Delta \ddot{\beta}_c \end{Bmatrix} &= \begin{bmatrix} 0 & 1 \\ -\omega_n^2 & -2\zeta\omega_n \end{bmatrix} \begin{Bmatrix} \Delta \beta_c \\ \Delta \dot{\beta}_c \end{Bmatrix} + \begin{bmatrix} 0 \\ \omega_n^2 \end{bmatrix} \Delta \beta_r \end{aligned}$$

represents the actuator model of Eq. (3.2) in the state-space representation.

Following the previously developed approach for the WT model only, one can set the total control law for the augmented plant to be

$$\Delta \beta_r = - \begin{bmatrix} \mathbf{G}_p & G_{d,p} \end{bmatrix} \begin{Bmatrix} \Delta \mathbf{x}_p \\ \Delta x_{d,F} \end{Bmatrix} \quad (3.9)$$

so that in the steady-state (i.e., $\dot{\mathbf{x}}_p = 0$) the augmented states can be expressed as

$$\Delta \mathbf{x}_{p,ss} = (\mathbf{A}_p - \mathbf{B}_p \mathbf{G}_p)^{-1} (\mathbf{B}_p G_{d,p} - \mathbf{B}_{d,p}) \Delta x_{d,F} \quad (3.10)$$

Disturbance attenuation for the augmented plant can be achieved by setting the disturbance state gain as $G_{d,p} = (\mathbf{B}_p^T \mathbf{B}_p)^{-1} \mathbf{B}_p^T \mathbf{B}_{d,p}$. However, due to the structures of both the control and disturbance input matrices (i.e., \mathbf{B}_p and $\mathbf{B}_{d,p}$, respectively) the resulting gain $G_{d,p}$ would always be zero. In other words, there would be no actuation that acts to attenuate the effect of the changing wind velocity. Moreover, it implies that for any tuned values of $G_{d,p} \neq 0$, the term $(\mathbf{B}_p G_{d,p} - \mathbf{B}_{d,p}) \neq 0$.

Physically, one can see that the augmented system in Eq. (3.8) does not relate the augmented system states $\Delta \mathbf{x}_p$ to the aerodynamic effect of the commanded pitch angle $\Delta \beta_r$, which in the WT model of Eq. (3.1) is served by \mathbf{B}_F that relates $\Delta \mathbf{x}_F$ to $\Delta \beta_c$. As a result, the disturbance state gain computed based on the augmented system model does not give a good disturbance rejection response.

It is important to note that in steady-state, the actuator state $\Delta \mathbf{x}_a$ must not be zero as it contains the perturbed actual pitch angle $\Delta \beta_c$. However, it is possible to find the tuned $G_{d,p}$ so that, from Eq. (3.10), the WT states $\Delta \mathbf{x}_F$ have the desired zero steady-state values. In order to do

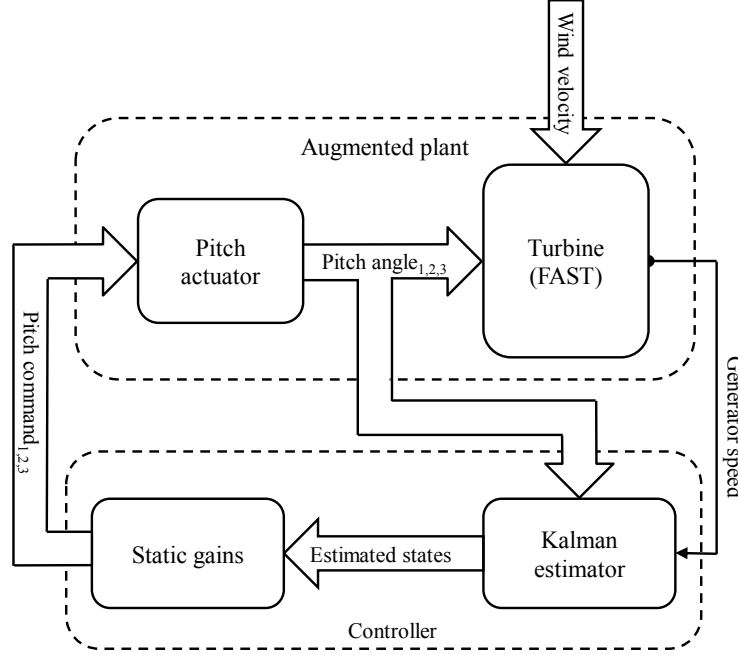


Figure 3.3: Schematic for simulation using SDAC.

so, the tuned value $G_{d,p}$ is now dependant on the value of \mathbf{G}_p . In other words, the feedback gain for the disturbance state is different for different desired closed-loop pole locations. This in turn complicates the tuning process. On the contrary, the DAC feedback law designed by omitting the actuator dynamics does not suffer from any steady-state error. This stems from the fact that for common pitch actuators at the steady-state $\beta_c = \beta_r$, conforming with the basic assumption used in designing the control feedback law in Eq. (3.7). Therefore, it is recommendable to omit the dynamics of pitch actuator in designing the DAC feedback law.

As only the generator speed is available from measurement, it is necessary to design a state estimator to obtain the estimates of the other WT states as well as the disturbance state. The linearized plant model, Eq (3.1), can be augmented with the disturbance model, Eq. (3.4), and the generator speed measurement as

$$\Delta \dot{\mathbf{x}}_o = \mathbf{A}_o \Delta \mathbf{x}_o + \mathbf{B}_o \Delta u_F + \mathbf{D}_o \mathcal{W} \quad (3.11)$$

$$\begin{aligned} \begin{Bmatrix} \Delta \dot{\mathbf{x}}_F \\ \Delta \dot{x}_{d,F} \end{Bmatrix} &= \begin{bmatrix} \mathbf{A}_F & \mathbf{B}_{d,F} \\ 0 & 0 \end{bmatrix} \begin{Bmatrix} \Delta \mathbf{x}_F \\ \Delta x_{d,F} \end{Bmatrix} + \begin{bmatrix} \mathbf{B}_F \\ 0 \end{bmatrix} \Delta u_F + \begin{bmatrix} 0 \\ \mathbf{I} \end{bmatrix} \mathcal{W} \\ \Delta y_F &= \mathbf{C}_o \Delta \mathbf{x}_o + \mathcal{V} = \begin{bmatrix} \mathbf{C}_F & 0 \end{bmatrix} \Delta \mathbf{x}_o + \mathcal{V} \end{aligned} \quad (3.12)$$

where \mathcal{V} is zero mean Gaussian white measurement noise.

$(\mathbf{A}_o, \mathbf{C}_o)$ is found to be observable. Thus, even though the disturbance state is not measured, based on the assumed stochastic properties of \mathcal{W} and \mathcal{V} , an optimal estimator such as Kalman estimator can be implemented to estimate the unmeasured system and disturbance states from the noisy measurement. The estimator dynamics can be written as

$$\Delta \dot{\hat{\mathbf{x}}}_o = \mathbf{A}_o \Delta \hat{\mathbf{x}}_o + \mathbf{B}_o \Delta u_F + \mathbf{K}(\Delta \mathbf{x}_o - \Delta \hat{\mathbf{x}}_o) + \mathbf{K}\mathcal{V} \quad (3.13)$$

where the Kalman gain can be calculated as $\mathbf{K} = \mathbf{P}\mathbf{C}_o^T R^{-1}$ and the estimation error covariance matrix $\mathbf{P} = E[(\Delta \mathbf{x}_o - \Delta \hat{\mathbf{x}}_o)(\Delta \mathbf{x}_o - \Delta \hat{\mathbf{x}}_o)^T]$ can be obtained by solving the continuous-time Riccati equation

$$\dot{\mathbf{P}} = \mathbf{A}_o \mathbf{P} + \mathbf{P} \mathbf{A}_o^T - \mathbf{K} \mathbf{C}_o \mathbf{P} + \mathbf{D}_o \mathbf{Q} \mathbf{D}_o^T \quad (3.14)$$

where \mathbf{Q} and R are the process noise covariance matrix and measurement noise covariance, respectively. Because R can be obtained during the calibration of the measurement sensor, \mathbf{Q} acts as the tuning parameter for the Kalman estimator. The overall schematic of the proposed SDAC is shown in Fig. 3.3.

3.4 Simulation Results and Discussions

3.4.1 Simulation with Step Wind Inputs

As a tuning guideline of the proposed SDAC, it is important to note that if $\mathbf{Q} = \mathbf{0}$, then the estimated disturbance state $\Delta \hat{x}_{d,F} = 0$. Thus, the total control law in Eq. (3.7) becomes just the nominal control. For the case presented in this study, the nominal control $\Delta \bar{u}_F$ of the designed DAC acting on the ‘true’ plant with higher-order dynamics results in an unstable system. Therefore, selecting too small \mathbf{Q} will also result in an unstable system. Figure 3.4 shows the generator speed (i.e., the output) and commanded pitch angle (i.e., the input) responses from simulation with FAST for the NREL 5-MW reference WT with $\mathbf{Q} = \mathbf{0}$. The wind input for this simulation was a constant uniform wind velocity of 16 m/s (i.e., the linearization wind velocity). As discussed in the previous section, the SDAC was designed by considering only the dynamics of the WT drivetrain, while the ‘true’ plant (i.e., the WT modeled in FAST) included other structural dynamics of blades and

tower. Despite designing the nominal control law of Eq. (3.3) that has stable closed-loop poles, the responses show unexpected deterioration of performance due to the unmodeled dynamics. Similar deterioration in the response was also reported in [5]. Figure 3.4(a) shows that the deteriorated performance is indeed due to the unmodeled high-order dynamic, which in turn forces the saturation of the actuator, as illustrated in Fig. 3.4(b).

On the other hand, selecting a large \mathbf{Q} value would compel the Kalman estimator to completely rely upon the measurement signal and therefore the noise associated with the measurement signal is directly transmitted into the estimates and then the control input [44]. In simulating the WT responses, a Gaussian white noise with a variance of 10 RPM², giving a signal to noise ratio of approximately 50 dB, was present in the measured generator speed signal. Figure 3.5 shows the simulated responses of the NREL 5-MW reference WT with a large diagonal matrix \mathbf{Q} , as well as a tuned one. The rough tuning of the diagonal matrix \mathbf{Q} was done to achieve more or less similar generator speed response with that of the baseline GSPI controller at the linearization wind velocity, as illustrated in Fig. 3.6 for the NREL 5-MW reference WT. It is further fine tuned to have a similar root mean square (RMS) generator speed error at the chosen linearization mean turbulent wind velocity, as discussed in the following subsection.

A good estimate of the wind velocity is critical in DAC as it directly affects the disturbance attenuation performance. For SDAC with the tuned \mathbf{Q} , Fig. 3.7 shows the wind estimate under multistep wind velocity input. Being a linear controller, it is expected that the estimation deteriorates as the wind velocity deviates away from the linearization wind velocity of 16 m/s due to the nonlinear aerodynamicss. Nevertheless, as shown in the following subsection, the control performance still yields good speed regulation.

3.4.2 Simulation with Turbulent Wind Inputs

To evaluate and compare the performance of the proposed SDAC to that of the baseline GSPI controller, simulations were performed under turbulent wind conditions for simulation time of 600 seconds each, following the IEC 6400-12 standard [50]. As this chapter focuses solely on the control objectives of region 3 operation, no switching of control logic is implemented although the instantaneous wind velocity occasionally drops to region 2 or rises to region 4 for a while.

TurbSim was used to generate realistic hub-referenced turbulent wind fields following the Kaimal

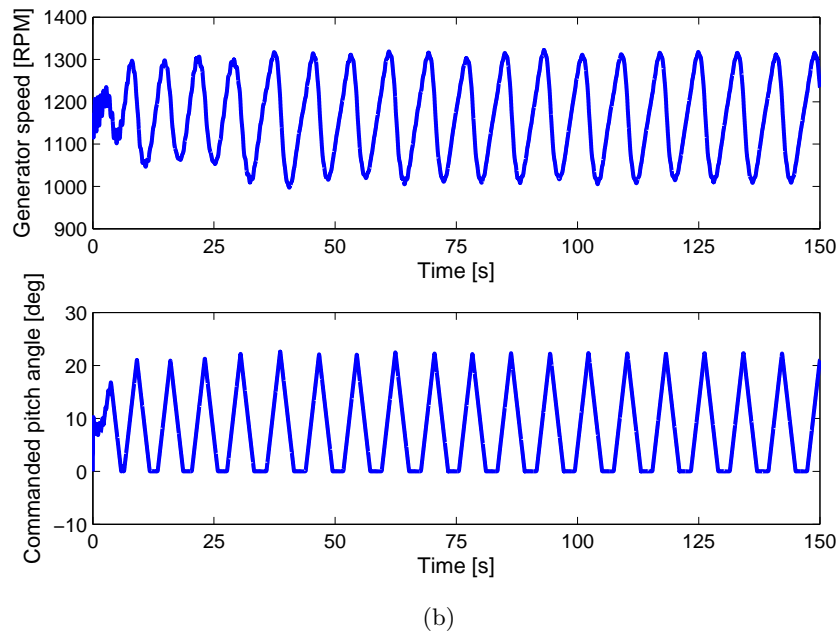
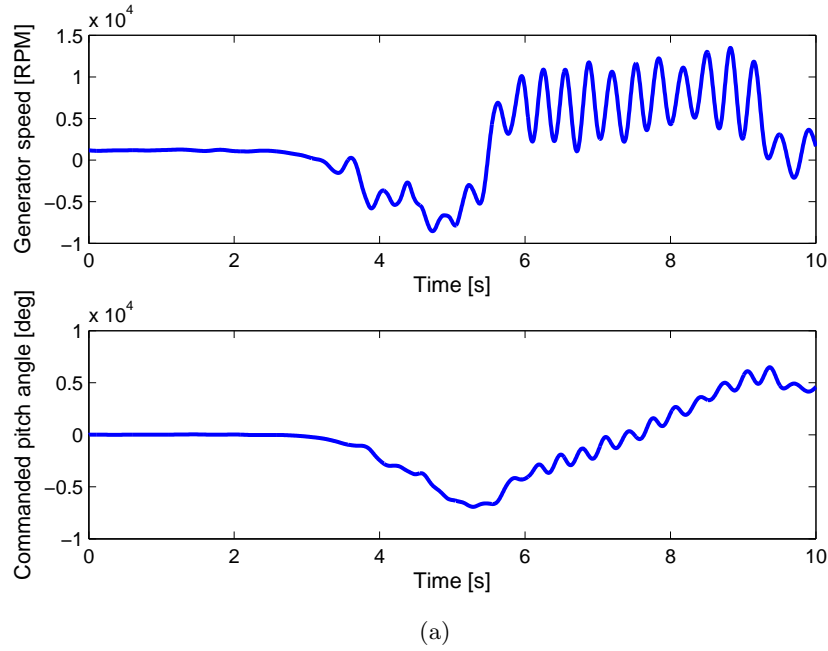


Figure 3.4: Deterioration in system responses for $\mathbf{Q} = \mathbf{0}$
 (a) with ideal (limitless) pitch actuator and (b) with actual pitch actuator.

spectrum [14]. Five turbulence cases were simulated. Each case used nine different turbulence seeds, resulting in a total number of 45 simulations. Four of the tested cases have different mean wind velocities with low turbulence intensity of class C while the remaining has high turbulence intensity of class A at the linearization mean wind velocity. Each operating condition is presented

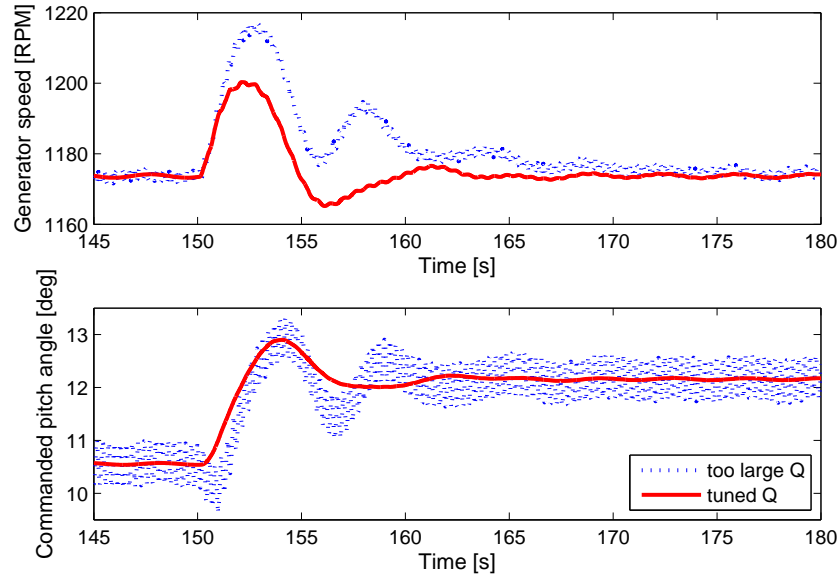


Figure 3.5: Noisy input and output responses due to large Q .

by indicating the mean velocity followed by the turbulence class or intensity in parentheses. For example, 16 m/s (C) represents the condition with mean wind velocity of 16 m/s with turbulence class C. Simulations on cases beyond these mean wind velocities and turbulence intensities resulted in an invalid comparison as the integral windup yielded severe performance deterioration for the baseline GSPI controller despite implementation of the integral anti windup.

Relative performance between the controllers is compared in terms of speed regulation, DEL of the low-speed shaft (LSS), and control cost. The speed regulation is compared using the RMS and maximum value of the speed error from the rated generator speed. The control cost is compared using the RMS of the blade pitch rate. Notched boxplot for each performance metric is plotted side by side for graphical comparison. The notch feature serves to highlight the difference among the data groups. Nonoverlapping notches offer evidence of a statistically significant difference between two compared boxplots with 95% confidence level. Further, in order to standardize the comparison, both controllers are tuned to achieve approximately similar RMS generator speed error at the reference operating condition. This reference operating condition corresponds to the one at the linearization mean wind velocity with lower turbulence intensity of class C. All performance metrics are normalized with respect to the median of the corresponding metric of the reference operating condition.

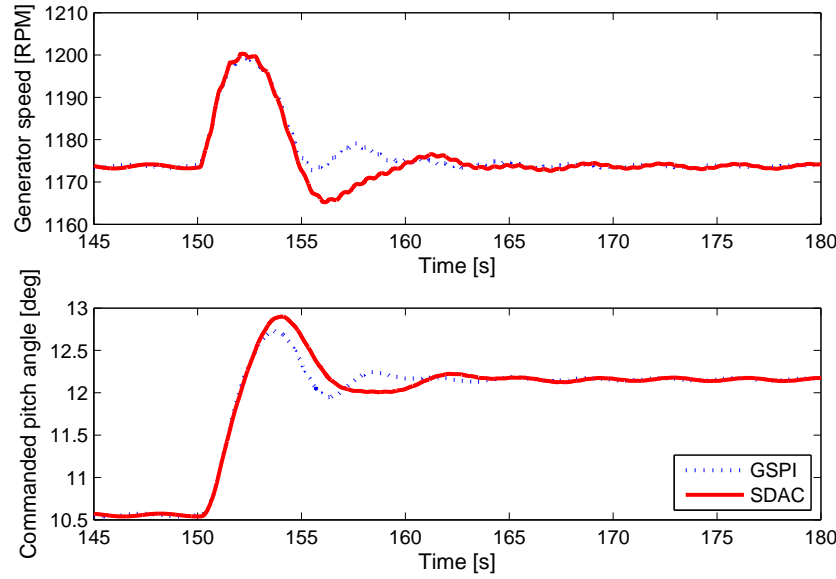


Figure 3.6: Similar generator speed responses of GSPI and SDAC after tuning the \mathbf{Q} .

Speed regulation of each controller is compared in terms of the RMS generator speed error in Fig. 3.8(a). The two controllers achieved the desired similar performance at the reference mean wind velocity. Further, the maximum generator speed error is compared in Fig. 3.8(b).

In term of the RMS generator speed error, a distinct trend between the controllers is observed across the tested mean wind velocities with similar turbulence class. The GSPI controller shows an expected trend in which the best speed regulation is achieved at the reference mean wind velocity of 16 m/s. Having been designed to take into account the nonlinear WT aerodynamics, the GSPI controller performs much better than a PI controller. Nonetheless, the GSPI controller cannot completely eliminate the performance degradation due to nonlinearity. On the other hand, having been designed as a linear controller, the SDAC shows a different trend in which the median and variation of the RMS speed error decreases as the mean wind velocity increases. One explanation of this can be offered through investigation of the instantaneous wind velocity. Previous study on the high-order controller for another WT, designed considering all WT flexibilities, has shown that the performance of DAC deteriorates as the wind velocity approaches the rated velocity [5]. As the mean wind velocity decreases, there are more occurrences of the instantaneous wind velocity near its rated value. This performance deterioration of SDAC at the wind velocities close to the rated value can be improved by gain scheduling of the SDAC gains. Nevertheless, in terms of both

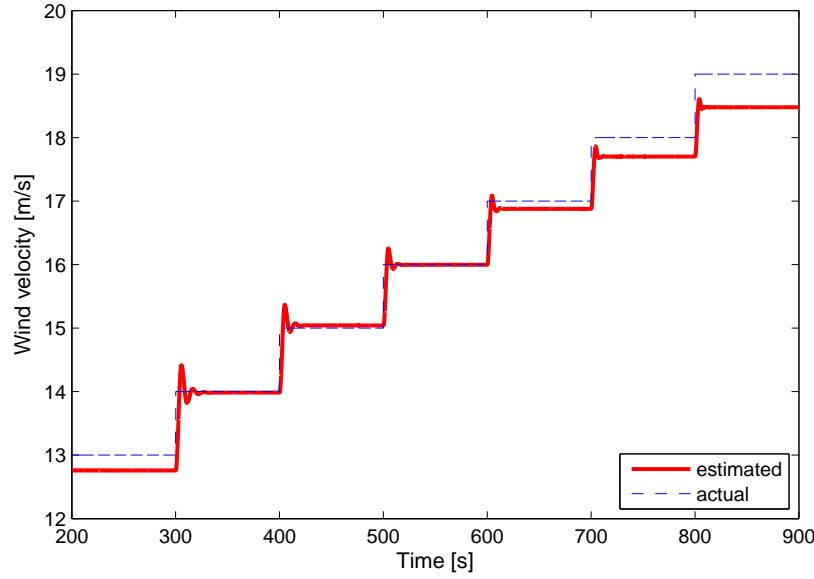
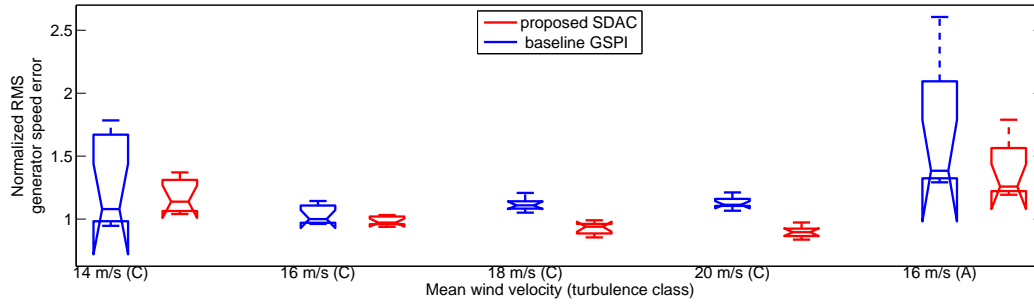


Figure 3.7: Estimated and actual wind velocity of SDAC.

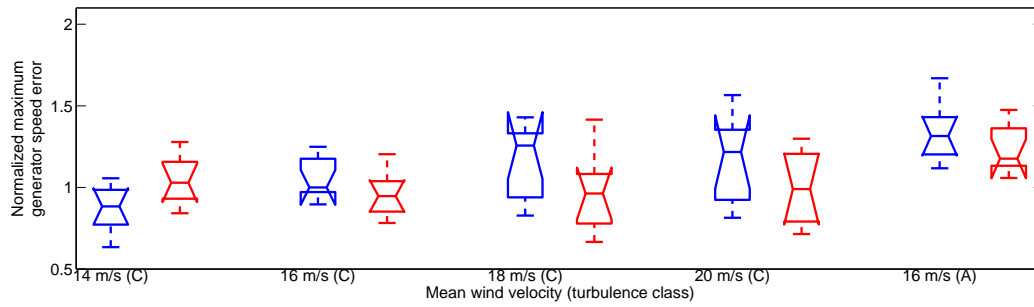
RMS and maximum speed errors, the proposed SDAC gives significant improvement for the mean wind velocities higher than the reference mean wind velocity and insignificant difference from that of GSPI for the ones lower or equal to the reference wind velocity. Therefore, the proposed SDAC conclusively improves the speed regulation across the tested mean wind velocities. Furthermore, though higher turbulence intensity leads to deterioration of generator speed response, as shown in Fig. 3.8(a), the SDAC results in lower speed error. This is an expected result as the controller formulation has taken into account the variations in wind velocity due to turbulence through the process noise covariance matrix \mathbf{Q} .

The added value of using two-mass drivetrain model is the ability to regulate dynamic loads experienced by the drivetrain due to the induced torsional deflections. It is accomplished by adjusting the closed-loop pole locations related to the torsional vibration of the drivetrain. This is validated in Fig. 3.8(c), in which the drivetrain loads of SDAC across different mean wind velocities and turbulence intensity are statistically lower than those of the GSPI controller, which does not take into account the flexibility of the drivetrain.

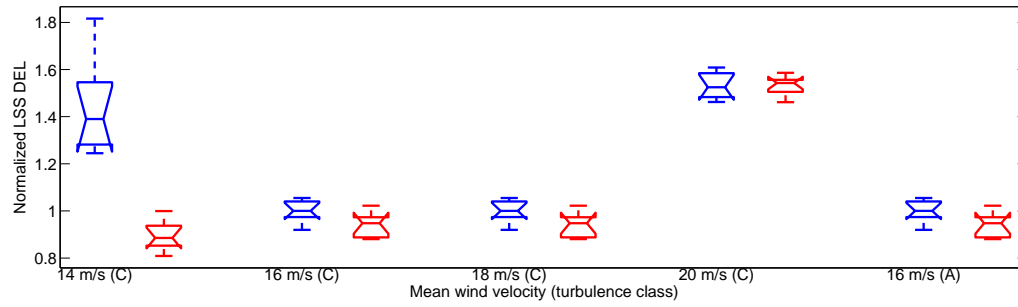
Figure 3.8(d) shows that the achievement of better speed regulation and lower drivetrain load of the SDAC generally comes with a higher control cost than that of the GSPI controller, which does not aim to mitigate the drivetrain load. However, the SDAC costs less at low mean wind velocity



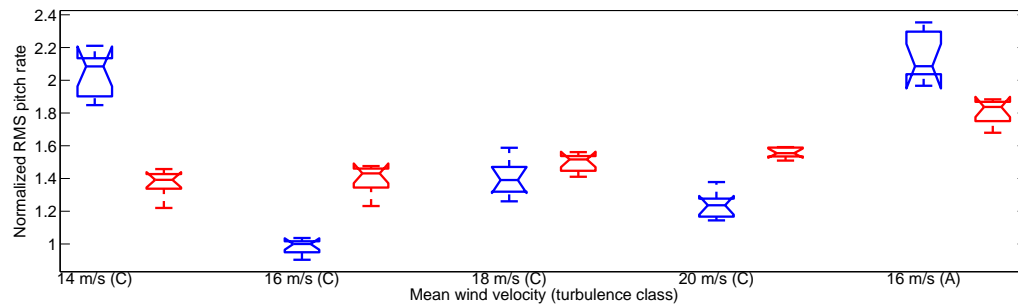
(a)



(b)



(c)



(d)

Figure 3.8: Performance comparisons between GSPI and SDAC under turbulent wind.

and high turbulence intensity. At such conditions, the instantaneous wind velocity more often interchanges between regions 2 and 3, contributing to the windup issue for the GSPI controller. Not only does this issue create high fluctuations in the rotational speed, as shown in Fig. 3.8(a), but it also forces the pitching actuation to saturate at its maximum rate of $8^\circ/\text{s}$.

3.5 Chapter Conclusions

This chapter presents the use of Kalman estimator in designing SDAC for CPC to stabilize the closed-loop system with unmodeled dynamics. Previous studies have highlighted the undesirable and destabilizing effects of the unmodeled higher-order structural dynamics on the previous designs of DAC for WT applications. This problem has successfully been addressed in this chapter using the proposed control scheme. To investigate the performance of the proposed SDAC against a stable baseline CPC, simulations were performed under turbulent wind conditions with various mean velocities and turbulence intensities. This chapter has shown that the SDAC is shown to improve the power quality up to 20.8%, while resulting in lower drivetrain load up to 22.5% as compared with the industrial-standard CPC. It was expected that the additional objective of dampening the drivetrain load will increase the control cost. Nonetheless, due to the nature of turbulent wind and the implementation of integral anti windup in the GSPI controller, the proposed SDAC can sometime result in a lower control cost.

Chapter 4

Pitch Controller to Mitigate Load considering Yaw Misalignment

4.1 Introduction

Collective pitch controllers (CPCs) are inherently not able to take into account the blade load variations caused by the vertical wind shear. Therefore, the individual pitch controller (IPC) was introduced, which requires additional sensors to measure the blade-root moments [51–53]. Since its introduction, various design alternatives and improvements have been proposed for IPC [47, 54–57], all of which were designed considering the effects of changing wind velocity and asymmetric aerodynamic loading due to wind shear to simultaneously maintain the WT rated speed (or power) and mitigate the blade load variations. In the designs of all these proposed IPCs, the wind field is assumed to have no misalignment with respect to the rotor plane.

A recent study has shown that yaw misalignment at certain angular positions can mitigate the blade load variations [6]. It suggested that the optimum yaw misalignment angle, which yield the lowest blade load variations, can be estimated based on the mean wind velocity, shear magnitude, and turbulence intensity. Further, it proposed a strategy in which the yaw controller holds the WT at the optimum angle while the WT operates at region 3 operation through implementation of a CPC, which is independent from the yaw controller. However, such yaw control strategy requires a reliable sensor to capture the conditions of the oncoming wind in order to decide the optimum yaw misalignment angle. Further, while the intentional yaw misalignment reduces the blade load at constant wind velocity and varying wind velocity with low turbulence intensity, the blade load alleviation at high turbulence intensity is insignificant.

This chapter presents a multi-input-multi-output (MIMO) IPC based on linear quadratic regulator (LQR) design that takes into account the benefit of yaw misaligned condition to alleviate

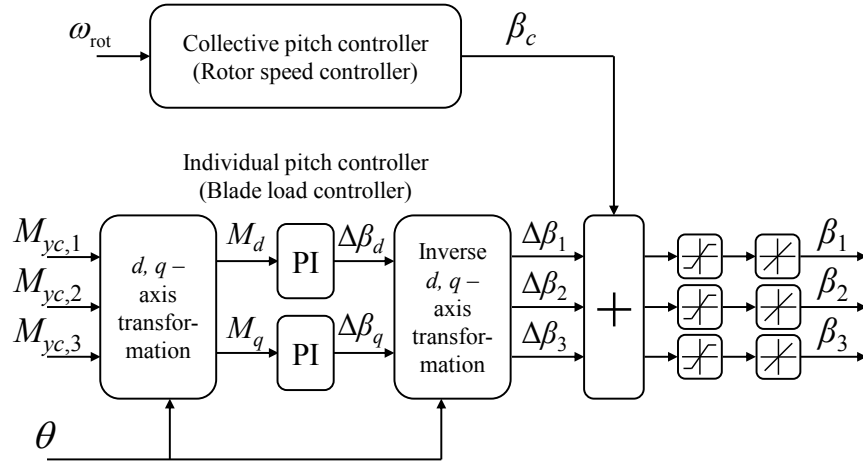


Figure 4.1: Schematic of the baseline IPC.

the blade loads. The reference point for the design of this controller is the one in which the WT operates in a yawed inflow condition that yields lower blade loads than if it operates with zero yaw misalignment. Nevertheless, the controller is intended for implementation on WTs with conventional yaw control strategy that aligns the WTs with the wind. Thus, there is neither intentional yaw misalignment nor coupling between the proposed MIMO IPC and the yaw controller. Also, the proposed controller does not require any sensors to capture the wind conditions. This chapter also considers the NREL 5-MW reference WT for controller design and verification.

4.2 Baseline Pitch Controllers

There are three baseline pitch controllers considered in this chapter, two of which regulate the collective pitch angle and another one regulates distinct pitch angle for each blade. The baseline CPC design is the SISO GSPI controller depicted in Fig. 2.12 with an anti windup gain $K_{aw} = 10$. One of the two CPC implementations in this chapter considers that the WT is aligned with the wind (i.e., 0° yaw angle) while the other considers that it is intentionally misaligned at the optimum angle, if such an angle exists, that yields the lowest blade-root OOP bending moment.

The baseline IPC design is defined in [52, 53] and shown in Fig. 4.1. It consists of independent rotor speed controller and blade loads controller. The rotor speed controller is the baseline CPC and the blade load controller is designed to take into account the wind shear effect. The spatially

varying wind velocity across the rotor plane causes asymmetric loadings, alleviating which requires independent regulation of each pitch angle. For this control loop, the blade-root OOP bending moments of each blade $M_{yc,i}$, measured in a reference frame that rotates with the WT rotor, are transformed to tilt moment M_d and yaw moment M_q in the direct and quadrature axes of a nonrotating frame as follows

$$\begin{Bmatrix} M_d \\ M_q \end{Bmatrix} = \frac{2}{3} \begin{bmatrix} \cos(\theta) & \cos(\theta + \frac{2\pi}{3}) & \cos(\theta + \frac{4\pi}{3}) \\ \sin(\theta) & \sin(\theta + \frac{2\pi}{3}) & \sin(\theta + \frac{4\pi}{3}) \end{bmatrix} \begin{Bmatrix} M_{yc,1} \\ M_{yc,2} \\ M_{yc,3} \end{Bmatrix} \quad (4.1)$$

where θ is the measured rotor azimuth, with $\theta = 0$ is where blade 1 is aligned with the z - axis, as shown in Fig. 2.13(a). It has been shown that the transformation decouples the collective pitch angle controller that regulates the rotor speed from the individual pitch angle controller that mitigates the blade load variations [54]. This in turn allows combining this blade load controller with various designs of CPC [58].

As the results of orthogonal transformation, the tilt and yaw moments can be considered as decoupled loads [51–53]. Thus, a PI controller can be designed to bring down each load component to zero. The outputs of the controllers, $\Delta\beta_d$ and $\Delta\beta_q$, are inverse transformed by

$$\begin{Bmatrix} \Delta\beta_1 \\ \Delta\beta_2 \\ \Delta\beta_3 \end{Bmatrix} = \begin{bmatrix} \cos(\theta) & \sin(\theta) \\ \cos(\theta + \frac{2\pi}{3}) & \sin(\theta + \frac{2\pi}{3}) \\ \cos(\theta + \frac{4\pi}{3}) & \sin(\theta + \frac{4\pi}{3}) \end{bmatrix} \begin{Bmatrix} \Delta\beta_d \\ \Delta\beta_q \end{Bmatrix} \quad (4.2)$$

to define them back in the rotating frame. Finally, the transformed pitch angles $\Delta\beta_i$ are summed with the collective pitch angle to be the individual pitch control commands β_i^* for each actuator.

4.3 Effects of Yaw Misalignment

The aerodynamics of WT in yawed inflow condition and the resulting mitigation of blade load variations amidst wind shear are explained in detail in [6]. To demonstrate the mitigation effect of

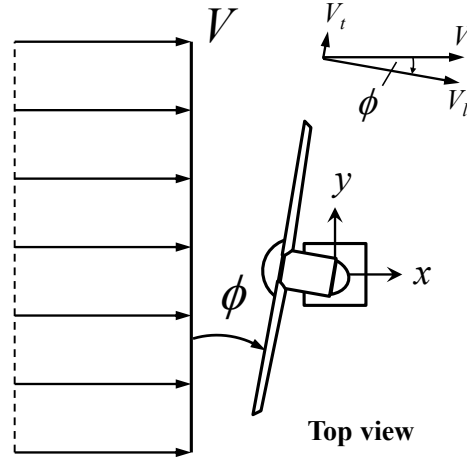


Figure 4.2: Top view of wind shear and yaw misalignment on WT in Fig. 1.2.

yaw misalignment, the exponential vertical shear model shown in Figs. 1.2 and 4.2 is used

$$V(z) = V_h \left(\frac{z}{z_h} \right)^\alpha \quad (4.3)$$

where V_h is the wind velocity at the hub-height z_h and z is the height above the ground. The IEC standard recommends a wind shear exponent of $\alpha = 0.2$ for onshore WTs [15]. Looking at the WT from top, the yaw misalignment angle ϕ is measured positively clockwise from the effective wind direction to the axis perpendicular to the rotor plane. (i.e., $\phi > 0$ in Figs. 1.2 and 4.2). The wind velocity V can be decomposed into the longitudinal V_l and translational V_t components, which are perpendicular and parallel to the rotor plane, respectively.

A set of simulations using FAST were performed at different yaw misalignment angles ϕ and constant hub-height wind velocity V_h to evaluate the blade load variations under sheared wind flow governed by Eq.(4.3) with the WT operating using the baseline CPC. Simulations using the baseline CPC represents the nominal operating conditions for linearization, in which the rate of change of the WT speed and blade pitch angles are small (i.e., the system inputs and output are nearly constant at equilibrium).

The blade load variation is represented by the peak-to-peak range of the resulting steady-state blade-root OOP bending moment of the first blade $\delta M_{yc,1}$, whose value is equal for all blades. The load variation is then normalized with respect to the peak-to-peak bending moment at zero

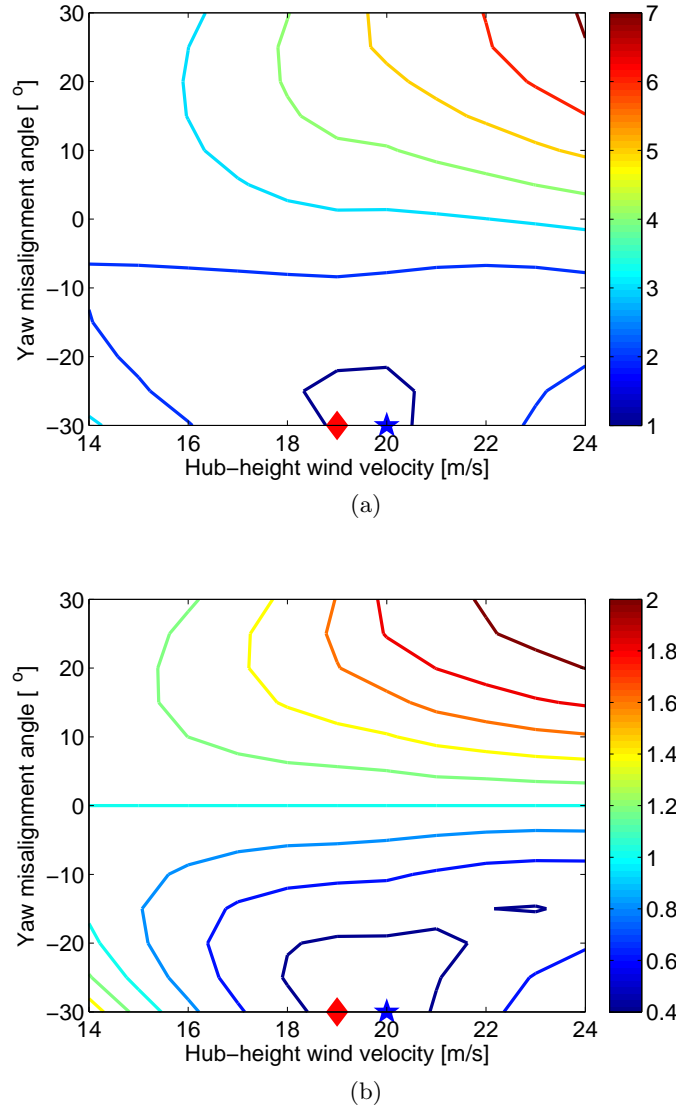


Figure 4.3: Simulated blade OOP loads under combined influences of wind shear and yaw misalignment for the baseline CPC: (a) peak-to-peak range (b) normalized peak-to-peak range.

misalignment as

$$\overline{\delta M_{yc,1}}(V_h, \phi) = \frac{\delta M_{yc,1}(V_h, \phi)}{\delta M_{yc,1}(V_h, 0)} \quad (4.4)$$

The peak-to-peak ranges and normalized values are shown in Fig. 4.3 as a function of yaw misalignment angle and wind velocity. It is important to highlight that for all cases the WT output power was successfully maintained at its rated value. The asymmetry in Fig. 4.3 stems from the fact that the rotor is rotating clockwise, seen from upwind, as shown in Fig. 1.2. If the rotor is yawed in the positive direction, as shown in Fig. 4.2, the translational wind velocity V_t (in positive

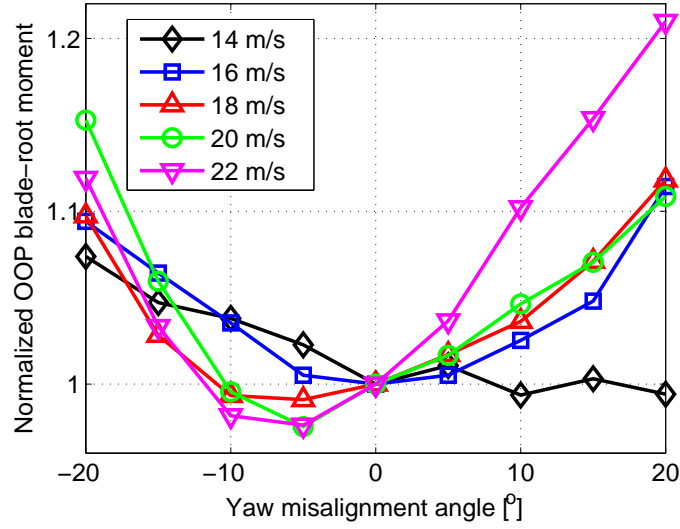


Figure 4.4: Simulated blade OOP loads under class C turbulent winds with different mean wind velocities.

y - direction) adds to the blade load fluctuations, as reflected in Fig. 4.3 Conversely, if the rotor is yawed in negative direction, the translational wind velocity V_t (this time in negative y - direction), dampens the blade load fluctuation.

Pitch controllers described so far have been designed at zero yaw misalignment angle. However, Fig. 4.3 shows that negative yaw misalignment angles yield lower load variations, with the lowest variation occurring at the operating condition marked by the pentagram. This implies that common pitch controllers are designed based on conditions having nearly three times higher blade OOP load than the lowest achievable load through yaw misalignment.

For the case of turbulent wind with the baseline CPC, the optimum yaw misalignment angle varies according to the mean wind velocity and turbulence intensity. Figure 4.4 illustrates the optimum yaw misalignment angles for cases with similar turbulence class but different mean wind velocities at region 3 operation. Each data point represents an average of six values of 1-Hz DEL normalized with respect to the averaged DEL at zero misalignment angle. At mean velocity of 14 m/s, the optimum yaw misalignment angle does not exist and absolute yaw misalignment angles larger than 20° at this wind mean velocity results in severe windup issues. At mean velocity of 16 m/s, the intentional yaw misalignment does not assist the blade load mitigation. Meanwhile, at higher mean wind velocities, a range of negative yaw misalignment angles yield lower blade

load with the best improvement of 2.5% at -5° . This observation presents key challenges in implementing the baseline CPC with intentional yaw misalignment on the a WT. Firstly, a reliable sensor is imperative not only to measure but also to monitor wind velocities for some period of time to sufficiently determine the mean velocity and turbulence intensity according to Eq. (2.1). Secondly, the optimum yaw misalignment angle for turbulent wind can only be determined through simulations, such as the one performed to obtain the results in Fig. 4.4. Many more simulations have to be performed to obtain the complete set of optimum yaw misalignment angles at various turbulent wind conditions to which a WT may be exposed. Lastly, it is important for the yaw controller and drive to deliver accurate yaw misalignment angle as small deviation, especially in the positive yaw misalignment angle, may result in amplification of the blade load.

4.4 Proposed Controller Design

To yield a pitch controller that results in a superior blade load mitigation, a MIMO controller designed based on a model linearized at the operating condition marked by the diamond in Fig. 4.3 is proposed in this chapter. This condition was chosen instead of that with the lowest blade load because its correspondingly lower wind velocity is located in the middle of the region 3 operating region, thus improving the speed regulation across the range of wind velocities at region 3 operation.

A linearized model is obtained for the NREL 5-MW reference WT in a sheared and yawed inflow condition with a hub-height wind velocity $V_h = 19$ m/s, yaw misalignment angle $\phi = -30^\circ$, and shear exponent $\alpha = 0.2$ at a defined number of equally spaced rotor azimuth θ of the form of Eq. (2.2), where the states consider the generator rotation and first flapwise mode of each blade, which are the minimum DOFs required to capture the dynamics of the rotor speed and blade loads. The states, control inputs, and disturbance inputs of the linearized model are respectively defined as

$$\begin{aligned}\Delta \mathbf{x}_F &= \left\{ \Delta \theta \quad \Delta f_1 \quad \Delta f_2 \quad \Delta f_3 \quad \Delta \dot{\theta} \quad \Delta \dot{f}_1 \quad \Delta \dot{f}_2 \quad \Delta \dot{f}_3 \right\}^T \\ \Delta \mathbf{u}_F &= \left\{ \Delta \beta_1 \quad \Delta \beta_2 \quad \Delta \beta_3 \right\}^T \\ \Delta \mathbf{u}_d &= \left\{ \Delta V_l \quad \Delta \phi \right\}^T\end{aligned}$$

where f_i is the flapwise tip deflection of the i^{th} blade.

The states associated with the blade tip DOF, f_i and \dot{f}_i , are defined and measured in the rotating reference frame. To assist in the controller design, multi-blade coordinate (MBC) transformation, which is a more general form of the d, q - axis transformation, is applied to transform all measurements to the nonrotating reference frame. MBC transformation for WT applications is discussed in detail in [59]. The disturbance states, which have been defined in the nonrotating frame, take into account the changes in both hub-height longitudinal wind velocity and yaw misalignment angle.

For the defined states and control inputs, the transformation from the nonrotating frame to the rotating one are defined as

$$\Delta \mathbf{x}_F = \mathbf{T}_s \Delta \mathbf{x}_{\text{NR}} \quad (4.5)$$

$$\Delta \mathbf{u}_F = \tilde{\mathbf{t}} \Delta \mathbf{u}_{\text{NR}} \quad (4.6)$$

where the transformation matrices are defined as

$$\begin{aligned} \mathbf{T}_s &= \begin{bmatrix} \mathbf{T}_1 & 0 \\ \dot{\theta} \mathbf{T}_2 & \mathbf{T}_1 \end{bmatrix}, \\ \tilde{\mathbf{t}} &= \begin{bmatrix} 1 & \cos(\theta) & \sin(\theta) \\ 1 & \cos(\theta + \frac{2\pi}{3}) & \sin(\theta + \frac{2\pi}{3}) \\ 1 & \cos(\theta + \frac{4\pi}{3}) & \sin(\theta + \frac{4\pi}{3}) \end{bmatrix}, \\ \mathbf{T}_1 &= \begin{bmatrix} 1 & 0 \\ 0 & \tilde{\mathbf{t}} \end{bmatrix}, \\ \mathbf{T}_2 &= \begin{bmatrix} 0 & 0 & 0 & 0 \\ 0 & 0 & -\sin(\theta) & \cos(\theta) \\ 0 & 0 & -\sin(\theta + \frac{2\pi}{3}) & \cos(\theta + \frac{2\pi}{3}) \\ 0 & 0 & -\sin(\theta + \frac{4\pi}{3}) & \cos(\theta + \frac{4\pi}{3}) \end{bmatrix} \end{aligned}$$

The states and control inputs in the nonrotating frame are defined as

$$\begin{aligned}\Delta \mathbf{x}_{\text{NR}} &= \left\{ \Delta \theta \quad \Delta f_0 \quad \Delta f_c \quad \Delta f_s \quad \Delta \dot{\theta} \quad \Delta \dot{f}_0 \quad \Delta \dot{f}_c \quad \Delta \dot{f}_s \right\}^T \\ \Delta \mathbf{u}_{\text{NR}} &= \left\{ \Delta \beta_c \quad \Delta \beta_d \quad \beta_q \right\}^T\end{aligned}$$

where f_0 , f_c , and f_s are respectively the static, cosine-cyclic, and sine-cyclic components of the flapwise blade-tip deflections. The linearized state-space model in the nonrotating frame can be expressed as

$$\Delta \dot{\mathbf{x}}_{\text{NR}} = \mathbf{A}_{\text{NR}}(\theta) \Delta \mathbf{x}_{\text{NR}} + \mathbf{B}_{\text{NR}}(\theta) \Delta \mathbf{u}_{\text{NR}} + \mathbf{B}_{d,\text{NR}}(\theta) \Delta \mathbf{u}_d \quad (4.7)$$

where

$$\begin{aligned}\mathbf{A}_{\text{NR}}(\theta) &= \begin{bmatrix} \mathbf{T}_1^{-1} & 0 \\ 0 & \mathbf{T}_1^{-1} \end{bmatrix} \left(\mathbf{A}_F(\theta) \mathbf{T}_s - \begin{bmatrix} \dot{\theta} \mathbf{T}_2 & 0 \\ \dot{\theta}^2 \mathbf{T}_3 + \ddot{\theta} \mathbf{T}_2 & 2\dot{\theta} \mathbf{T}_2 \end{bmatrix} \right) \\ \mathbf{T}_3 &= \begin{bmatrix} 0 & 0 & 0 & 0 \\ 0 & 0 & -\cos(\theta) & -\sin(\theta) \\ 0 & 0 & -\cos(\theta + \frac{2\pi}{3}) & -\sin(\theta + \frac{2\pi}{3}) \\ 0 & 0 & -\cos(\theta + \frac{4\pi}{3}) & -\sin(\theta + \frac{4\pi}{3}) \end{bmatrix} \\ \mathbf{B}_{\text{NR}}(\theta) &= \begin{bmatrix} \mathbf{T}_1^{-1} & 0 \\ 0 & \mathbf{T}_1^{-1} \end{bmatrix} \mathbf{B}_F(\theta) \\ \mathbf{B}_{d,\text{NR}}(\theta) &= \begin{bmatrix} \mathbf{T}_1^{-1} & 0 \\ 0 & \mathbf{T}_1^{-1} \end{bmatrix} \mathbf{B}_{d,F}(\theta)\end{aligned}$$

Finally, the state-space model is averaged to give the LTI system model used for controller design

$$\Delta \dot{\mathbf{x}}_{\text{NR}} = \mathbf{A}_{\text{NR}} \Delta \mathbf{x}_{\text{NR}} + \mathbf{B}_{\text{NR}} \Delta \mathbf{u}_{\text{NR}} + \mathbf{B}_{d,\text{NR}} \Delta \mathbf{u}_d \quad (4.8)$$

where each matrix is averaged over N azimuth angles θ_l similar to that of Eq. (2.6).

Since $(\mathbf{A}_{\text{NR}}, \mathbf{B}_{\text{NR}})$ is controllable and assuming that all the states are available through mea-

surement, a nominal feedback control law can be designed as $\Delta \mathbf{u}_{\text{NR}} = -\mathbf{K}\Delta \mathbf{x}_{\text{NR}}$. Linear quadratic regulator (LQR) theory was used to obtain the optimal static gain matrix that minimizes the following cost function

$$J(\Delta \mathbf{u}_{\text{NR}}) = \int_0^\infty (\Delta \mathbf{x}_{\text{NR}}^T \mathbf{Q} \Delta \mathbf{x}_{\text{NR}} + \Delta \mathbf{u}_{\text{NR}}^T \mathbf{R} \Delta \mathbf{u}_{\text{NR}}) dt \quad (4.9)$$

In this work, the quadratic cost function was defined using the weighting matrices of $\mathbf{Q} = \text{diag}([12, 0.5, 0.5, 0.5, 0.5, 0.1, 0.1, 0.1])$ and $\mathbf{R} = \text{diag}([75, 150, 150])$.

All eigenvalues of the designed closed-loop system (i.e., $\text{eig}(\mathbf{A}_{\text{NR}} - \mathbf{B}_{\text{NR}}\mathbf{K})$) are in the left-hand side of the imaginary axis, as shown in Fig. 4.5. Because the controller is to be implemented on a WT with flexible blades, drivetrain, and tower, it is important to ensure that all of the closed-loop eigenvalues of the higher-order system under the designed feedback law are also in the stable region. To do so, the previously described linearization, transformation, and averaging process was repeated on a WT model with full flexibility (i.e., all of the 16 available DOFs were activated) resulting in a 32-state LTI state-space equation. The designed feedback gains \mathbf{K} were then applied on the eight states of $\Delta \mathbf{x}_{\text{NR}}$ while no feedback was applied on the remaining 24 states. As shown in Fig. 4.5, the actual closed-loop eigenvalues are in some distance from the designed locations. Nonetheless, there is no unstable pole in the actual higher-order closed-loop system.

The output equation in the nonrotating frame can also be obtained through FAST linearization, MBC transformation, and averaging process to provide the LTI form as

$$\Delta \mathbf{y}_{\text{NR}} = \left\{ \Delta \dot{\theta} \quad \Delta M_0 \quad \Delta M_d \quad \Delta M_q \right\}^T = \mathbf{C}_{\text{NR}} \Delta \mathbf{x}_{\text{NR}} + \mathbf{D}_{\text{NR}} \Delta \mathbf{u}_{\text{NR}} + \mathbf{D}_{d,\text{NR}} \Delta \mathbf{u}_d \quad (4.10)$$

The impacts of wind disturbances, in terms of variation in lateral wind velocity ΔV_l and inflow angle $\Delta \phi$, on the blade OOP loads across the frequencies appropriately investigated using FAST are depicted in Fig. 4.6. In general, the designed closed-loop system mitigate the three components of the blade loads amidst these disturbances. In particular, substantial mitigation occurs for frequency components of 0.1 Hz and above.

The output of the nominal feedback control is gain-scheduled to compensate for the nonlinear WT aerodynamics. A gain-scheduling scheme was implemented following the method in [60], which

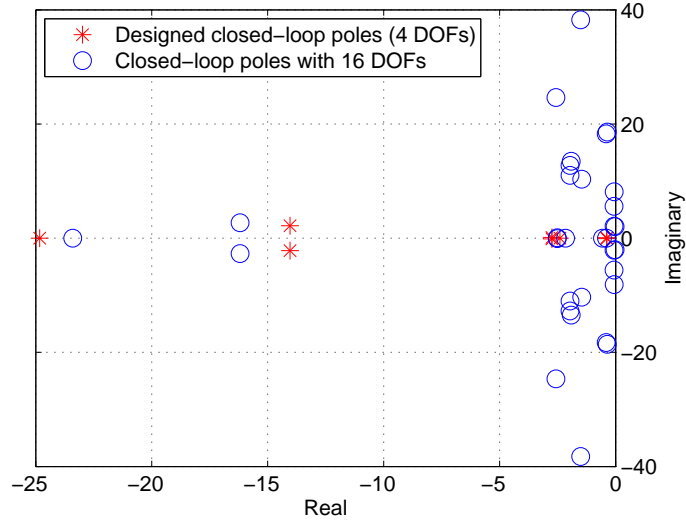


Figure 4.5: Designed closed-loop eigenvalues based on lower-order WT model (4 DOFs) and actual closed-loop eigenvalues based on fully flexible WT model (16 DOFs).

is shown in Fig. 4.7. The gain-scheduled individual pitch angle is defined as

$$\beta_i^* = G_2(\hat{\beta}_i)\hat{\beta}_i \quad (4.11)$$

where

$$G_2(\hat{\beta}_i) = \frac{1}{1 + \frac{\hat{\beta}_i - \psi_1}{\psi_2}}$$

with $\psi_1 = 6.6^\circ$ and $\psi_2 = 23.5^\circ$ respectively referring to the nominal pitch angles at the rated and cut-out wind velocities.

In the case of turbulent winds, the instantaneous wind velocity can drop to below the rated wind velocity for a while before coming back to the above the rated wind velocity. This occasionally results in windup as the blade pitch angle has a lower limit of 0° . Anti windup is therefore designed and implemented following the back-calculation scheme for the baseline CPC, the output of which is added to the measured rotor azimuth angle (i.e., integral of the rotor speed) to make up for the first WT state. The scheme is depicted in Fig. 4.8.

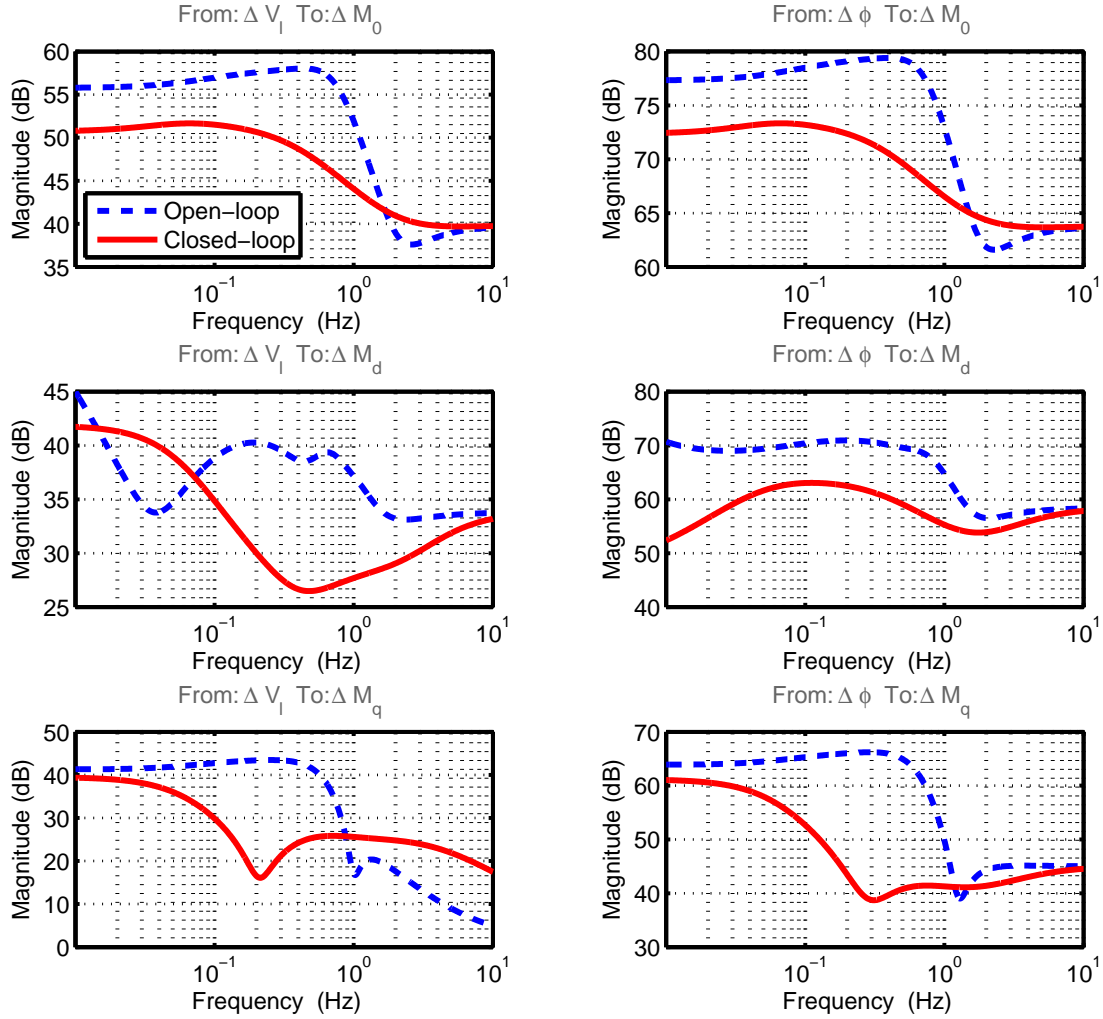


Figure 4.6: Bode plots from the disturbances to the components of blade-root OOP bending moment under the designed MIMO IPC.

4.5 Simulation Results

The simulations were conducted using turbulent winds with various mean wind velocities and turbulence intensities. The length of each simulation is 700-second, out of which the first 100-second was reserved for the simulation startups. For each controller, five mean wind velocities within the region 3 operation with turbulence class C were considered. Also, two other different turbulence intensities were evaluated at the mean wind velocity of 18 m/s. Another turbulence intensity of 5%,

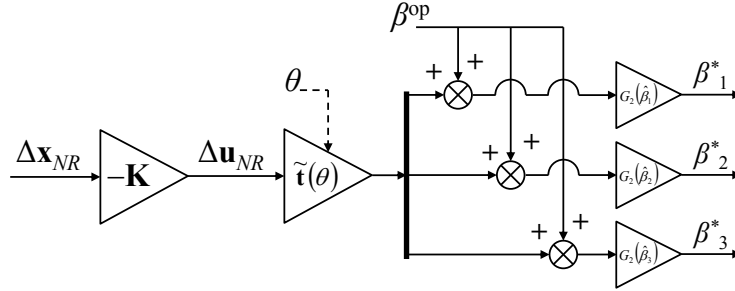


Figure 4.7: Gain-scheduling of the proposed controller.

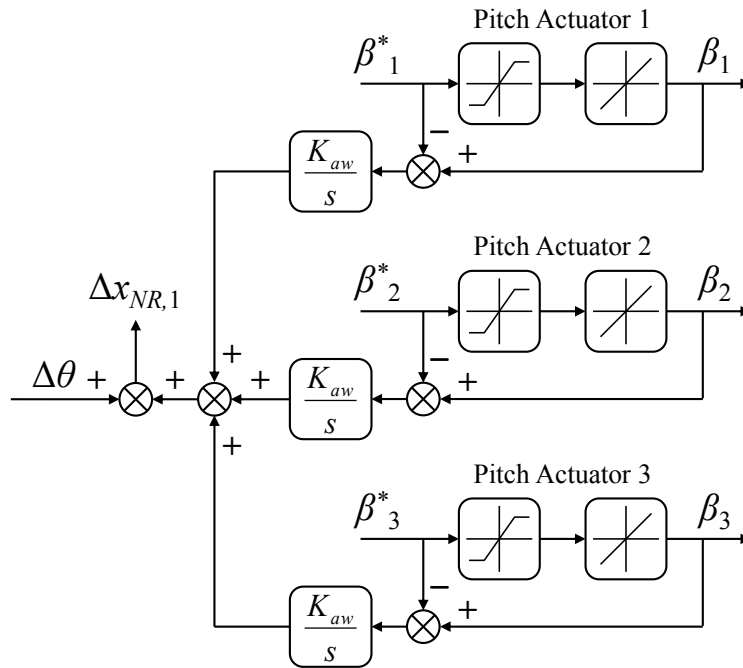


Figure 4.8: Back-calculation scheme for the proposed controller.

which is lower than that of class C, was considered to verify the control performance at relatively steady winds. Six different turbulence seeds were used for each case, resulting in a total number of 42 simulations for each of the tested control schemes. In simulating the WT loads using FAST, the mean wind direction is zero and the WT model considered all structural flexibilities, except for the yaw DOF.

Based on Fig. 4.4, two control schemes based on the baseline CPC were tested for 18 m/s (C), 20 m/s (C), and 22 m/s (C). One was without misalignment and another was at a fixed yaw misalignment angle of -5° for the lowest blade OOP load. For the case of 18 m/s (5%), the

optimum yaw misalignment angle is -15° . The baseline CPC for the turbulence cases of 14 m/s (C), 16 m/s (C) and 18 m/s (A) were only tested without misalignment because of the nonexistence of optimum yaw misalignment angle besides 0° .

Relative performance among the controllers is compared in terms of speed regulation and structural loads. The speed regulation, which is directly related to power regulation, is compared using the RMS and maximum value of the generator speed error from its rated speed. The structural loads are represented by the DELs of the blade-root OOP and IP bending moments of the first blade as well as the tower-base FA and side-to-side SS bending moments. Notched boxplot for each performance metric is again plotted side by side for graphical comparison to highlight the difference among the data groups.

4.5.1 Speed regulation

In order to standardize the comparison, the baseline CPC without misalignment, baseline IPC, and MIMO IPC were tuned to achieve similar RMS generator speed error at 18 m/s (C), as verified in Fig. 4.9. This resulted in PI gains of $K_P = 1.53$ and $K_I = 0.78$ for the baseline CPC, which were maintained for the case of baseline CPC with the optimum yaw misalignment angle. Since the baseline CPC without misalignment is treated as the benchmark, all performance metrics were normalized with respect to the median of the corresponding metric of the baseline CPC without misalignment at 18 m/s (C).

The RMS generator speed errors of all controllers are compared in Fig. 4.9. Having similar design that governs the WT speed, the baseline CPC and IPC share similar RMS speed error response. The baseline IPC yields slightly higher mean and variation in RMS speed error due to occasional saturations of the pitch actuators, attributed to the additional pitch demands by the blade load controller. The RMS speed error response of the proposed MIMO IPC improves as the mean wind velocity increases, while the speed variation is the highest at the lowest mean wind velocities of 14 m/s (C). This phenomenon, in which a full-state feedback controller yields deterioration in speed regulation as the wind velocity approaches the rated speed, is consistent with the one observed in Fig. 3.8(a) and has also been reported in [5]. Nonetheless, in term of the RMS generator speed errors, all controllers perform similarly.

Higher turbulence intensity, represented by 18 m/s (A), understandably causes higher RMS

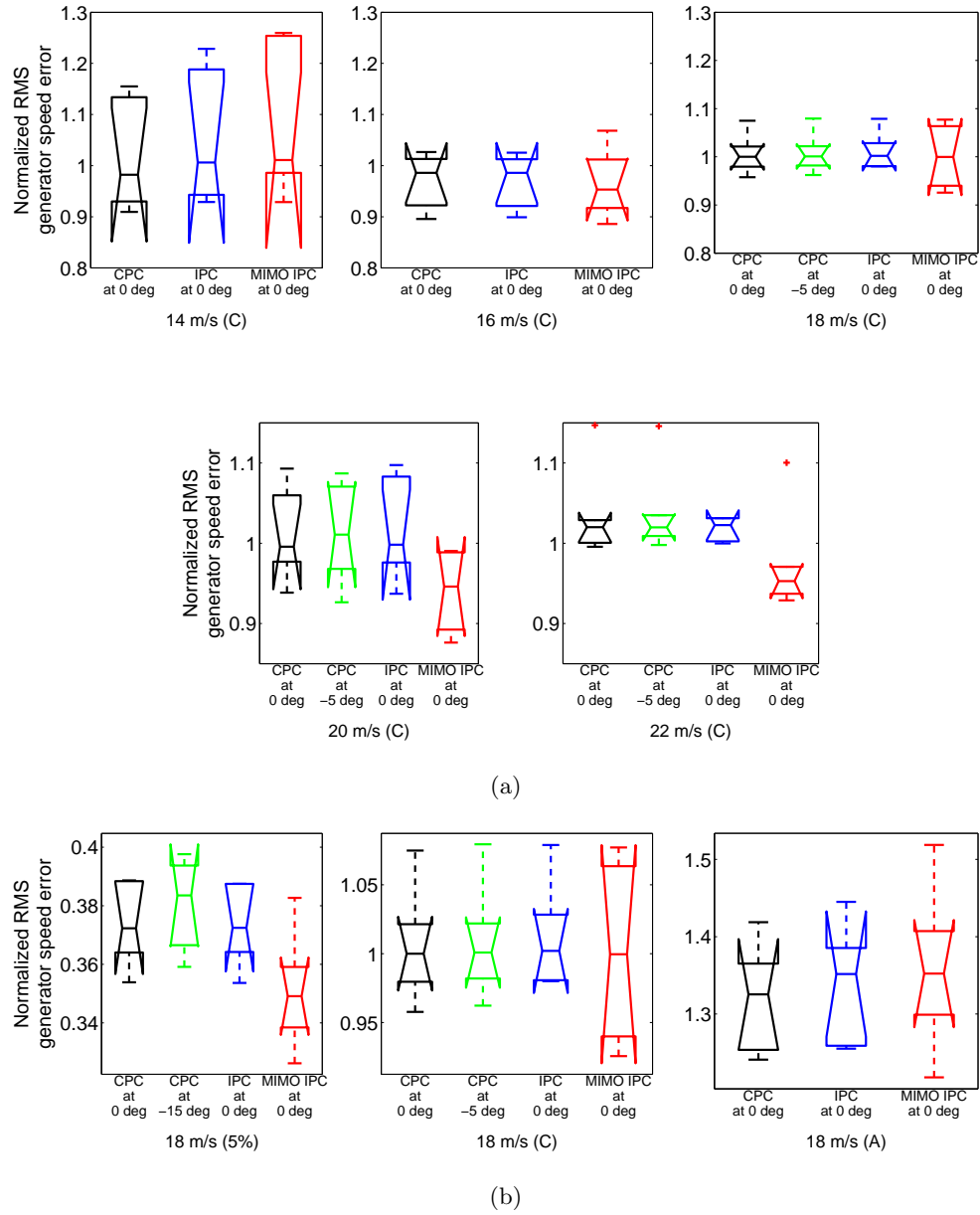


Figure 4.9: Comparison of the controllers in term of RMS generator speed error at various (a) mean wind velocities and (b) turbulence intensities.

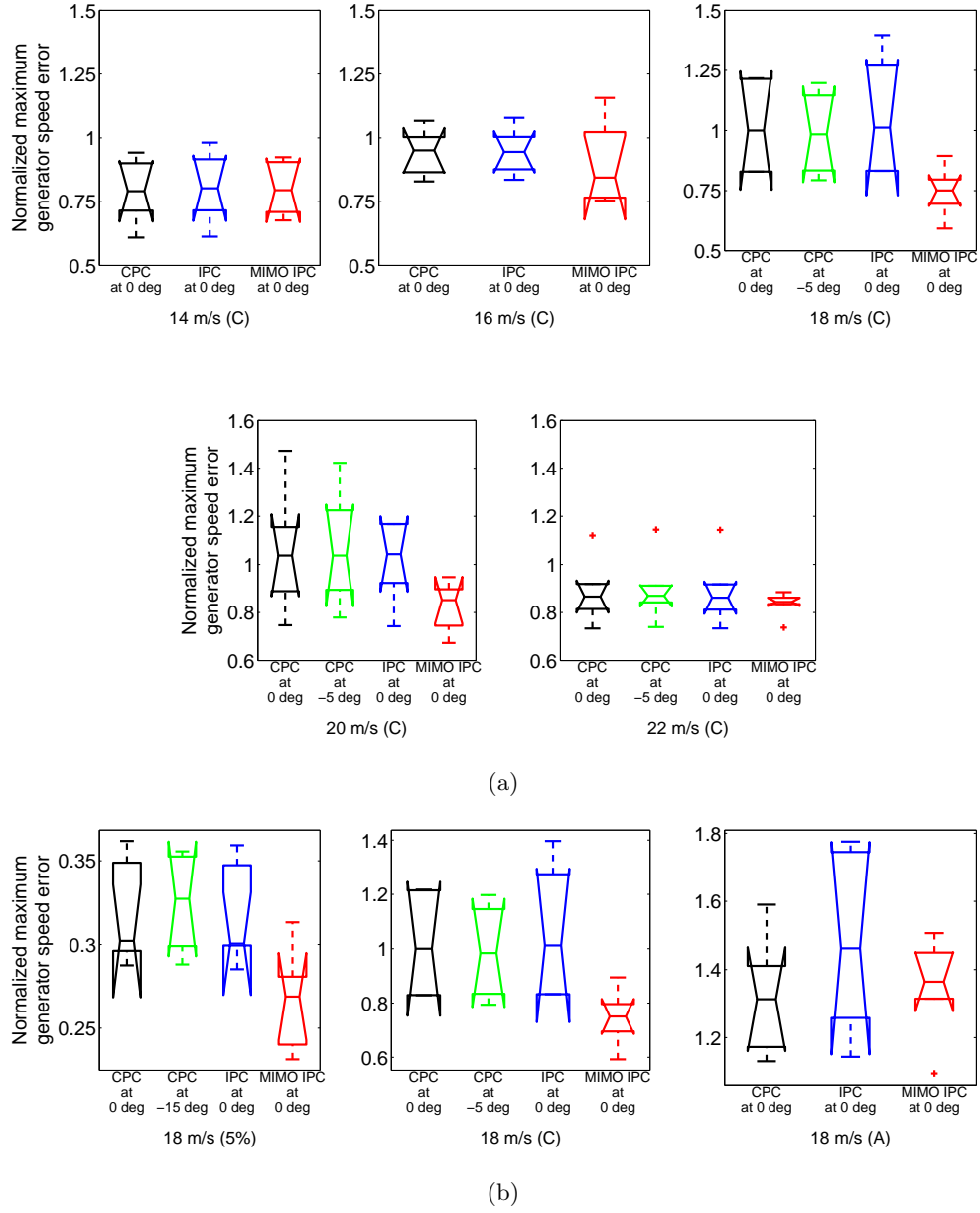


Figure 4.10: Comparison of the controllers in term of maximum generator speed error at various
 (a) mean wind velocities and (b) turbulence intensities.

speed errors, as shown in Fig. 4.9(b). At this condition, the occurrence of actuator saturations attributed to the baseline IPC is more prominent, resulting in higher RMS speed error. Nonetheless, there is no significant difference among the controllers across the turbulence intensities, except at the lowest turbulence intensity where the RMS speed error of the proposed MIMO IPC is the lowest while that of the baseline CPC with large enough optimum yaw misalignment angle (i.e., -15°) is the highest.

The maximum generator speed errors are compared in Fig. 4.10 because WT overspeeding is undesirable. While there is no statistically significant difference among the controllers, it can be seen at 18 m/s (5%) that misaligning the WT to a large degree can deteriorate the speed (and power) regulation and in most of the simulated conditions the proposed controller is the one least likely to overspeed the WT.

4.5.2 Structural loads

Blade loads

Both the baseline and proposed IPCs are designed to mitigate the blade OOP bending moments. Therefore, the OOP bending moments of the first blade are compared in Fig. 4.11. The proposed MIMO controller consistently yields the lowest blade OOP loads across all simulated mean wind velocities and turbulence intensities. In terms of the mean DEL, this improvement as compared with the baseline CPC without misalignment was found to be at least 31.54% at 18 m/s (A) and at most 42.03% at 20 m/s (C). Although the mean blade OOP loads of the baseline IPC are always lower than that of the baseline CPC, the improvements are not statistically significant except at the lowest mean wind velocity of 14 m/s (C) and lowest turbulence intensity of 18 m/s (5%), where the baseline IPC in average yields 8.3% and 28.97% lower blade OOP loads, respectively. Further, the blade OOP loads of the baseline IPC has higher variation at higher turbulence intensity of 18 m/s (A), which indicates that volatile wind variations can deteriorate the performance of the baseline IPC. A similar trend can be observed when yaw misalignment angle is introduced, where despite yielding lower mean blade OOP loads than those of without misalignment, the improvements are less significant as turbulence intensity increases. Even at low turbulence intensity, the intentional yaw misalignment does not outperform the baseline IPC.

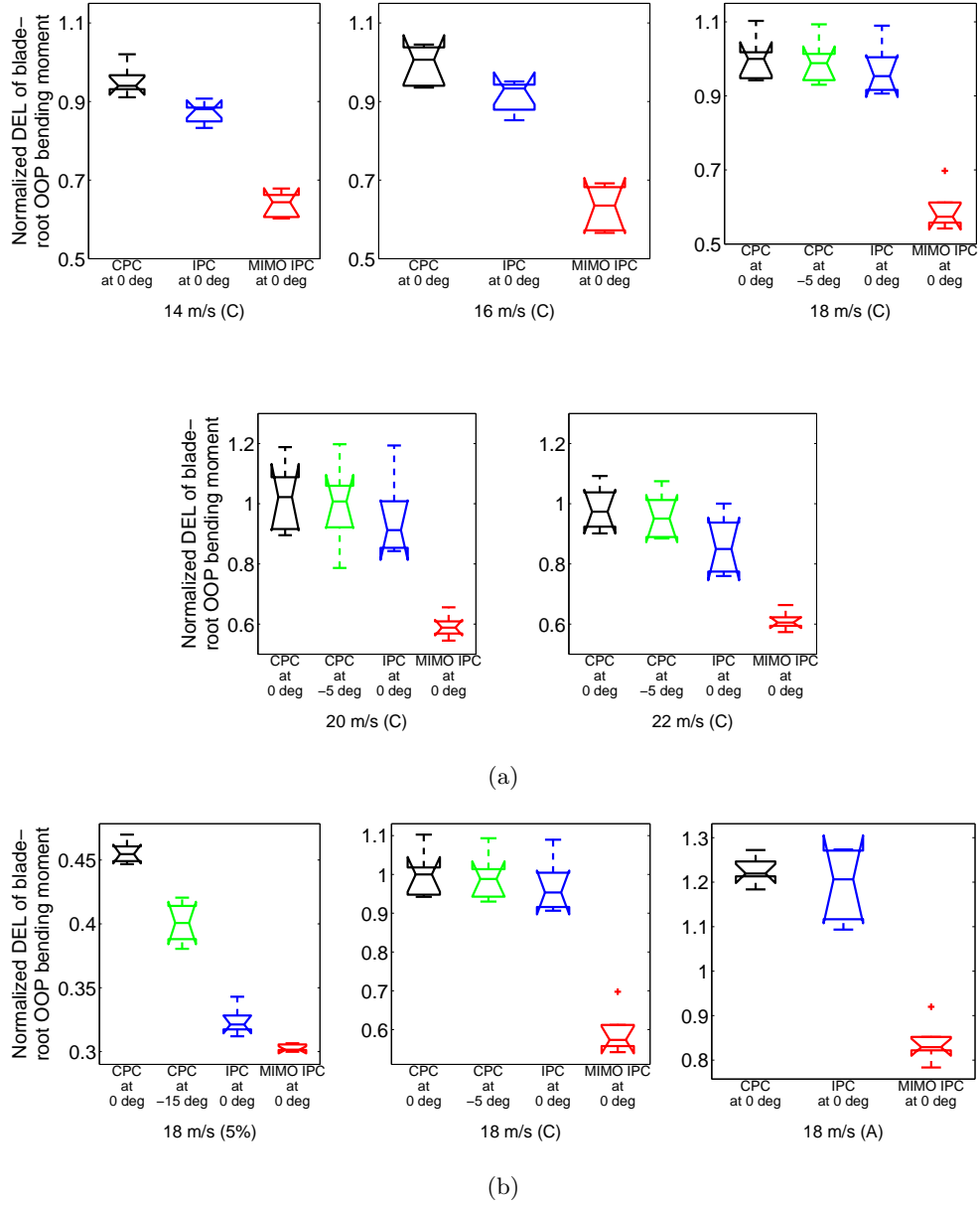


Figure 4.11: Comparison of the DEL of blade-root OOP bending moment of blade 1 at various (a) mean wind velocities and (b) turbulence intensities.

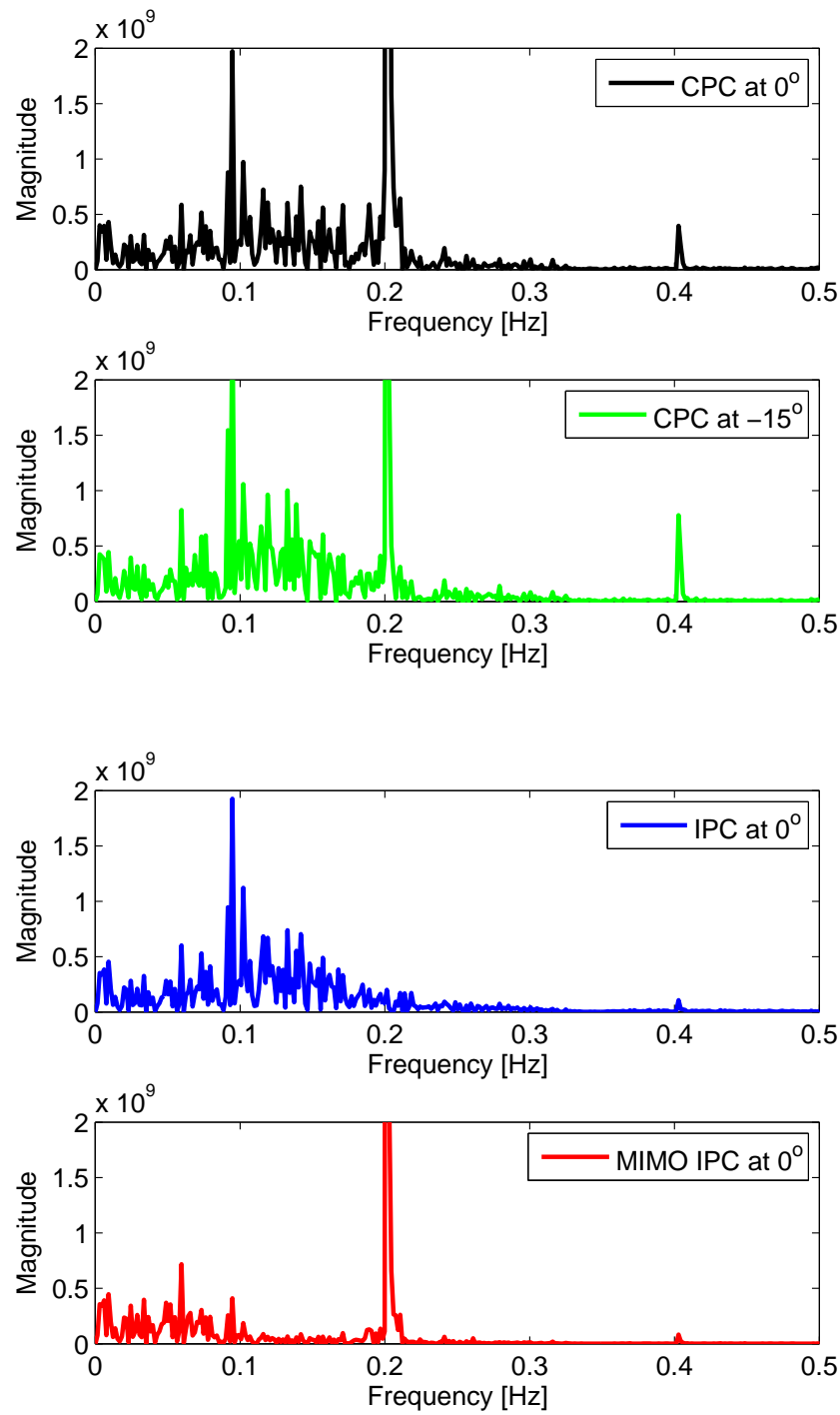


Figure 4.12: Power spectral density (in Nm) of a blade OOP load at 18 m/s (5%).

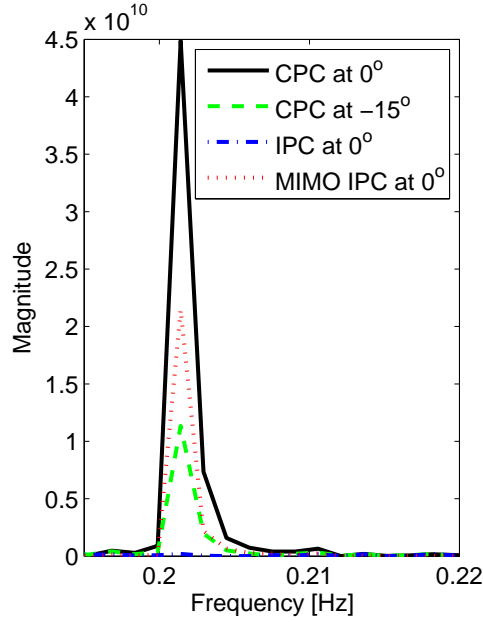


Figure 4.13: Power spectral density (in Nm) of a blade OOP load at 18 m/s (5%) around the WT rotational speed.

The contribution of each control scheme on the blade OOP load mitigation can further be appreciated by looking into the power spectral density of the blade OOP load. As a representation, the resulting blade OOP load of a turbulence sample of 18 m/s (5%) are shown in Figs. 4.12 and 4.13. As expected, the baseline IPC removes the blade OOP load component at the WT rotational speed of 0.2 Hz (i.e., at about 12 RPM). The baseline CPC with intentional yaw misalignment and proposed MIMO IPC also reduce the load component at this frequency, with the former performing better than the latter. Nevertheless, the major contribution of the proposed controller to blade load mitigation is in the broad attenuation of frequency components starting from about 0.1 Hz. These frequency components are attributed to turbulence (i.e., variation in wind velocity and inflow angle), which are not properly accommodated by the baseline controllers but satisfactorily attenuated by the proposed controller, as illustrated earlier in Fig. 4.6.

The blade IP loads are not affected by the vertical wind shear. Nonetheless, to ensure that the blade OOP load mitigation of the proposed IPC does not sacrifice another component of the blade loads, the IP loads of the first blade from all controllers are compared in Fig. 4.14. It shows that for the baseline CPC without misalignment, the mean blade IP loads increase as the mean wind velocity and turbulence intensity increase. Other controllers do not follow the trend while

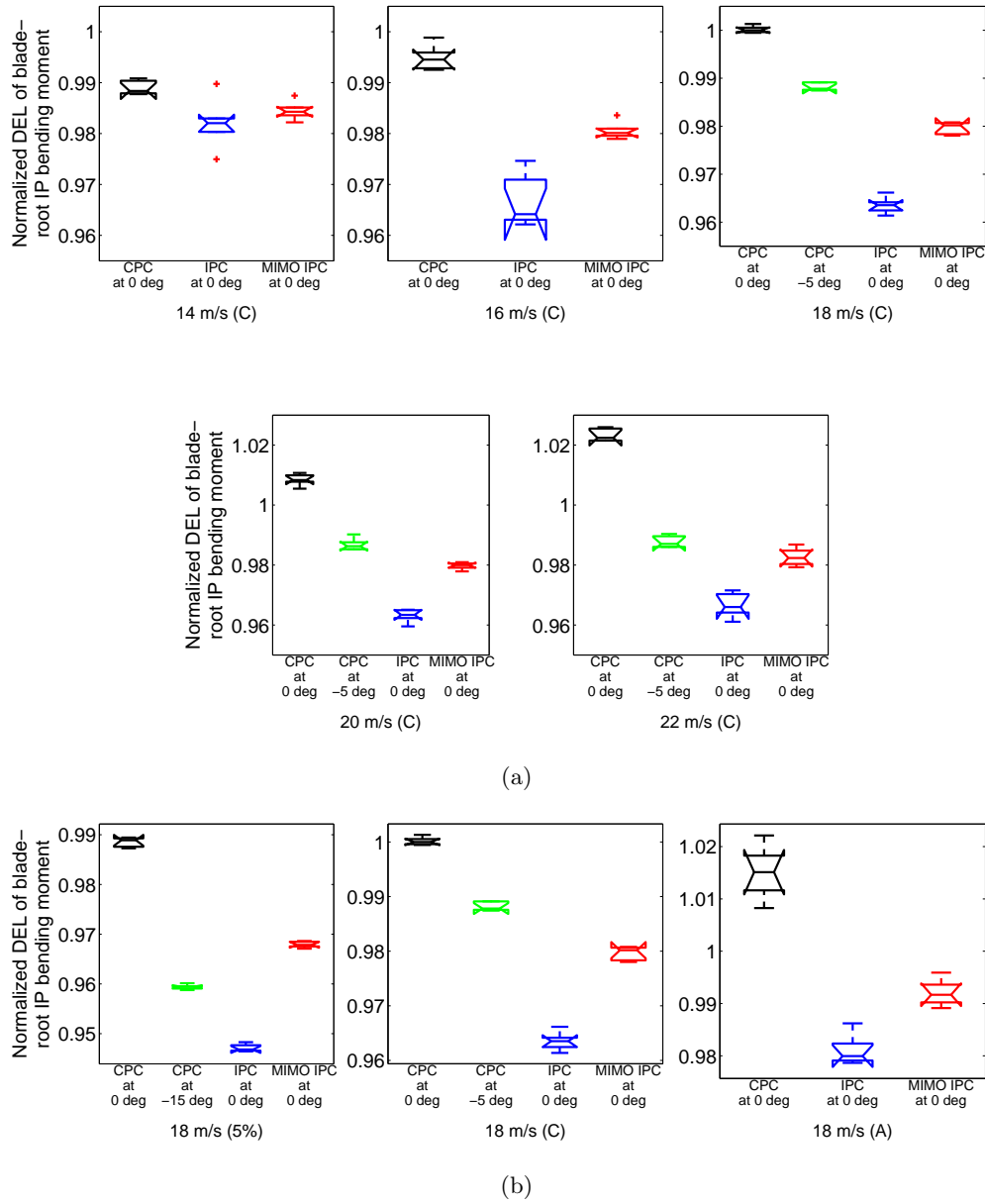


Figure 4.14: Comparison of the DEL of blade-root IP bending moment of blade 1 at various (a) mean wind velocities and (b) turbulence intensities.

resulting in lower blade IP loads. The baseline IPC consistently yields the lowest blade IP loads across the simulated mean wind velocities and turbulence intensities, with the best mitigation of 5.37% compared with the baseline CPC at 22 m/s (C). The power spectral density of this load due to all controllers are identical and hence not shown.

Based on the significant improvements in the blade OOP loads and comparable performances in the blade IP loads with respect to the baseline IPC, it can be concluded that the proposed MIMO IPC yields superior performance in mitigating the overall blade loads.

Tower loads

Although the tower dynamics were not considered during the design of the controllers, the WT tower is an integral and important component affecting the overall WT performance and effective lifetime. Further, comparing the resulting tower load can give more insights into the comparative performance of each controller.

The FA bending moments at the tower-base of all controllers are compared in Fig. 4.15. For all controllers, the mean tower FA loads increase as the mean wind velocity and turbulence intensity increase. Nonetheless, the proposed controller consistently yields the lowest tower FA loads across all simulated mean wind velocities and turbulence intensities. The improvement, as compared with the baseline CPC without misalignment, in terms of the mean DEL, is at least 35.32% at 22 m/s (C). It further improves up to 44.97% as the mean wind velocity decreases to 14 m/s (C). The baseline IPC and CPC with misalignment always yield higher mean tower FA loads than that of the baseline CPC without misalignment even though the differences are not statistically significant.

The power spectral density of the tower FA load of a turbulence sample of 18 m/s (C) are shown in Fig. 4.16. Consistent with the findings in Fig. 4.15, the spectral density of the three control schemes are identical with prominent peaks at around 0.15 Hz and 0.324 Hz, attributed to turbulence and the tower FA mode [17], respectively, with the baseline IPC yielding higher peaks at the latter mode. Comparing Fig. 4.15 with Fig. 4.6 and observing that the peaks of the tower load get attenuated as they are within the blade load mitigation region of the MIMO IPC suggest a strong disturbance rejection property of the proposed controller.

The SS bending moments at the tower-base of all controllers are compared in Fig. 4.17. For all controllers, the mean tower SS loads increase as the mean wind velocity and turbulence intensity

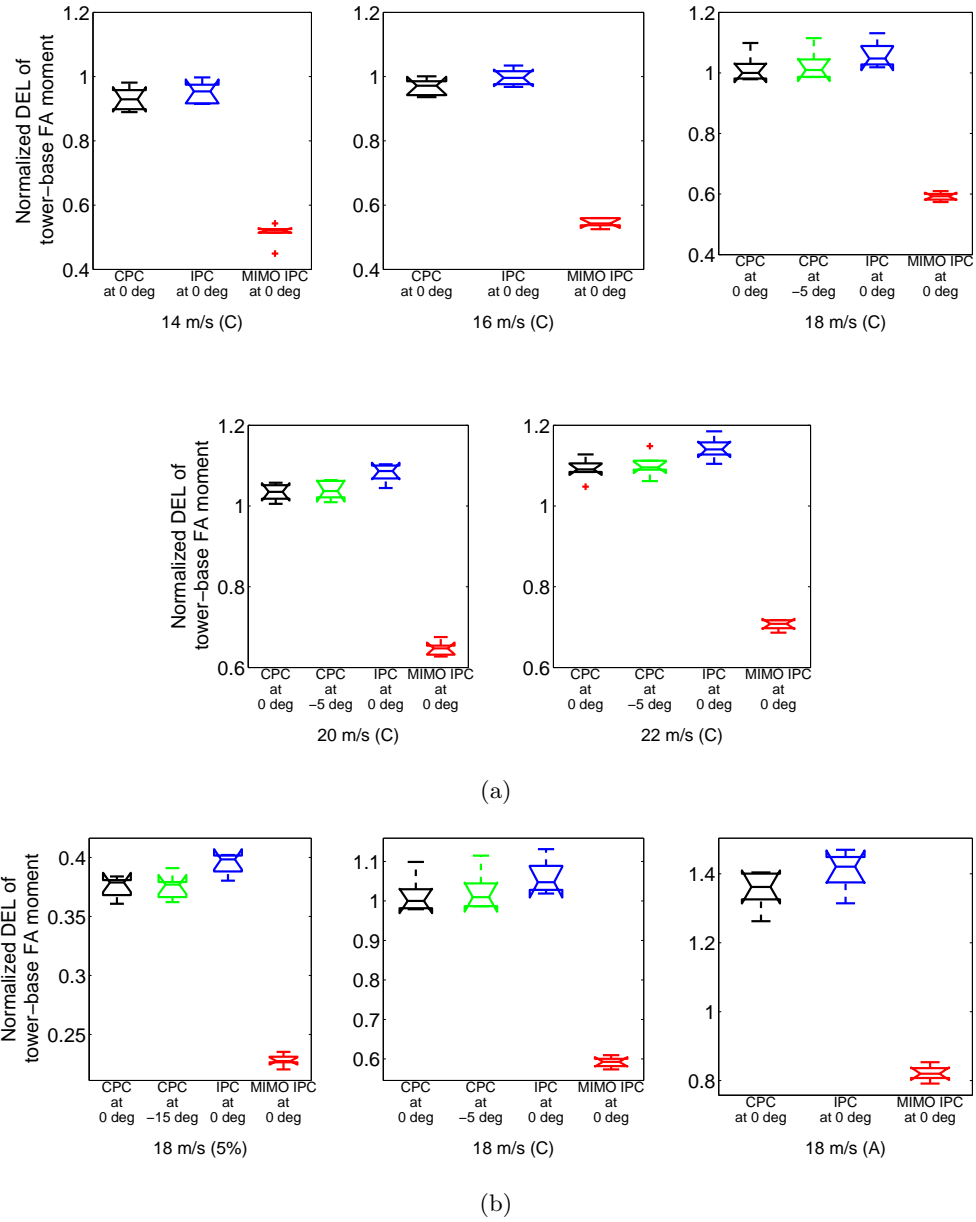


Figure 4.15: Comparison of the DEL of tower-base FA at various (a) mean wind velocities and (b) turbulence intensities.

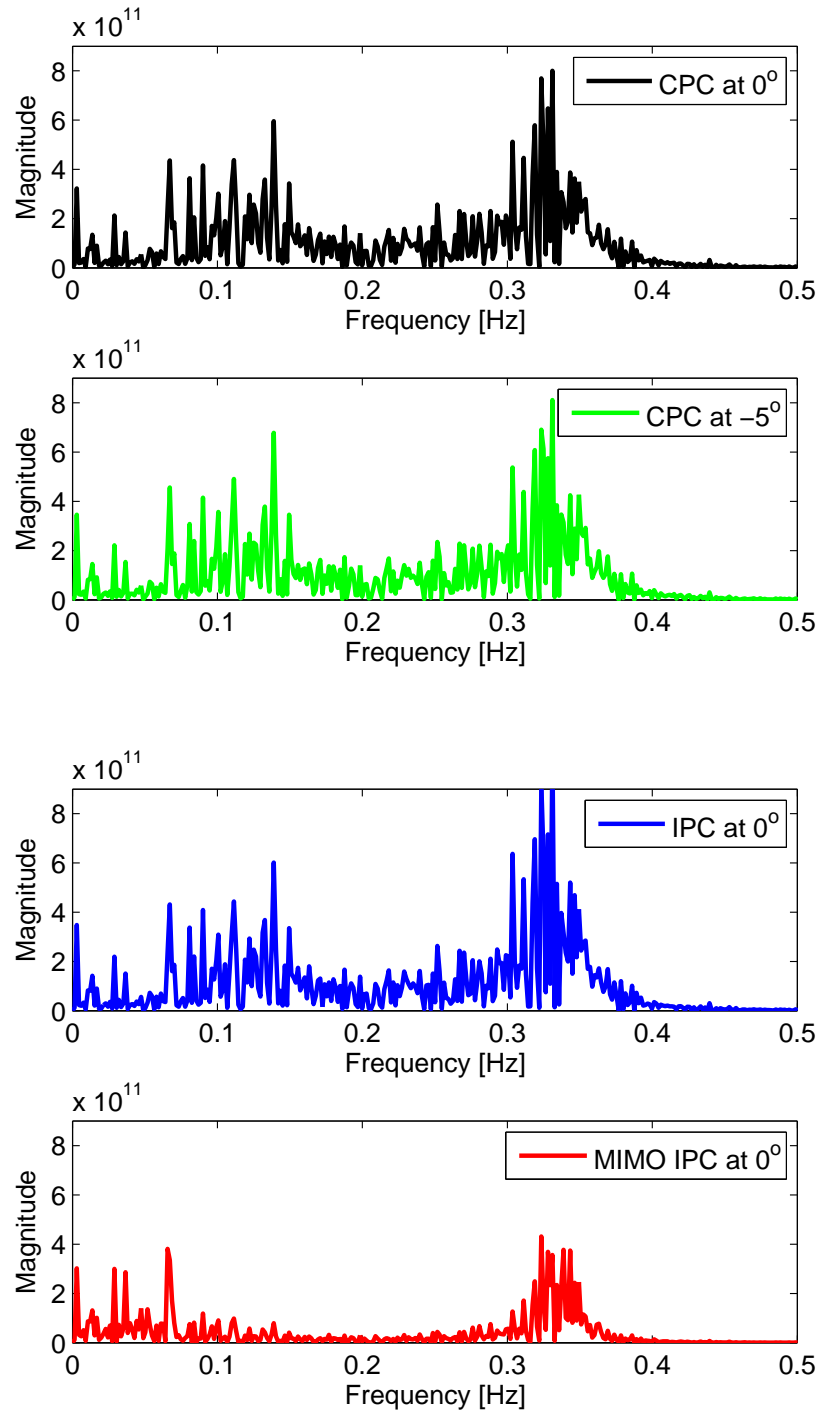


Figure 4.16: Power spectral density (in Nm) of a tower-base FA load at 18 m/s (C).

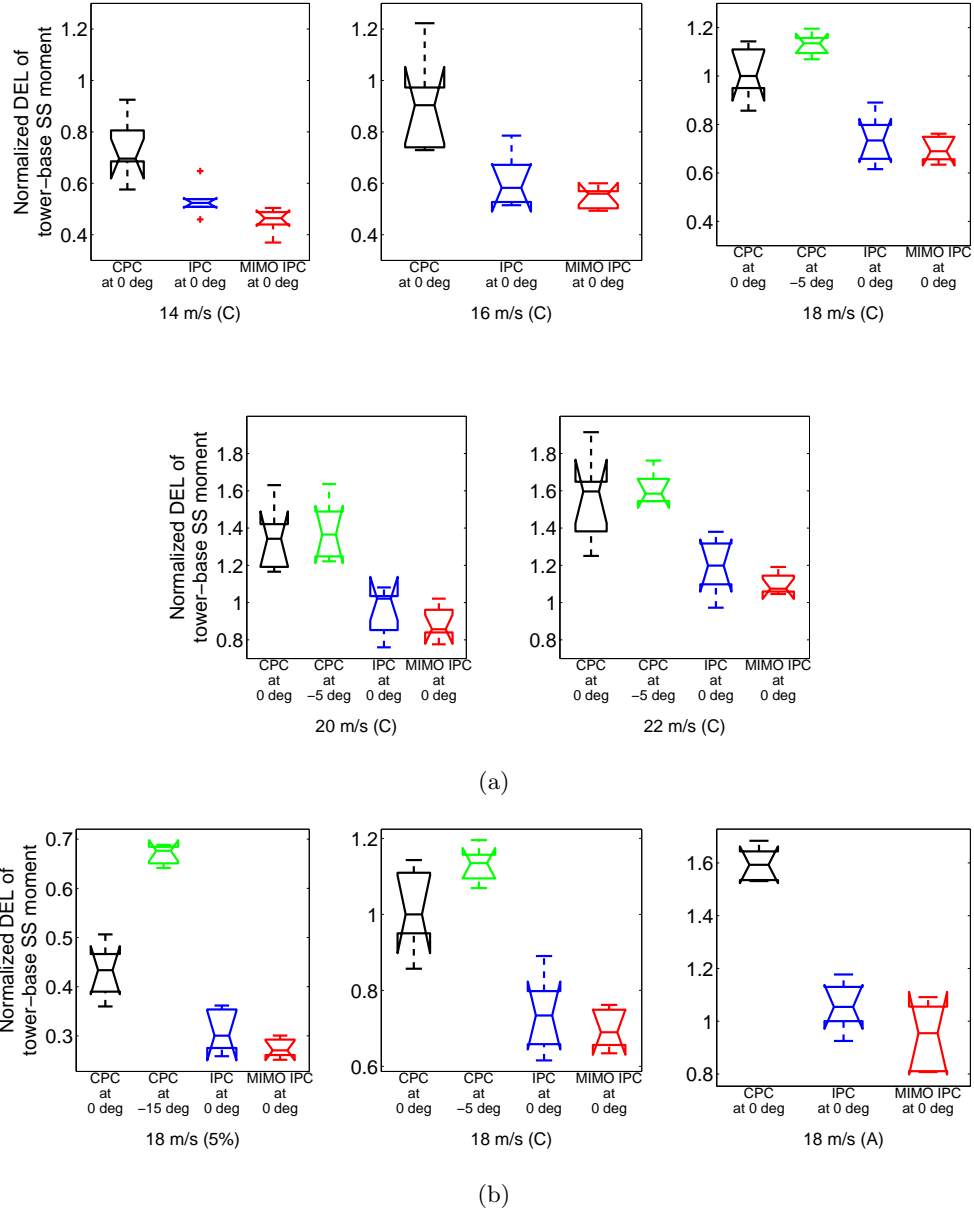


Figure 4.17: Comparison of the DEL of tower-base SS at various (a) mean wind velocities and (b) turbulence intensities.

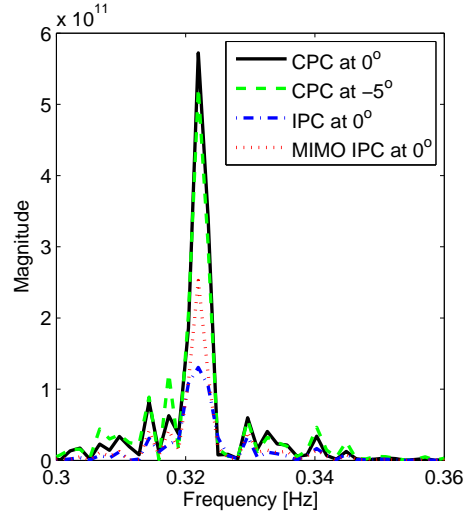


Figure 4.18: Power spectral density (in Nm) of a tower-base SS load at 20 m/s (C).

increase. Both baseline and proposed IPCs result in lower tower SS loads with no significant difference between the two while the intentional yaw misalignment increases this load. Consistent with the findings, the power spectral density of the tower SS load of a turbulence sample of 20 m/s (C) around the tower SS mode of 0.312 Hz [17] is shown in Fig. 4.18.

4.6 Chapter Conclusions

So far, the pitch controller designs in research and industry have not considered any yaw misalignment. However, it has been have shown that yaw misalignment can yield significant reduction in blade moment variations caused by wind shear. This chapter proposes an LQR-based MIMO IPC design considering a WT model linearized at a yawed inflow condition. The proposed IPC is decoupled from the yaw controller; thus, allowing implementation of conventional yaw controllers that aim to align the WT with the wind. Performance of the controller is compared with that of the baseline CPC and IPC through simulations under various turbulent wind conditions. The results show that compared with the baseline CPC, the proposed controller is shown to contribute at least a 31.54% reduction in the blade out-of-plane fatigue load, a 35.32% reduction in the tower fore-aft fatigue load, and a 29.80% reduction in the tower side-to-side fatigue load. Therefore, the proposed controller design can bring benefits in increasing the reliability of the overall WT components.

Chapter 5

Torsional Models of Wind Turbine Drivetrain

5.1 Introduction

It has been shown so far throughout this thesis that aeroelastic tools, such as FAST, are capable to model and simulate the dynamics of WTs in response to different wind fields and controller designs. While high-order models are used to represent the dynamics of the WT blades and tower, the drivetrain model of FAST, and of other aeroelastic tools [61,62], is a simplified two-DOF model shown in Fig. 3.1, which results in restricted detail in describing various configurations and complex dynamic behaviors of different drivetrain designs. Although dynamic models for WT drivetrains have been developed with various levels of fidelity [63–72], they do not provide direct insights on the dynamic interactions between the drivetrain and other components of the WT. Recent studies in [71, 72] take a decoupled approach in which the global WT response was first simulated using an aeroelastic tool. Afterwards, the resulting loads and motion trajectories of the WT rotor as well as the nacelle were used as inputs to a high-fidelity model of the drivetrain to simulate its internal dynamic behavior. In such a way, the decoupled approach fails to capture the influence of the drivetrain dynamics onto the overall WT response.

Three torsional models of WT drivetrain are discussed in this chapter, one of which is the most basic two-mass model while the other two are developed using the Simscape/SimDriveline [73] with higher-fidelity to better capture the internal dynamics of the gearbox. All models are based on lumped parameter approach that models a mechanical system as concentrated masses, springs, dampers, and point forces or torques. Each mass is characterized by finite number of degrees of freedom. Only the torsional degree of freedom is considered in this chapter. Thus, each shaft is modeled as an ideal massless torsional spring and each gear is modeled as an inertial body. In this

chapter, the model with the highest fidelity is integrated with FAST in the Simulink environment to investigate the dynamic response of a WT drivetrain under aerodynamic and electrical excitations.

5.2 Model Overview

The WT modeled in this part of the thesis is based on the 750-kW GRC WT summarized in Table 2.2. The WT was originally equipped with two fixed-speed (i.e., type 1) generators. To model the variable-speed operation of region 2 operation for maximum energy capture, the generator is modeled using a DFIG (i.e., type 3 generator). The induction generator model is based on a commercial WT of the same rating available in the market. The models of the generator and converters were built using the Simscape/SimPowerSystems based on the properties detailed in Table 5.1 following the models in [74]. An average model of the AC/DC/AC converter can be used to analyse the electromechanical interaction because the mechanical components of the drivetrain have much slower dynamics than the power electronics. In an average model, the power electronics components were replaced by controlled current sources [75].

Table 5.1: Parameters of the 750-kW DFIG

Generator	
Line-line voltage (RMS)	690 V
Frequency, number of pole pairs	60 Hz, 2
Stator resistance, leakage inductance (pu)	0.016, 0.06
Rotor resistance, leakage inductance, both referred to stator (pu)	0.016, 0.06
Magnetizing inductance (pu)	2.56
Inertia constant (s)	2
Converter	
Converter maximum power (pu)	0.5
Grid side coupling inductance, reactance (pu)	0.15, 0.0015
Nominal DC bus voltage	1200 V
DC bus capacitor	0.1 F

For wind velocities below 12.5 m/s, which is the rated wind velocity of the GRC WT), the output power of the generator is controlled to track the maximum power coefficient ($C_{P_{\max}}$) while maintaining constant pitch angle at its optimum aerodynamic efficiency of -3.5° .

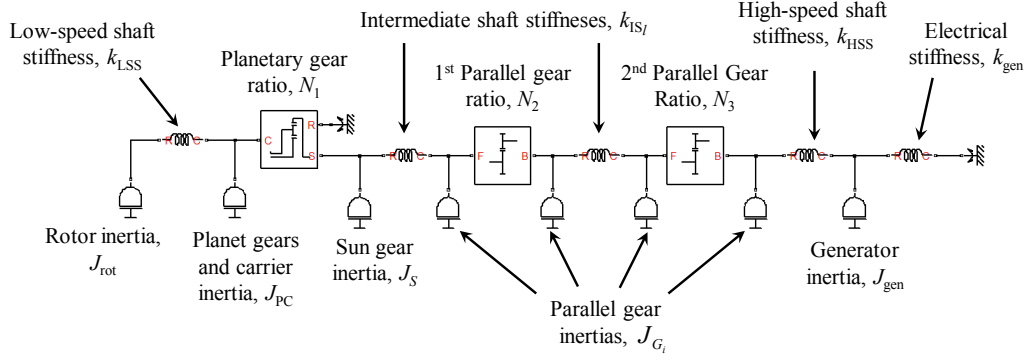


Figure 5.1: Five-mass model of WT drivetrain built in Simscape/SimDriveline.

Table 5.2: Parameters of GRC Drivetrain

Stiffnesses [Nm/rad]		Inertias [kg m ²]	
k_{LSS}	3.69×10^7	J_{rot}	998138.4
$k_{IS_1} = k_1$	2.45×10^7	J_{PC}	116.72
$k_{IS_2} = k_2$	2.70×10^8	J_P	3.32
k_{HSS}	2.08×10^6	J_C	106.76
$k_{planet-ring}$	5.86×10^7	J_S	1.02
$k_{planet-sun}$	5.86×10^7	J_{G_1}	31.72
k_{P_1}	5.23×10^7	J_{G_2}	0.4
k_{P_2}	1.72×10^7	J_{G_3}	3.42
Gear ratios		J_{G_4}	0.08
		J_{gen}	39
N_1	5.714		
N_2	3.565		
N_3	4		

5.3 Five-mass Model of Drivetrain

Figure 2.13(b) shows the building blocks of the modular drivetrain commonly used in operating WTs [63]. In GRC WT, the multistage gearbox consists of a planetary (epicyclic) gear stage and two parallel gear stages, with two intermediate shafts.

Figure 5.1 shows the five-mass model of GRC WT drivetrain, developed in the Simscape/SimDriveline environment. The five inertial bodies (i.e. the masses) represent the rotor, gears, and generator. This model considers rigid gearbox. In other words, the gearbox is assumed to have static transmission across the gear sets, defined by each gear ratio. The mechanical parameters are listed in Table 5.2.

A fixed-speed induction generator has an electrical torsional stiffness k_{gen} between the air gap

magnetic field and the generator rotor. This stiffness behaves as a spring to the inertial reference frame of the drivetrain, which provides a restoring torque to the rest of the drivetrain. Such stiffness arises because of tight allowable speed variation in this type of generator. Effects of this stiffness are prominent in the transient response of the generator (e.g., during startup). For a variable-speed generator, this restoring effect does not exist, and the drivetrain model shown in Fig. 5.1 will have a free boundary condition on the other side of the generator.

5.4 Two-mass Model of Drivetrain

Figure 3.1 has shown the configuration of the two-mass model commonly used to model the dynamics of the drivetrains in WT aeroelastic tools, such as FAST [12]. Inputs into the model are the five parameters: J_{rot} , k_{eff} , c_{eff} , N , and $\frac{J_{\text{eff}}}{N^2}$. The generator electrical torsional stiffness is generally not required in FAST because this stiffness is inherent to the generator model used for the analysis. Parameters of the two-mass model can be derived from the five-mass model as follows

$$J_{\text{eff}} = J_{\text{PC}} + N_1^2 (J_S + J_{G_1} + N_2^2 (J_{G_2} + J_{G_3} + N_3^2 (J_{G_4} + J_{\text{gen}}))) \quad (5.1)$$

$$\frac{1}{k_{\text{eff}}} = \frac{1}{k_{\text{LSS}}} + \frac{1}{N_1^2 k_1} + \frac{1}{(N_1 N_2)^2 k_2} + \frac{1}{(N_1 N_2 N_3)^2 k_{\text{HSS}}} \quad (5.2)$$

$$N = N_1 N_2 N_3 \quad (5.3)$$

The effective drivetrain torsional damping, c_{eff} , can be determined experimentally through several braking events [63].

The two-mass model cannot represent the different possible drivetrain configurations because the rest of the drivetrain is represented by one spring and one mass. As presented later in this chapter, this model has limitations in providing insights on possible resonant excitations of the drivetrain as well as in analyzing the loads experienced by each of the drivetrain components.

5.5 Pure Torsional Model of Gearbox with Constant Meshing Stiffness

In the previously described drivetrain models, the meshing gear is modeled as an ideal static gain for mechanical power (i.e., torque and speed) transmission. In reality, the gear transmission error,

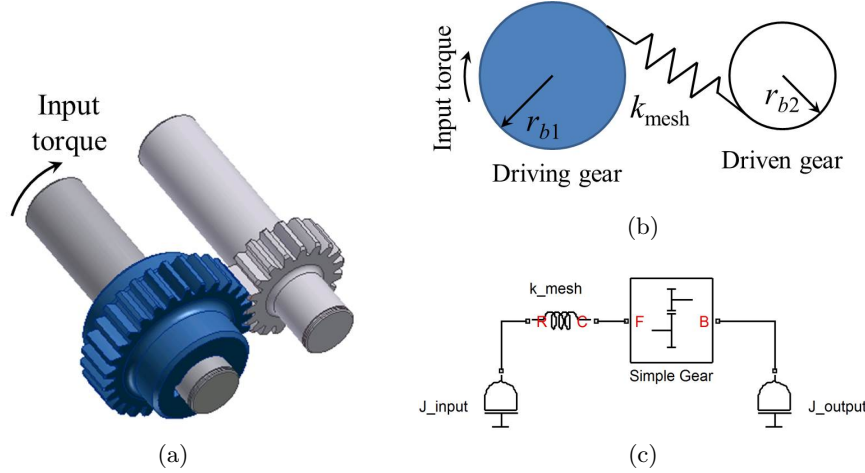


Figure 5.2: (a) Parallel gear stage, (b) dynamic model representation, and (c) model representation in Simscape/SimDriveline.

which is defined as the difference between the actual and ideal angular positions of the rotating gear, resulted mainly due to the gear elastic deformation, contributes to the dynamics of the pair meshing gear. This phenomenon contributes to the definition of gear meshing stiffness. This chapter introduces the application of a purely torsional model of WT drivetrain with constant gear meshing stiffness. This section described the model development and analysis on both planetary and parallel gear stages.

5.5.1 Parallel Gear Stage

Figure 5.2(a) shows a parallel gear set, which is a torque reducer, commonly employed in WT drivetrains. Figure 5.2(b) represents its flexible equivalent, in which the meshing stiffness acts on the line of action of the meshing gears. The constant meshing stiffness k_{mesh} , with respect to the input gear, can be represented as the function of geometric and material properties of the input gear [76]:

$$k_{\text{mesh}} = k_{\text{gear}} (r_{b1} \cos \gamma) \quad (5.4)$$

where r_{b1} is the base circle radius of the input gear and γ is the helical angle of the gears. The gear tooth stiffness k_{gear} can be determined according to international standards, such as DIN 3990 [77] and ISO 6336 [78].

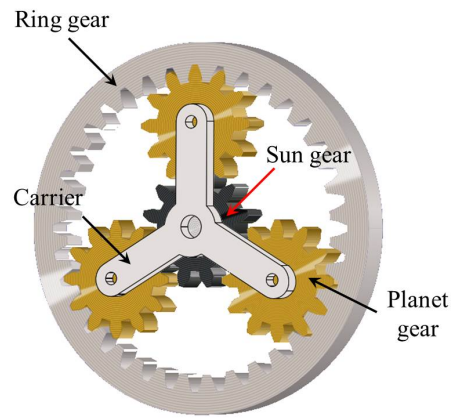
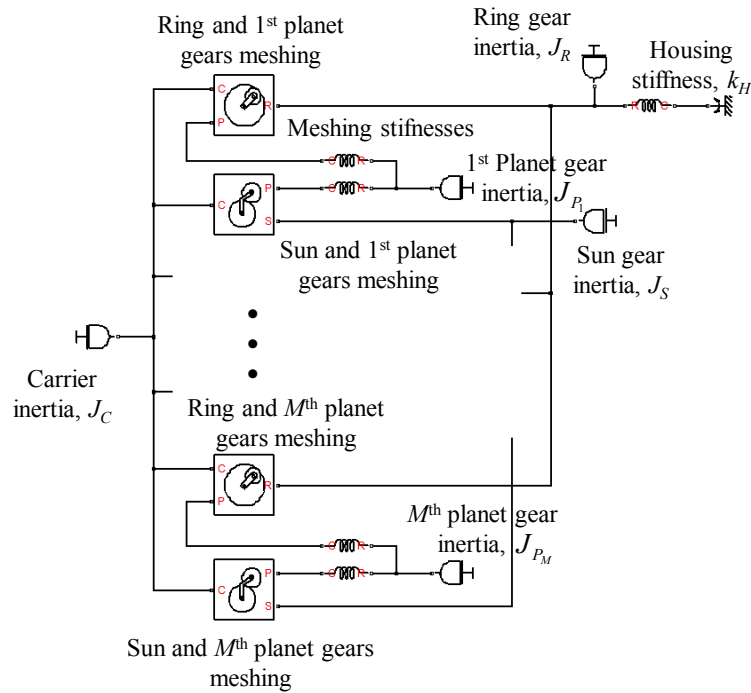


Figure 5.3: Planetary gear stage with 3 planet gears.

Figure 5.4: Torsional model of planetary gear stage with M planet gears.

5.5.2 Planetary Gear Stage

Figure 5.3 shows a planetary gear set with three planet gears, which is a similar configuration to the one installed in the GRC WT. The rotational input is from the carrier of the planetary gear stage, which provides rotational motion through the planet gears, and finally to the sun gear. The ring gear is modeled to have flexible coupling with the fixed gear housing. The flexibility between the meshing planet and ring gears and between the meshing planet and sun gears can be modeled similar to that of a parallel gear set shown in Fig. 5.2(b) based on Eq. (5.4). Figure 5.4 shows a schematic diagram of the torsional model of the planetary gear set built in the Simscape/SimDriveline environment. This model can be adapted for planetary gear sets with equispaced M planet gears.

5.6 Eigenfrequency Analysis and Validations

Eigenfrequencies of a system can be found either analytically or numerically. Equations of motion of a WT drivetrain are used to analytically compute the eigenfrequencies in [69, 79]. However, this approach becomes inconvenient as the order of the dynamic model increases. The developed drivetrain model in SimDriveline allows the usage of MATLAB/Simulink basic packages to numerically estimate the eigenfrequencies.

The resulting eigenfrequencies were validated at both component level (i.e., the gearbox) and integrated drivetrain level. The eigenfrequencies of planetary gear sets were validated against those published in [76], while those of the overall GRC drivetrain were validated against the results from field measurements.

5.6.1 Eigenfrequencies of Purely Torsional Gearbox Model

While some works have reported experimental measurements of gearbox eigenfrequencies [64, 80], it is difficult to justifiably replicate the results because the mechanical properties of those gearboxes are not publicly available. Thus, to validate the developed purely torsional gearbox, eigenfrequencies of the SimDriveline gear set models are compared with those reported in [76].

It is important to note that the gear parameters used in the component-level validation in this subsection is based on the ones originally used in [81], which are different from the ones implemented in the GRC drivetrain. Eigenfrequencies of this planetary gear set have been evaluated in other

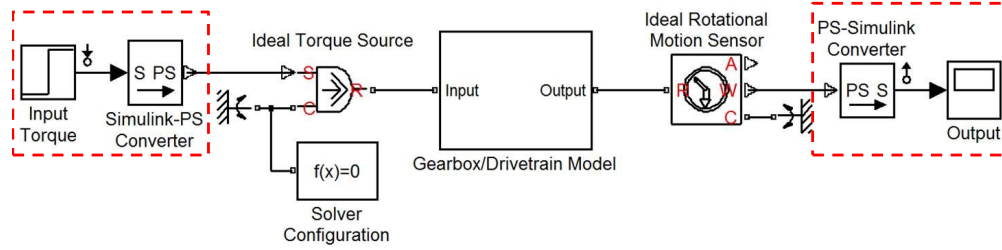


Figure 5.5: Input-output configuration on SimDriveline model for eigenfrequency analysis.

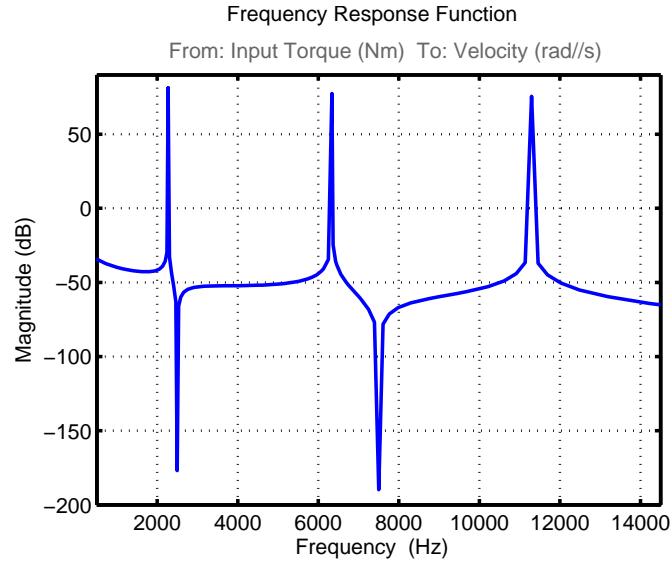


Figure 5.6: FRF of three-planet planetary gear stage for the gearbox presented in [75].

published works [76, 82–85]. Particularly in [76], the analysis was performed on the planetary gear sets with different numbers of planet gears.

Estimating the eigenfrequencies using the SimDriveline models was done by first defining the excitation input and the output to be monitored. For analysis and verification, the input for the gearbox model was the torque to the carrier, while the output was the angular velocity of the sun gear as illustrated in Fig. 5.5. Based on the input-output configuration, MATLAB/Simulink Control System Toolbox was used to compute the linear state-space representation of the model, frequency response function (FRF) of which has been used to indicate the eigenfrequencies. Figure 5.6 shows the FRF of the planetary gear set that has three planet gears, where the sharp peaks correspond to the response amplifications at the gearbox eigenfrequencies. The comparisons for different numbers of planet gears show good agreement with results presented in [76] and are summarized in Table 5.3.

Table 5.3: Comparisons with Eigenfrequencies Reported in [75]

Mode	SimDriveline Model	Peeters [75]	Difference
3 Planet Gears, $M = 3$			
1	2.273 kHz	2.217 kHz	2.53 %
2	6.340 kHz	6.159 kHz	2.94 %
3	11.296 kHz	11.205 kHz	0.81 %
4 Planet Gears, $M = 4$			
1	2.207 kHz	2.138 kHz	3.23 %
2	6.911 kHz	6.688 kHz	3.33 %
3	12.699 kHz	12.577 kHz	0.97 %
5 Planet Gears, $M = 5$			
1	2.153 kHz	2.059 kHz	4.57 %
2	7.403 kHz	7.105 kHz	4.19 %
3	13.980 kHz	13.810 kHz	1.23 %

5.6.2 Eigenfrequencies of Overall Drivetrain Model

Ultimately, all necessary component models, including the purely torsional gearbox model discussed earlier, were integrated and the parameters in Table 5.2 were set to build the overall GRC drivetrain model. Eigenfrequency analysis for the drivetrain was performed with the torque to the WT rotor as the input and the angular position of the generator as the output. The resulting eigenfrequencies are compared herein with the frequency components of several measured drivetrain transient responses [71]. The GRC WT was equipped with torque transducer to measure the operating drivetrain loads. Due to the limited sampling rate of 100 Hz, the measured response can only be used to validate the first drivetrain eigenfrequency.

The first two transient responses shown in Figs. 5.7 and 5.8 are attributed to the generator. Hence, the analysis on the overall drivetrain model included the electrical torsional stiffness. Table 5.4 summarizes the drivetrain eigenfrequencies both with and without the electrical torsional stiffness. Figure 5.7 shows the torque measured on the LSS (i.e., the rotor opposing torque) during a generator startup at $t = 57$ s. Before the generator is connected to the grid, the turbine is accelerated by the aerodynamic torque while there is no opposing torque from the generator. The dotted box highlights the transient response oscillating at the drivetrain eigenfrequencies, which is revealed to be around 0.78 Hz. Figure 5.8 shows another transient response when the drivetrain was upshifted to a higher-speed generator. It reveals an eigenfrequency of 0.68 Hz. These two frequency readings are very close to the one calculated from the SimDriveline model, which is 0.84 Hz. The

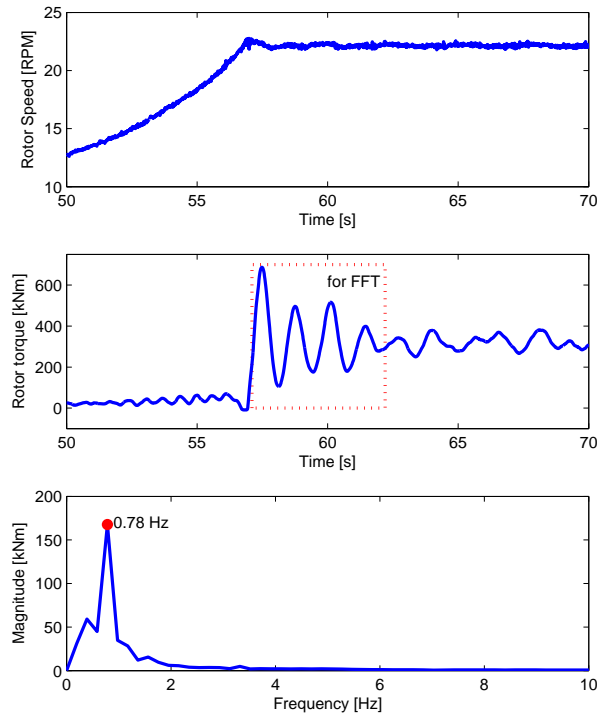


Figure 5.7: Transient rotor speed and torque from field measurements during generator startup.

Table 5.4: Eigenfrequencies of GRC Drivetrain with Torsional Gearbox Model

Mode	With Electrical Stiffness	Without Electrical Stiffness
1	0.84 Hz	0 Hz
2	4.62 Hz	1.83 Hz
3	154 Hz	
4	307 Hz	
5	353 Hz	
6	748 Hz	
7	1020 Hz	
8	1530 Hz	

second mode of 4.62 Hz was not apparent in the field measurements due to two possible reasons. Firstly, the energy stored in the second torsional mode is much smaller than that stored in the first one. Secondly, the second mode is attributed to the HSS. As discussed in the following section, excitations from the HSS get attenuated at the LSS side; thus, it may not appear as a dominant component in a measurement that contains noise. The experimental setup did not implement any torque measurements at the HSS.

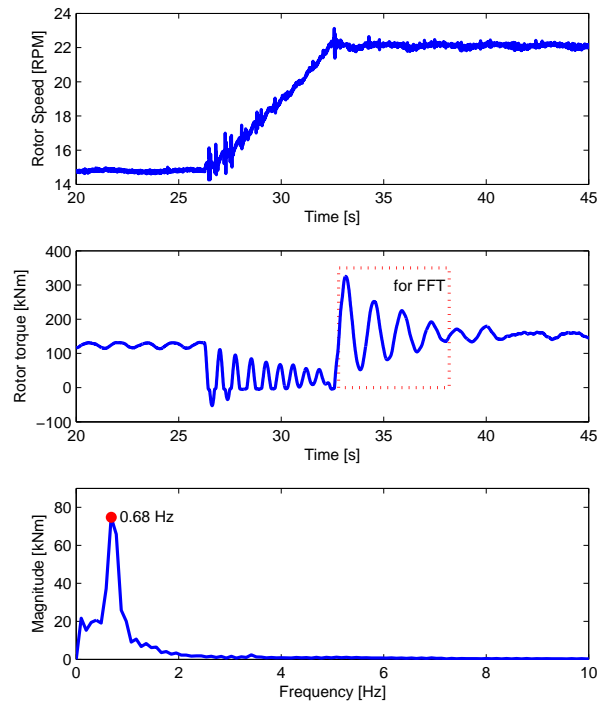


Figure 5.8: Transient rotor speed and torque from field measurements during generator upshift.

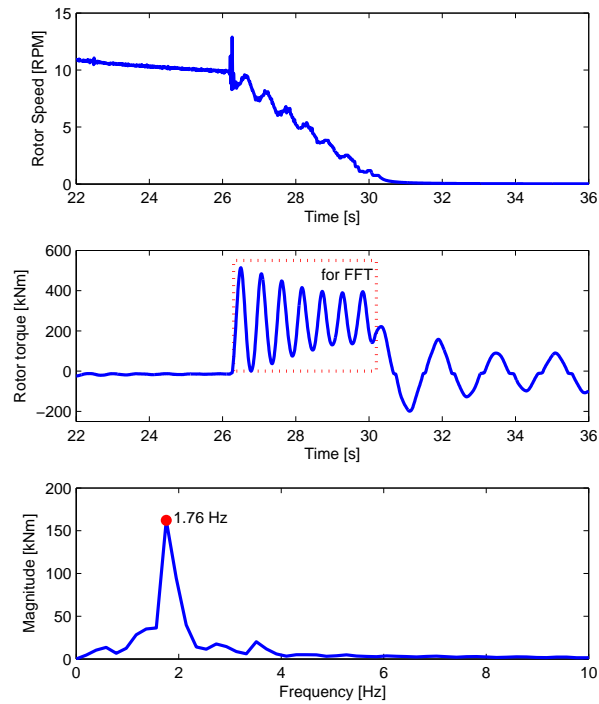


Figure 5.9: Transient rotor speed and torque from field measurements during braking event.

Figure 5.9 shows a transient response in an event of drivetrain braking, during the generator had already been disconnected from the grid. Thus, there is neither opposing torque from the generator and nor influence from the electrical torsional stiffness. In this event, a braking torque was applied mechanically at $t = 26$ s through the disc brake to put the WT into a complete stop after the WT was being decelerated by the blade tip brakes. The frequency decomposition of the transient rotor opposing torque reveals a frequency of 1.76 Hz, which is close to an eigenfrequency of 1.83 Hz predicted from the SimDriveline model. These results illustrate the validity of the SimDriveline model to predict the eigenfrequencies of both an independent gearbox and integrated WT drivetrain.

If the overall drivetrain is simplified to a two-mass model, the only nonzero eigenfrequency can be calculated using the parameters of Eqs. (5.1) - (5.3) as:

$$f_n = \frac{1}{2\pi} \sqrt{k_{\text{eff}} \left(\frac{1}{J_{\text{rot}}} + \frac{1}{J_{\text{eff}}} \right)} \quad (5.5)$$

The resulting eigenfrequency using the two-mass model for the GRC drivetrain is 2.32 Hz, which is quite different from the first nonzero drivetrain eigenfrequency of 1.83 Hz predicted earlier. This discrepancy can create a significant difference in predicting the loads experienced by the drivetrain.

5.7 Model Integration with FAST

Figure 5.10 illustrates the proposed strategy to integrate the described drivetrain models into the inherent two-mass model of FAST. For simplicity, the flexible modes of the other WT components modeled inside FAST, such as those of the blades and tower, are not depicted in the schematic diagram in Fig. 5.10.

The inherent two-mass drivetrain model of FAST is reduced to a single-mass model consisting of solely the rotor and the rigid shaft, as shown in the bottom part of Fig. 5.10. This is done by deactivating the flexibility of the drivetrain simulating rigid transmission and setting the gear ratio and the generator inertia to unity and zero, respectively. The rotor equation of motion can be expressed as

$$J_{\text{rot}} \alpha_{\text{rot}} = Q_{\text{aero}} - Q_{\text{opp}} \quad (5.6)$$

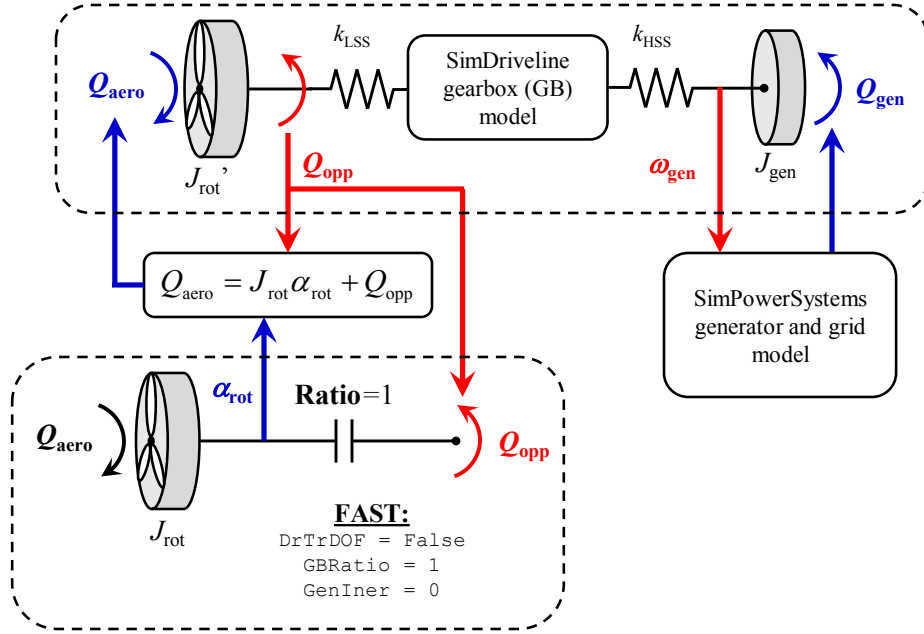


Figure 5.10: Integration of the SimDriveline drivetrain model with FAST.

FAST internally calculates the input aerodynamic torque Q_{aero} from the defined wind profile, but does not provide this torque as an output. However, as the rotor acceleration α_{rot} is an available FAST output, the aerodynamic torque can be reconstructed using Eq. (5.6) to be one of the inputs to the drivetrain model in SimDriveline. In this process, the rotor inertia is assumed constant and replicated inside the SimDriveline drivetrain model. The rotor inertia body is connected to the rest of the drivetrain model through the flexible LSS, the purely torsional gearbox model with constant gear meshing stiffness, the flexible HSS, and the generator inertia. Another end of the drivetrain model is connected to the DFIG model, built using the Simscape/SimPowerSystems, which takes rotational speed as input and provides the electromagnetic torque as another input to the drivetrain model.

The rotor opposing torque Q_{opp} is required as an input to the FAST drivetrain model as well as to calculate the aerodynamic torque in Eq. (5.6). In SimDriveline, this rotor-opposing torque can be retrieved by utilizing the torque sensor element behind the built rotor body. In general, torque, velocity, and angular-position sensor elements can be placed flexibly within the Simscape drivetrain model to monitor the response of the drivetrain under various load conditions.

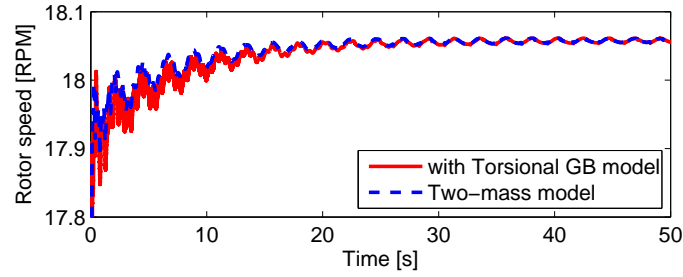


Figure 5.11: Rotor speed response at wind velocity of 7.25 m/s.

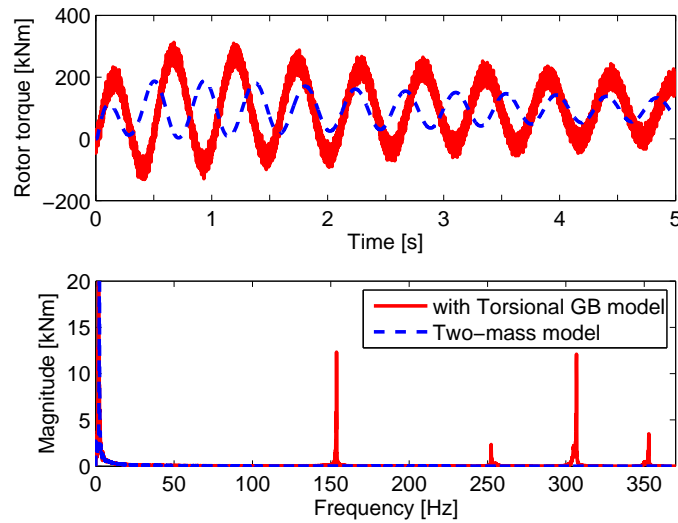


Figure 5.12: Transient response comparison of the rotor torque.

5.8 Simulation Results

Simulations in MATLAB/Simulink environment were performed to illustrate the effectiveness of the integrated torsional model of the gearbox (GB) model under different transient load cases. In the simulations, all available WT flexible modes in FAST, including that of the blades, tower, and drivetrain, were activated. Zero damping is defined within the drivetrain model to highlight the transient response of the drivetrain. Aerodynamic damping computed within FAST was the only source of damping that stabilizes the overall drivetrain response. The results are compared with those of an undamped two-mass model of the drivetrain inherent in FAST.

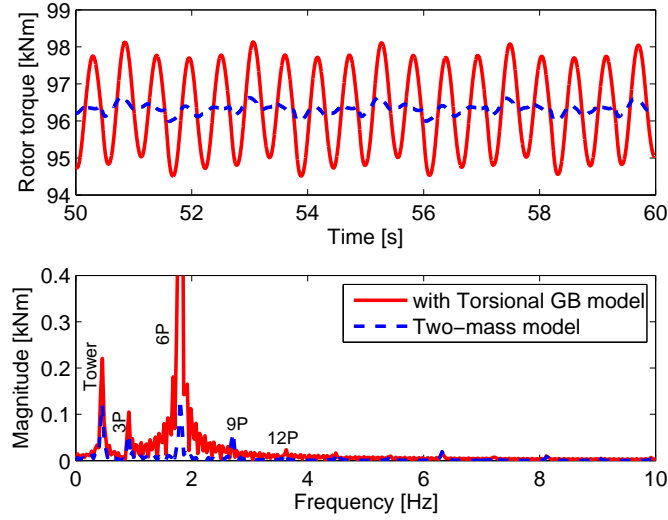


Figure 5.13: Steady-state response comparison of the rotor torque.

5.8.1 Transient Response due to Wind Excitation

The simulation was performed under a constant wind velocity of 7.25 m/s (i.e., below the rated wind velocity), and the WT rotor speed was initialized to be 17.9 RPM. The start of simulation effectively imparts a large step input to the system that can excite all of the drivetrain modes, especially during the transient period.

Figure 5.11 shows the WT rotor speed using the integrated drivetrain model as well as the inherent FAST two-mass model. The rotor speed steadily increases to reach the optimal TSR. Both models are in good agreement in the speed response of the GRC WT. Figure 5.12 is the transient response comparison of the rotor torque of the two models. It reveals the excitation of the high-eigenfrequency components coming from the high-fidelity drivetrain/gearbox model.

Figure 5.13 highlights the distinction between the two models in predicting the steady-state load response of the drivetrain. It also shows that the integrated model is able to capture dynamic coupling from other parts of the WT structures. The frequency of 0.4 Hz comes from the tower FA mode, whereas the frequency of 0.9 Hz and its harmonics come from the blade-pass frequency. The blade-pass frequency excitation occurs due to the aerodynamic interaction each time a blade-passes in front of the tower (i.e., the tower shadow effect). The i^{th} harmonic of blade-pass frequency is

dependent on the rotor rotational frequency f_{rot} .

$$f_{b,i} = imf_{\text{rot}}, \quad i = 1, 2, 3, \dots \quad (5.7)$$

where m is the number of blades (i.e., $m = 3$ for the GRC WT). The nominal of the blade-pass frequency excitation is often represented as 3P, referring that it occurs 3 times within a full rotation of the WT rotor .

The response of the drivetrain model with the purely torsional gearbox is particularly high at two times the blade-pass frequency (i.e., 6P) of 1.8 Hz because it is very close to the estimated first eigenfrequency of 1.83 Hz. Thus, it predicts amplification of load caused by resonance at the wind velocity of 7.25 m/s. On the other hand, the two-mass drivetrain model estimates an eigenfrequency of 2.32 Hz, which is at some distance from the harmonics of the blade-pass frequency, and hence predicts no resonance.

5.8.2 Transient Response Resulting From Grid Excitation

Another transient load can arise due to excitations from the grid events. One example of grid excitation was simulated to predict the loads on the gearbox. A drop in the grid voltage for 0.15 second, from 100% to 90% and back to 100% of the nominal RMS voltage, was simulated after the WT had reached steady-state.

As shown in Fig. 5.15, this voltage drop results in harmonic torque excitations to the drivetrain with frequencies of 50.78 Hz and 56.15 Hz. These frequencies are inherent to the generator characteristic. It is important to note that the frequency component of this torque excitation may cause resonances if the frequency matches any of the drivetrain eigenfrequencies. These resonances cannot be predicted using the standard two-mass model because the two-mass model can predict only the lowest eigenfrequency of the drivetrain.

Figure 5.15 illustrates how this load gets transmitted to each stage of the multistage gearbox. The torque through each shaft, except the LSS, is shown in both time and frequency domains. The HSS experiences the largest proportion of high-frequency loads caused by grid excitations compared to other shafts. Therefore, this shaft and the gear set directly connected to it are most prone to failures from fatigue in the event of grid disturbances. Sudden increases in the generator

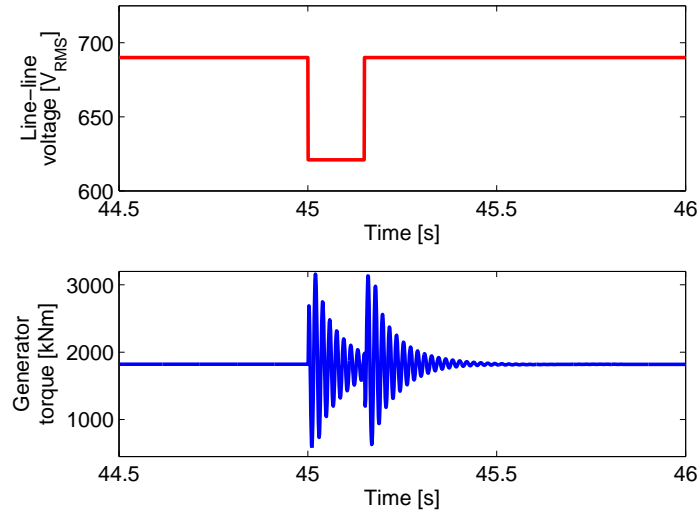


Figure 5.14: Generator torque excitations resulting from a voltage drop on the grid.

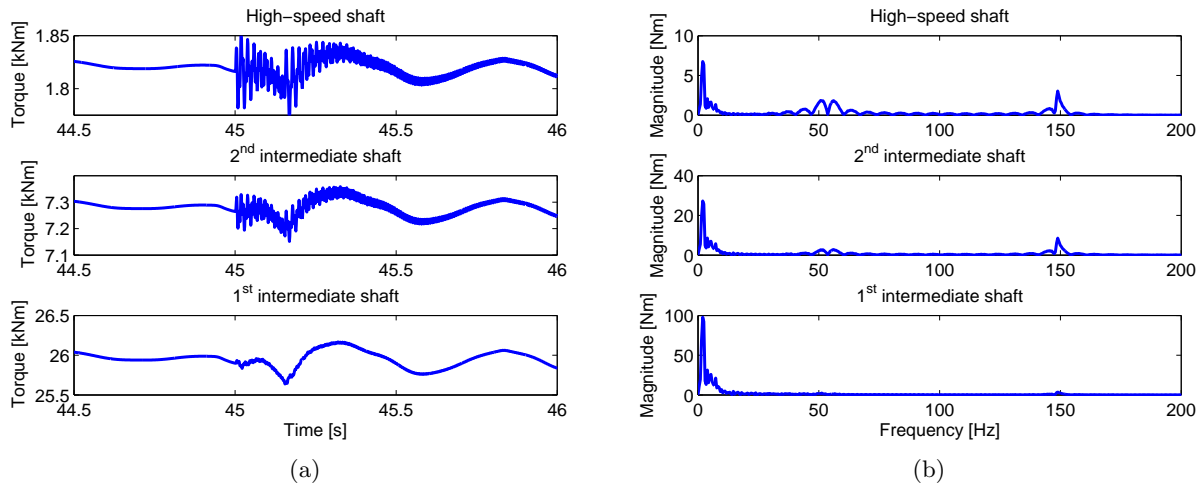


Figure 5.15: (a) Transmitted loads onto the gears because of grid excitation and (b) its frequency components.

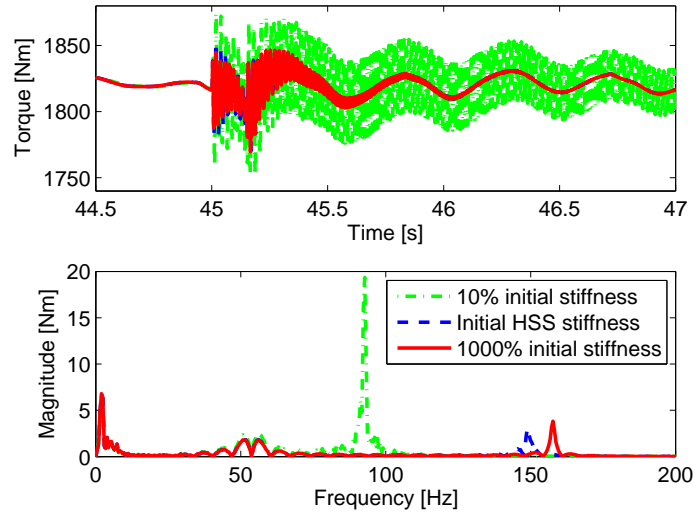


Figure 5.16: Transmitted loads onto the second parallel gear stage under various HSS stiffness values and (b) its frequency components.

electromagnetic torque excite the two lowest and most dominant modes of the drivetrain (i.e., 1.83 Hz and 154 Hz). This torque also excites the system at its excitation frequencies of 50.78 Hz and 56.15 Hz, but with less dominant effect than at the eigenfrequencies. The transmitted loads are reduced as the shaft gets further from the source of excitation, but the most dominant drivetrain eigenfrequency of 1.83 Hz prevails during the transient regime.

The developed high-fidelity drivetrain model can also be used in designing the drivetrain components to preserve or extend the life of the gearbox. In simulation analysis, this HSS stiffness was varied to 0.1 and 10 times of the nominal value to investigate its influence on the load transmitted to the gearbox. In practice, the generator and gearbox HSS are often connected through a mechanical coupler to provide for misalignment of the shafts. However, this coupler reduces the effective stiffness between the generator and the gearbox. Higher stiffness can be achieved by reducing the length of the HSS.

The transmitted loads through the HSS to the gearbox were evaluated and shown in Fig. 5.16. A lower stiffness (i.e., using coupler) appears to transmit more severe loads to the gearbox. This phenomenon is a result of reduction in the second drivetrain eigenfrequency due to the lower stiffness and vice versa, as shown in Fig. 18. The transmitted load gets amplified as the second eigenfrequency is brought down to 92.8 Hz, which is close to the second harmonics of the generator

electromagnetic torque frequencies (i.e., resonance).

5.9 Chapter Conclusions

In this chapter, the capability of the FAST aeroelastic tool is enhanced through integration of a dynamic model of a WT drivetrain built using Simscape in the MATLAB/Simulink environment. The integration of the developed drivetrain model enables FAST to be used in a number of ways. First, the model can be simulated under different wind and grid conditions to yield further insight into the drivetrain dynamics, especially in terms of predicting possible resonance excitations. Second, the integrated model can be used to simulate and understand transient loads and their couplings across the drivetrain components. Third, the model can be used to design the various flexible components of the drivetrain such that transmitted loads onto the gearbox can be reduced.

Chapter 6

Torque Controller to Mitigate Load due to Resonance

6.1 Introduction

The discussions in the previous chapter highlight the presence of resonance loads at certain operating conditions. This chapter proposes a novel controller that obviates the event of resonance while maintaining the main objective of maximizing the energy capture in region 2 operation of type 3 WT. To illustrate its application, the resonance frequency of interest is the first nonzero eigenfrequency of the drivetrain. To verify the controller capability, simulations were performed using the integrated drivetrain model of the 750-kW GRC WT established in the previous chapter. The performance of this novel controller is compared against a controller previously designed to dampen the resonance.

6.2 Campbell Diagram

A source of harmonic excitation that can induce the drivetrain resonance is the blade-pass frequency and its harmonics, represented by Eq. (5.7). Figure 6.1 shows inclined lines, which are the variation of the blade-pass frequency and its harmonics as a function of the rotor speed. The shaded region indicates the operational speed range of the WT. The red dotted horizontal line at 1.83 Hz indicates the first drivetrain eigenfrequency and the intersection between this horizontal line and any of the inclined lines indicates the occurrence of resonance at the corresponding rotor speed. Point **R** highlights a resonance due to the second harmonics of the blade-pass frequency at 18.3 RPM.

The higher drivetrain eigenfrequencies will only intersect with very high harmonics of the blade-pass frequency, which have very small excitation energy. Hence, only the first eigenfrequency is

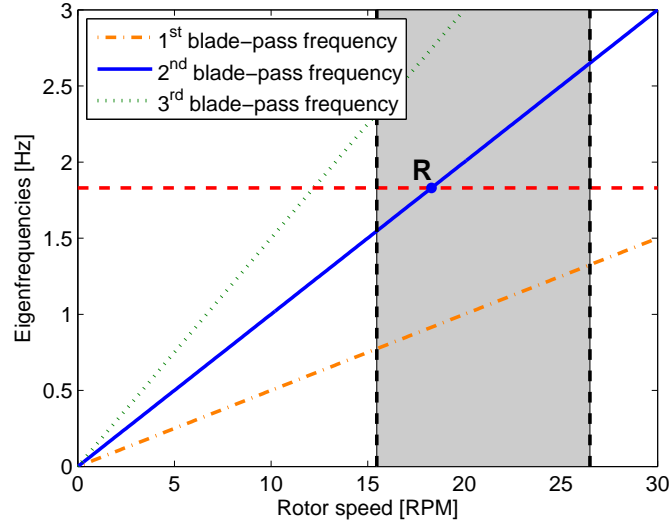


Figure 6.1: Campbell diagram of the GRC drivetrain with respect to the blade-pass frequency and its harmonics.

investigated in this chapter.

6.3 Controller Designs

To prevent excessive loads due to such resonance, a novel control method, which is based on a virtual inertia concept, is formulated. Performance of the proposed controller will be compared against a baseline stress damper controller (SDC), which is also formulated in this section. Both controllers aim to introduce a resonance compensating torque Q_{res} in the generator torque to mitigate the resonance load

$$Q_{\text{gen}} = k_{\text{opt}} \omega_{\text{rot}}^2 + Q_{\text{res}} \quad (6.1)$$

Figure 6.2 shows the control diagram of the rotor side converter of the DFIG to regulate the generator torque. The reference generator torque $Q_{\text{gen}}^{\text{ref}}$ using Eq. (6.1) can be achieved by regulating the rotor current through the current controller, which takes measurements from both the rotor and stator sides of the generator. Different uses of the two controllers in power converters to manipulate the resonance compensating torque Q_{res} are discussed as follow.

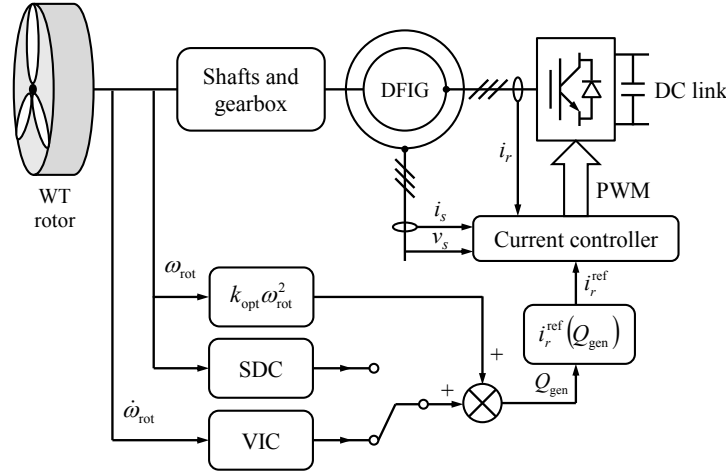


Figure 6.2: Control schematic of the DFIG rotor side converter to mitigate resonance load.

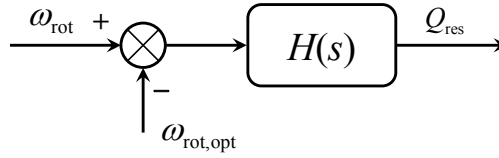


Figure 6.3: Schematic implementation of SDC.

6.3.1 Baseline SDC

The baseline SDC was first introduced in [86] and adopted by researchers in various aspects of WT operations [28, 79, 87–92]. The controller regulates the generator torque to provide additional damping at certain frequency by feeding the generator (or rotor) speed measurement through a band-pass filter (BPF) of a form

$$H(s) = G \frac{2\zeta\omega s}{s^2 + 2\zeta\omega s + \omega^2} \quad (6.2)$$

where G is the feedback gain. In this study, a narrow bandwidth of $\zeta = 0.25$ was chosen and ω was tuned to the first eigenfrequency of the drivetrain. Figure 6.3 shows the schematic implementation of the SDC. The $\omega_{\text{rot,opt}}$ is the optimum rotor speed that ensures maximum aerodynamic power capture.

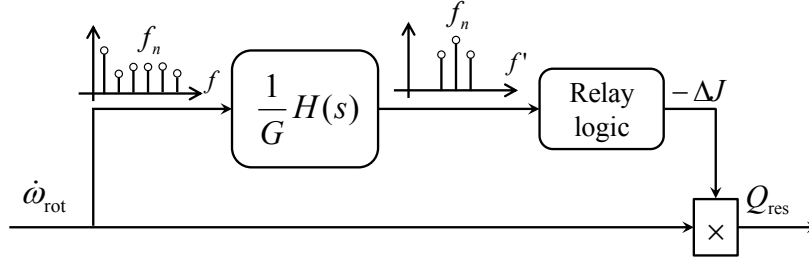


Figure 6.4: Schematic implementation of VIC.

6.3.2 Virtual Inertia Controller (VIC)

As illustrated in Eq. (5.5), the system inertias affect the eigenfrequency of the drivetrain. The equation of motion of the two-mass model of Fig. 3.1 with respect to the WT rotor side can be expressed as

$$(J_{\text{rot}} + J_{\text{eff}}) \dot{\omega}_{\text{rot}} = Q_{\text{aero}} - N Q_{\text{gen}} \quad (6.3)$$

where $\dot{\omega}_{\text{rot}} = \alpha_{\text{rot}}$ is the WT rotor acceleration. By defining the generator electromagnetic torque Q_{gen} according to Eq. (6.1) with the resonance compensating torque as

$$Q_{\text{res}} = -\Delta J \dot{\omega}_{\text{rot}} \quad (6.4)$$

It injects additional virtual inertia $\Delta J > 0$ to the drivetrain. This is to be done only if the drivetrain passes through its inherent resonance region. In doing so, the controller temporarily shifts the closed-loop eigenfrequency of the system and thus avoids the resonance. Beyond the characteristic resonance region, there is no compensating torque is required. In other words, the maximum power capture, implemented as $Q_{\text{gen}} = k_{\text{opt}} \omega_{\text{rot}}^2$, is kept intact during normal operation.

Figure 6.4 shows the schematic implementation of the compensating torque Q_{res} of VIC. The unity gain BPF of VIC is tuned according to Eq. (6.2). It is important to note that herein the BPF is used to check whether there is any excitation at the frequency of interest (i.e., the first drivetrain eigenfrequency). Logic is implemented to check the magnitude of the filter output and decide that the system is under resonance if the magnitude exceeds certain threshold. In this chapter, hysteresis logic is implemented to decide whether to add zero, medium, or high virtual inertia.

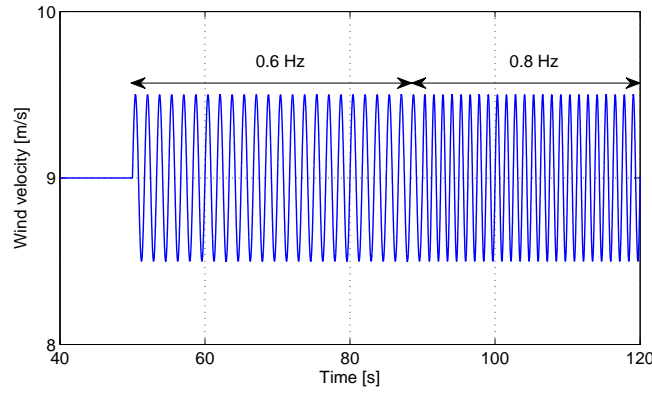


Figure 6.5: Sinusoidal wind excitation at varying frequency.

6.4 Simulation Results

The simulations using the integrated GRC WT model under different wind profiles were performed to verify the effectiveness of the proposed VIC and to compare its performance with the baseline SDC. They comprises three tests. The first one aims to investigate the performance of the controllers under a wide frequency range as well as to tune both controllers to facilitate the comparison between the two. In this first test, the simulation was performed using a hypothetical sinusoidal wind velocity input with varying frequency. The wind velocity input has average wind velocity of 9 m/s and amplitude of 0.5 m/s. Initialization for 50 s with constant wind velocity of 9 m/s was performed to allow the WT to reach steady-state condition before the harmonic excitation was applied. The frequency of excitation increases step by step from 0.6 Hz to 2.6 Hz with an increment of 0.2 Hz. Each harmonic excitation lasts for 40 s. Figure 6.5 shows the first 120 s of this sinusoidal wind excitation at 0.6 Hz and 0.8 Hz.

Figure 6.6 shows the transmitted torque through the drivetrain in terms of the rotor opposing torque Q_{opp} . The loads transmitted through other shafts within the drivetrain have similar profiles as the one shown in Fig. 6.6. As expected, a large fluctuation in the drivetrain load occurs at the sinusoidal wind excitation of 1.8 Hz (i.e., between 290 s and 330 s), which is close to the first drivetrain eigenfrequency without the electrical stiffness in Table 5.4. To facilitate a fair comparison, the gain G of SDC and the high ΔJ of VIC were tuned to achieve similar performance in mitigating the loads during the resonance between 290 s and 330 s, as shown in Fig. 6.6(c). To enhance the performance of VIC in the vicinity of resonance, a medium ΔJ is injected to the drivetrain. For

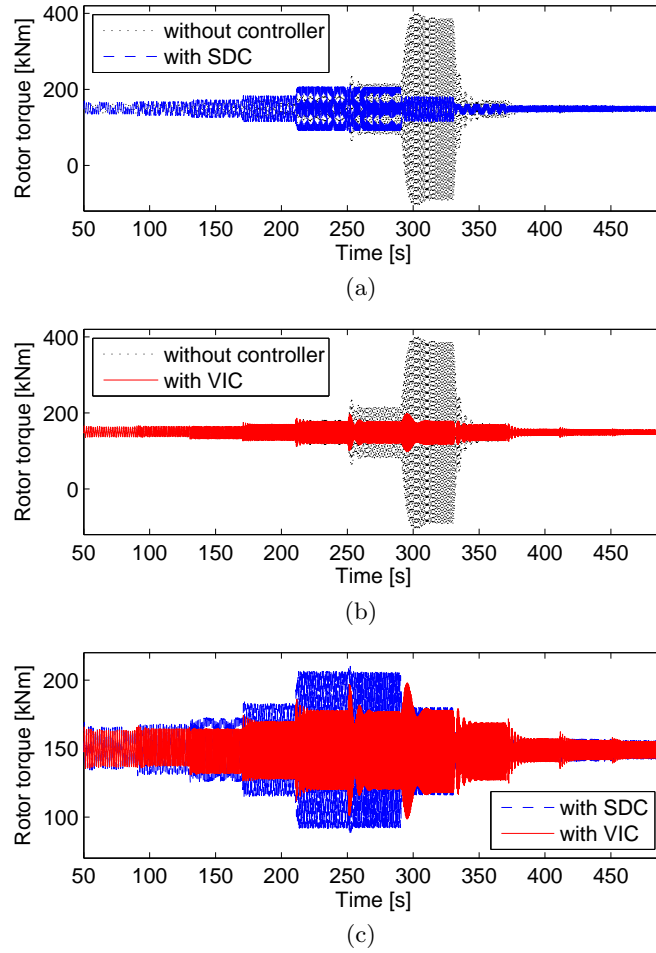


Figure 6.6: Controller comparisons in terms of transmitted drivetrain load under sinusoidal wind excitation: (a) without controller and with SDC, (b) without controller and with VIC, and (c) with SDC and VIC.

this WT, SDC gain G is 23,000 while the medium and high ΔJ are 400 and 2,500, respectively.

Under the harmonic wind excitations, both controllers are shown to be effective in mitigating the resonant loads at 1.8 Hz. However, the SDC is shown to induce additional load at another frequency location of 1.4 Hz (i.e., between 210 s and 250 s), which is the damped natural frequency. This is a major drawback as the drivetrain load at this condition becomes larger than that of without any controller, as shown in Fig. 6.6(a). On the contrary, as shown in Fig. 6.6(b), the proposed VIC specifically mitigates resonance load only around the eigenfrequency and does not amplify the response at other frequency locations.

The other two tests illustrate scenarios in which the excessive load can happen under constant wind velocity profiles. Figure 6.7 shows the simulation results under constant wind velocity of 7.25

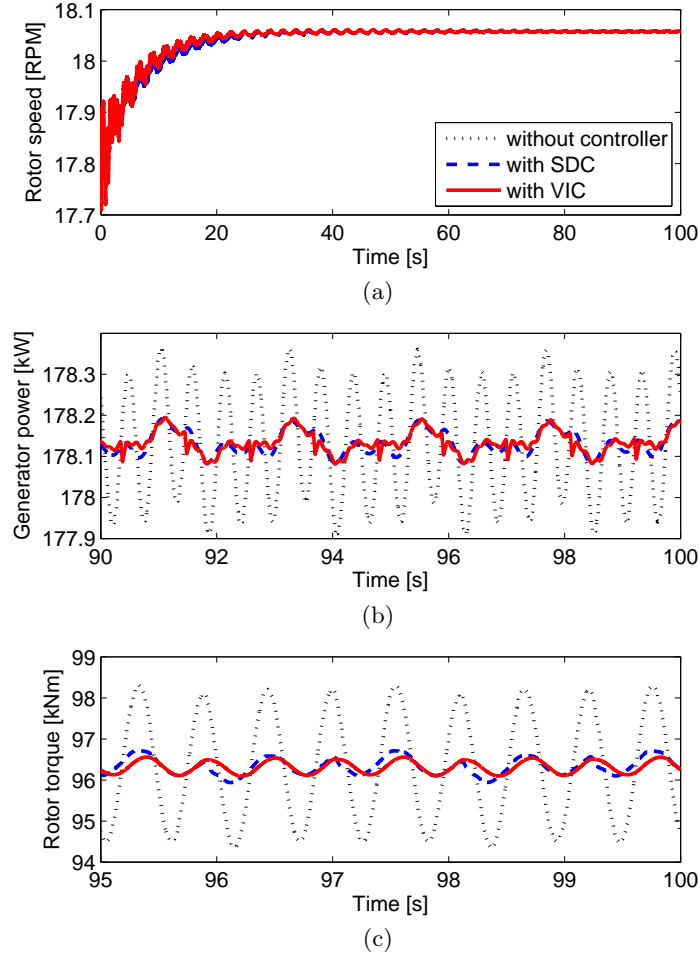


Figure 6.7: Drivetrain responses under constant wind velocity of 7.25 m/s: (a) WT rotor speed, (b) generator output power, and (c) drivetrain torsional load.

m/s. The rotational speed of the WT rotor was initialized to be 17.9 RPM. Figure 6.7(a) shows the rotor speed response that increases to reach the optimum rotor speed that ensures maximum capture of the aerodynamic power. The plot lines from the three cases (i.e., without any controllers as well as with SDC and VIC) superimpose each other that virtually only one line is visible. The maximum power capture is verified in Fig. 6.7(b), which shows the same average in the generator output power from the three cases. However, according to the Campbell diagram in Fig. 6.1, the WT drivetrain is predicted to undergo resonance due to the second harmonic of the blade-pass frequency at the rotor speed of approximately 18 RPM. The prediction is verified as large fatigue loads are transmitted within the drivetrain if no controller is being implemented, as shown in Fig. 6.7(c). Both SDC and VIC are shown to effectively reduce the fluctuations in the drivetrain load.

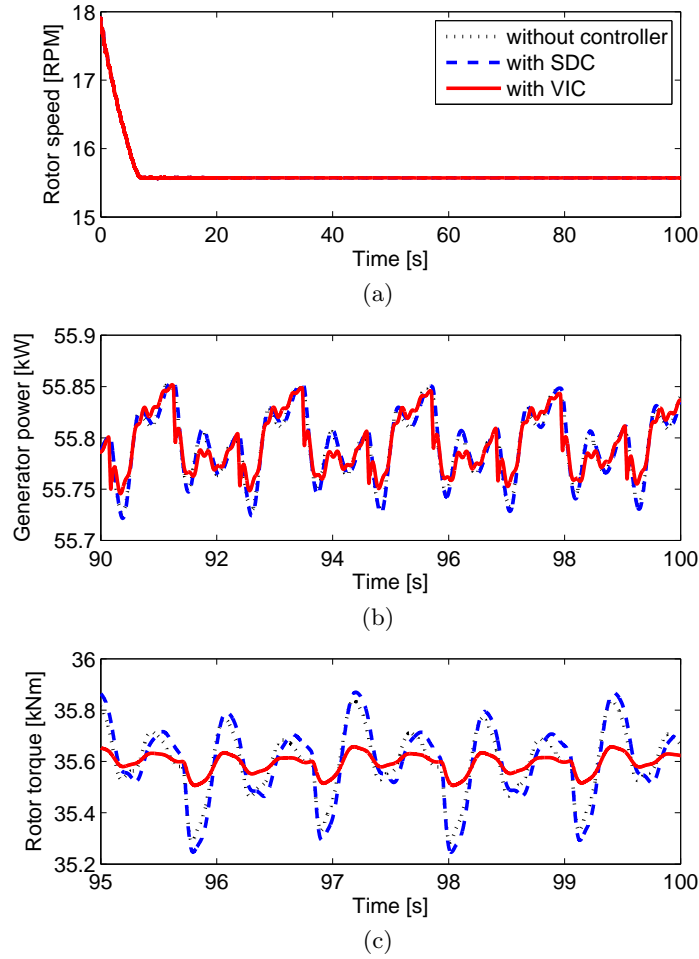


Figure 6.8: Drivetrain responses under constant wind velocity of 7.25 m/s: (a) WT rotor speed, (b) generator output power, and (c) drivetrain torsional load.

Furthermore, the controllers introduce improvement by minimizing the generator output power variation.

The third test aims to evaluate and compare the performance of the two controllers at a different operating wind velocity. Figure 6.8 shows the simulation results under constant wind velocity of 5 m/s. The rotor speed was again initialized to be 17.9 RPM. The variable-speed WT, under the three cases, is shown in Fig. 6.8(a) to successfully track the changing wind velocity to maximize the aerodynamic power capture. However, this time, the drivetrain with SDC has the largest fatigue load, as shown in Fig. 6.8(c). Therefore, if the WT spends sufficiently long period at the wind velocity of around 5 m/s, the effect of installing SDC on a variable-speed WT can be detrimental. On contrary, the VIC results in lower transmitted loads, with slightly lower power fluctuation, as

shown in Fig. 6.8(b). It occurs as this condition is still recognized as around the inherent resonance region. Thus, the controller injects a medium additional inertia ΔJ to mitigate the resonance loads.

6.5 Chapter Conclusions

This chapter proposes a novel torque control strategy in the power converters to manipulate the eigenfrequency of the WT drivetrain by introducing additional virtual inertia in the compensating torque. The VIC shifts the eigenfrequency of the system only when the drivetrain passes through its inherent resonance. Beyond the characteristic resonance region, there is no compensating torque required and the typical maximum power capture controller runs unchanged during normal operation. This is of importance as the baseline SDC has a drawback of inducing additional load at another operating condition. The simulation results show the effectiveness of the VIC, which performs better under the range of tested wind velocities and frequency excitations.

Chapter 7

Torque Controller to Mitigate Load while Providing Inertial Response

7.1 Introduction

As the number of WT connected to the grid is increasing, there have been growing demands for WTs to participate in maintaining the stability of the power system. One of which is through the provision of inertial response. Inertial response requires variable-speed WTs to inject additional energy to the grid when the grid frequency drops so that the frequency decline can be arrested.

To allow type 3 WTs to provide the inertial response, many works have proposed the implementation of supplementary control loops in the power electronics converters [93–99] so that additional energy obtained from the kinetic energy stored in the rotating mass of the WT is injected to the grid during a frequency drop. Due to its feasibility, power system operators are currently at certain stages of implementing requirements for WT’s inertial response in their system operations [9–11] and WT manufacturers have been offering inertial response capabilities in their products [100,101].

However, the impacts of inertial response on the structural loads of WT have not been given much attention. The immediate injection of energy to arrest the frequency drop requires a rapid increase in the generator torque. Such increase in torque excites transient vibrations on the structures, which in turn increases the fatigue loads and deteriorates the reliability of the WT’s components. In other words, inertial response can incur additional costs in the form of higher occurrences of failure. Therefore, it is important to discuss the dynamic loads experienced by the WT’s structures due to the inertial response to obtain more informed consideration in providing such a service.

This chapter investigates the structural loads, particularly the drivetrain load at the component-

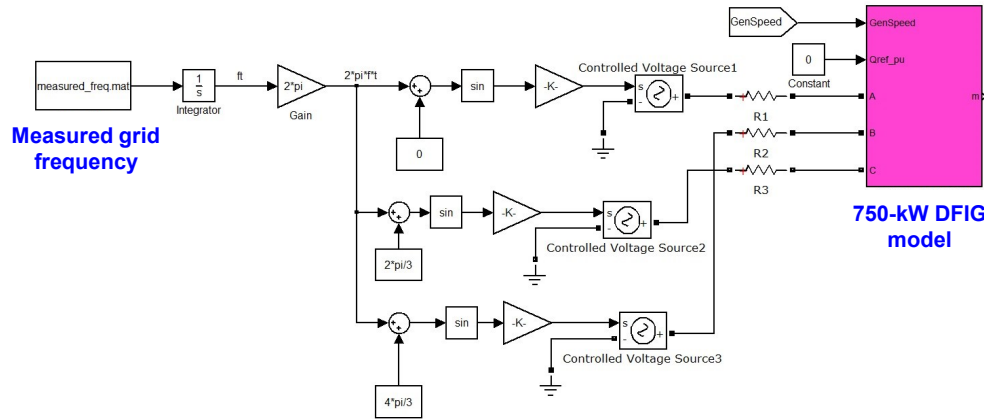


Figure 7.1: DFIG model taking measured grid frequency input.

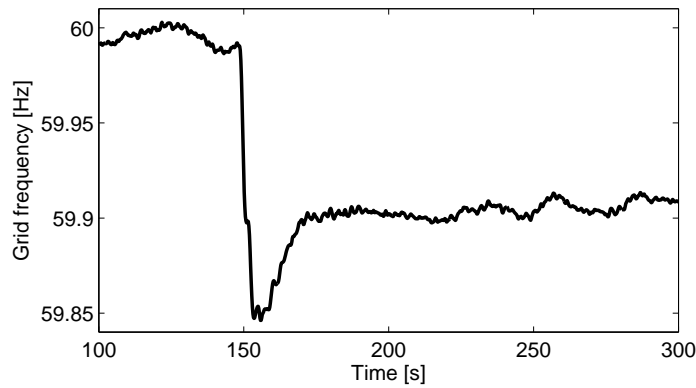


Figure 7.2: A frequency dip measured at Western Interconnection.

level, of type 3 GRC WT when providing inertial response using the developed high-fidelity WT model established in Chapter 5. This chapter also proposes a torque controller based on the concept of damper harmonic oscillator to mitigate the vibrations of the gear during the inertial response.

7.2 Generator Model

While an average model used in Chapters 5 and 6 is sufficient to represent the dynamics of DFIG at constant grid frequency, a detailed DFIG model is required to take into account the effects of grid frequency variations. Detailed generator model is available in the SimPowerSystems library [102] and were modified following the properties detailed in Appendix B. A measured grid frequency of a power system interconnection was taken as an input to the generator model, as shown in Fig. 7.1.

NREL has developed a custom monitoring system and software to autonomously and continu-

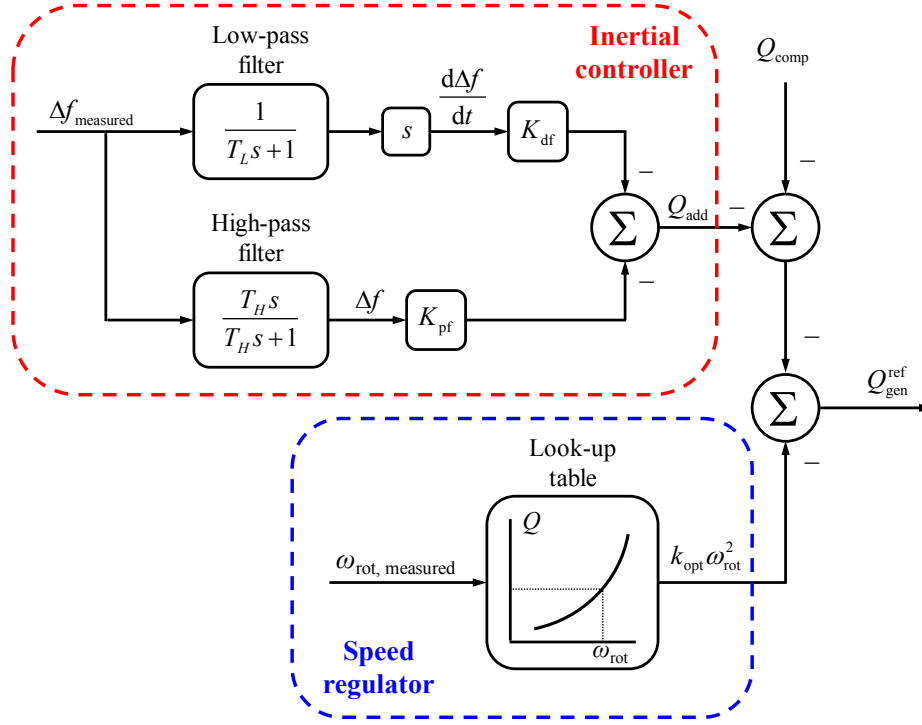


Figure 7.3: Torque controller for the rotor side converter of DFIG.

ously monitor and capture grid frequency events. One such system was installed at the National Wind Technology Center in June 2011 and has since been monitoring the frequency of the Western Interconnection in the US [103]. Figure 7.2 shows the measured frequency dip used in this chapter caused by a large loss of generation in the interconnection. It represents the event with the lowest frequency nadir ever recorded by the measurement setup.

7.3 Torque Controller for Inertial Response

Figure 7.3 shows the schematic used in this chapter to compute the reference generator torque for the rotor side converter of the DFIG to provide the inertial response. The speed regulator is the one to extract the maximum power from the wind using the quadratic torque law of Eq. (2.9). Upon a drop in grid frequency lower than 59.5 Hz, an additional term Q_{add} in pu (1 pu torque = rated generator torque) can be added to this torque setpoint to generate the inertial response. The additional torque is given by [98, 104]

$$Q_{\text{add}} = -K_{\text{df}} \frac{d\Delta f}{dt} - K_{\text{pf}} \Delta f \quad (7.1)$$

where Δf is the grid frequency deviation from the nominal frequency (i.e., $\Delta f = 60 \text{ Hz} - f$). The negative signs are to follow the convention that electric machine behaving as generator produces negative torque. The first term in Eq. (7.1) is to emulate the inherent behaviour of synchronous generators (SGs) used in conventional power plants [94], in which positive K_{df} represents virtual inertia that can be tuned arbitrarily to increase the overall system inertia [97]. The second term is to emulate the primary frequency control or droop control of conventional SGs [95], in which positive K_{pf} adds damping to the grid frequency oscillation [97].

The low-pass filter is to remove the noise from grid frequency measurement and to mitigate sudden increase in the torque setpoint, both of which can adversely vibrate the WT drivetrain. The high-pass filter is to remove the effects of steady-state deviation in the grid frequency so that the WT can return to the normal operating state of maximum power extraction after the grid frequency stabilizes.

For the simulations, the parameters for the filters were fixed as $T_L = 1$ and $T_H = 10$ leaving K_{df} and K_{pf} as the tuning parameters. Figures 7.4 and 7.5 show the WT responses under different tuning parameters at a constant uniform hub-height wind velocity of 8 m/s while the blades are pitched at the optimum angle of -3.5° . Without implementation of the inertial response (i.e., $K_{df} = K_{pf} = 0$), neither does the WT speed nor the output power change in response to the frequency deviation due to the electrical decoupling from the grid by the power electronics converters. In order to provide an inertial response resembling those of conventional SGs and type 1 generators, the parameters were tuned to achieve the synchronized operation, as recommended in [96]. Synchronized operation means that the type 3 WT speed normalized to the speed before frequency deviation follows the normalized grid frequency during the negative rate of change of frequency. Such response is achieved for this WT with $K_{df} = K_{pf} = 0.2$, as verified in Fig. 7.4. Tuning either of the parameters to a larger value, although it is feasible, results in higher kinetic energy extracted from the WT while reducing and then overshooting the WT speed excessively, as shown in Figs. 7.4 and 7.5. The synchronized operation of this WT yields up to 4% power boost for a maximum of 0.2% frequency dip. The operation then returns to the rotor speed corresponding to the maximum power extraction in less than 50 seconds.

It is important to note that for this WT, synchronized operation can be achieved with $K_{df} = K_{pf} = 0.2$ for any other measured grid frequencies and any wind velocities between 3 m/s and 12.5

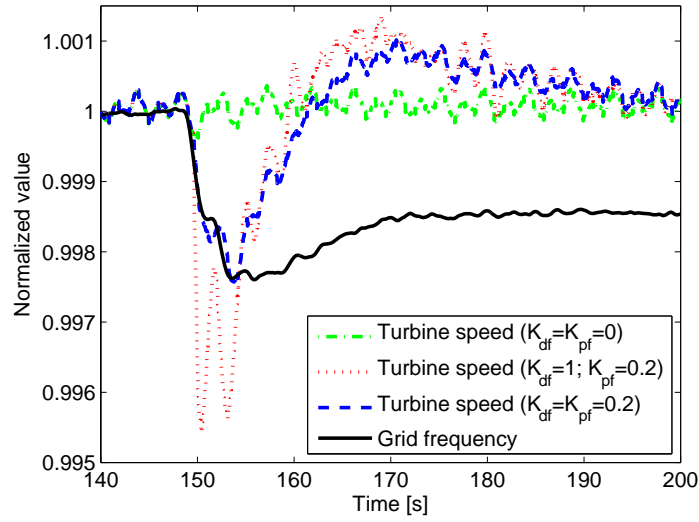


Figure 7.4: Speed response of type 3 WT at different tuning parameters.

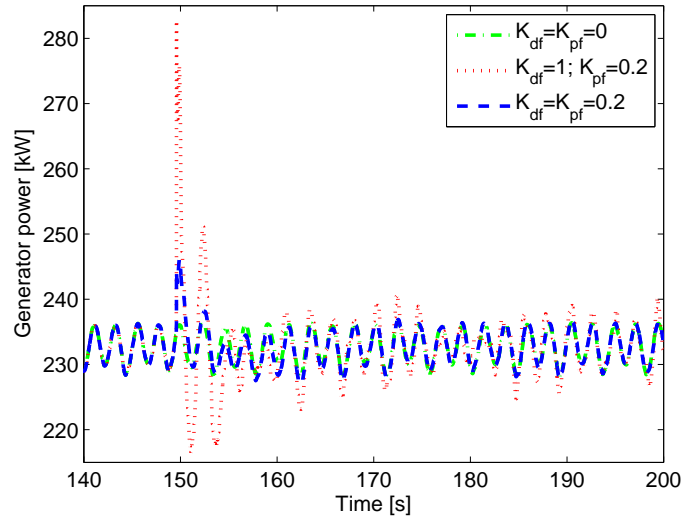


Figure 7.5: Total power delivered to the grid at different tuning parameters.

m/s, which are the cut-in and rated wind velocities of the GRC WT, respectively. For higher wind velocities during which the WT operation changes from region 2 to region 3 operations, which is not covered in this chapter, pitch controller must be implemented to maintain the rated output power and the tuning parameters need to be slightly reduced to $K_{df} = K_{pf} = 0.15$ to achieve synchronized operation.

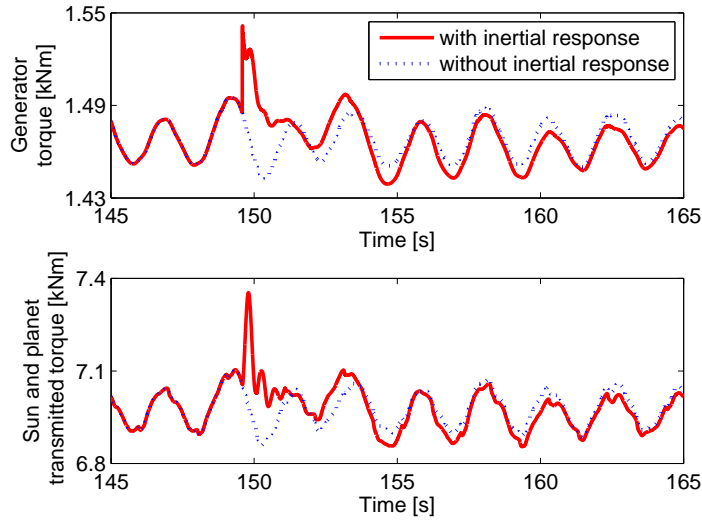


Figure 7.6: Generator torque and transmitted gear load during the inertial response.

7.4 Structural Loads due to Inertial Response

Simulations using the high-fidelity integrated model allow for investigation of the structural loads of the WT. As expressed in Eq. (7.1), the inertial response of variable-speed WT comes with higher generator torque, as verified in Fig. 7.6. This directly translates to an increase in the gear loading, which is represented in Fig. 7.6 by the increase in the transmitted torque between the sun gear and one of the three planet gears. This torque also indicates the amount of stress experienced by the gear teeth. Therefore, although it is possible to transfer higher kinetic energy from the rotating mass of the WT, as illustrated in Fig. 7.5, it is important to take into account the extent of the increased load that comes with the inertial response.

Further, due to the structural couplings, the transient excitation from the generator torque causes load fluctuations on other WT's components. Figure 7.7 shows the moments in the SS and FA directions on the top of the tower. The torque fluctuations are transmitted from the gearbox through its arm support in the form of SS rolling motion to the base plate of the nacelle, as depicted in Fig. 7.8. Such motion in turn exerts higher load on the yaw bearing at the top of the tower with the same profile as the load fluctuations of the gearbox. Meanwhile, the tower FA motion and load are not affected by the drivetrain excitation.

Figure 7.9 shows the moments in the SS and FA directions at the base of the tower, (i.e., the

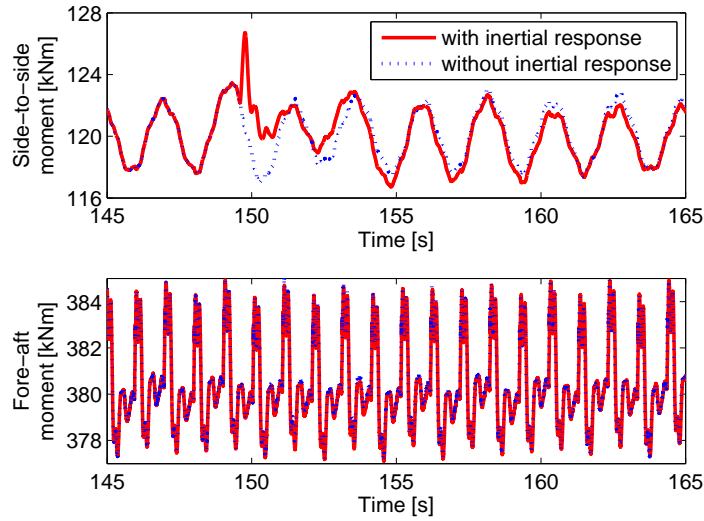


Figure 7.7: Loads on the tower-top during the inertial response.

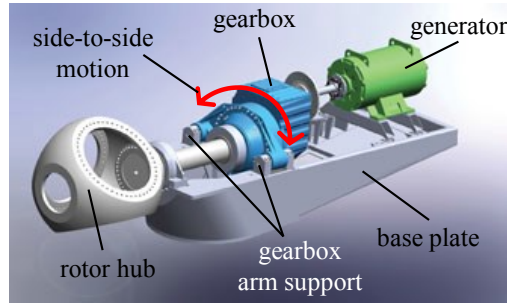


Figure 7.8: Coupling between drivetrain torque and tower-top SS moment, adapted from [17].

loads exerted on the WT foundation). It shows reductions in the tower-base loads due to the slowing down of the WT during the inertial response. As the WT speed reduces, the aerodynamic thrust and torque reduce [21], respectively contributing to the lower FA and SS loads during the inertial response. Simulations using a more aggressive inertial controller represented by the red dotted line in Figs. 7.4 and 7.5 verified the more significant reductions in the tower-base loads as the WT gets slower. The difference between the blade loads with and without inertial response is negligible and hence not shown.

A closer look into the transient responses of the generator during the inertial response is shown Fig. 7.10. It shows an excitation from the generator torque to the drivetrain at approximately 58.6 Hz for the first 0.3 s since the commencement of the inertial response. Similar to the observation in Fig. 5.14 using an average DFIG model, this high-frequency excitation is inherent to the generator,

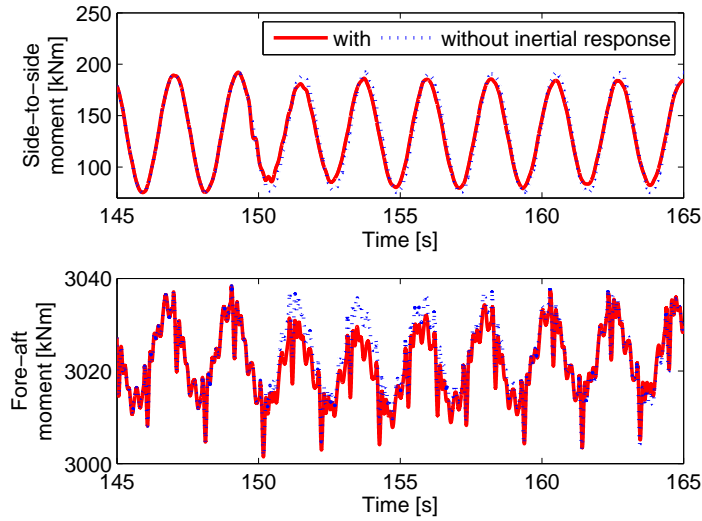


Figure 7.9: Loads on the tower-base during the inertial response.

the influence of which can only be accurately investigated using a high order drivetrain model. As shown in Fig. 7.11, the instantaneous deliverance of power to the grid introduces some torsional vibrations to the drivetrain. Because the magnitude of the high-frequency excitation is small and it does not match with any of the eigenfrequencies of the drivetrain, only the first eigenfrequency of the drivetrain at 1.83 Hz gets excited during the transient response of the drivetrain load. Nevertheless, this transient vibration contributes to an increase in the fatigue load that in a long run can fail or crack the gear teeth or other drivetrain components.

To quantify the impact of such excitations, the resulting structural loads from $t = 100$ s and $t = 200$ s (i.e., approximately 50 s before and after the grid frequency drops below 59.95 Hz for the first time) were used to compute the DELs. The resulting fatigue loads on different WT's components are summarized in Table 7.1. It shows that the provision of inertial response increases the fatigue load of variable-speed WT gears by 75.03% and the SS moment of the yaw bearing on the top of the tower by 0.57%. However, the inertial response reduces the fatigue loads of the FA moment of the yaw bearing by 0.07%. The load reductions are more prominent on the SS and FA moments of the tower-base, respectively by 5.13% and 2.17%, due to the slowing down of the WT.

To mitigate the increase in the gear fatigue load, a compensating torque Q_{comp} based on the

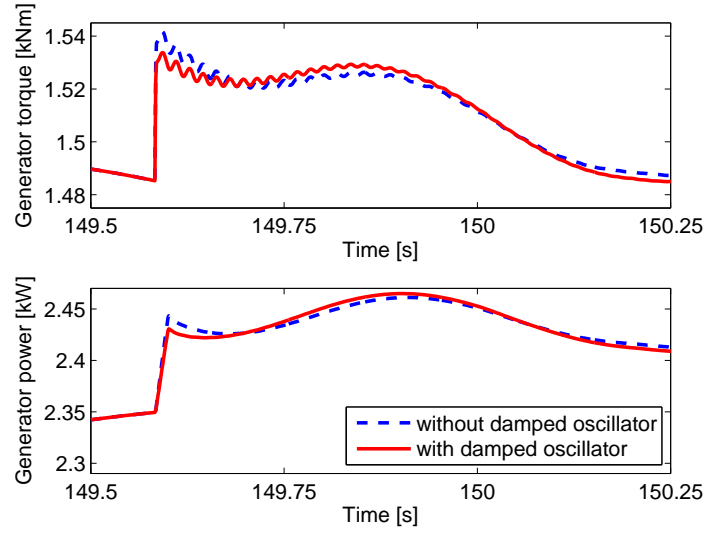


Figure 7.10: Generator responses in terms of torque and output power during inertial response with and without damped oscillator.

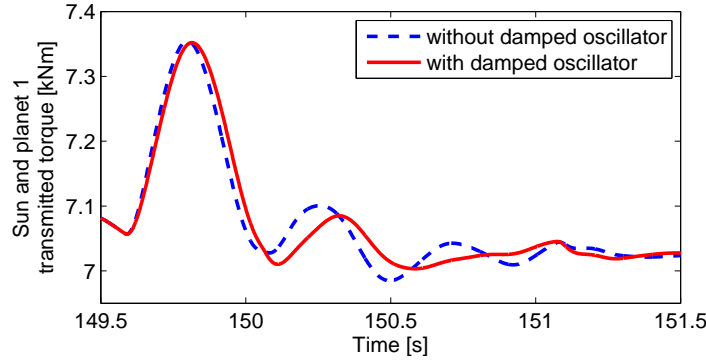


Figure 7.11: Gear transmitted load during inertial response with and without damped oscillator.

concept of damped harmonic oscillator concept [105] is proposed, which is defined as

$$Q_{\text{comp}} = -K \frac{s^2}{s^2 + 2\zeta\omega s + \omega^2} \quad (7.2)$$

The profile of the compensating torque is shown in Fig. 7.12 where the damped period of oscillation is defined as $T = \frac{2\pi}{\omega\sqrt{1-\zeta^2}}$. The compensating torque along with the other torque commands are superimposed to yield the reference torque Q_{ref} for the rotor-side converter, as shown in Fig. 7.3.

Because there is not any feedback in determining the compensating torque, proper tuning of the parameters is important to effectively mitigate the drivetrain load. For the simulations of this work, $K = 0.02$, $\zeta = 0.15$, and $\omega = 2\pi f_e$ was tuned to the first eigenfrequency of the drivetrain

Table 7.1: DELs of WT's Components

Structural Loads	No Inertial Response	With Inertial Response		Compensated Inertial Response	
Sun and planet 1 gears transmitted torque	156.2 Nm	273.4 Nm	75.03%	272.3 Nm	−0.40%
Tower-top					
SS bending moment	3.881 kNm	3.903 kNm	0.57%	3.893 kNm	−0.26%
FA bending moment	7.091 kNm	7.086 kNm	−0.07%	7.085 kNm	−0.01%
Tower-base					
SS bending moment	87.96 kNm	83.45 kNm	−5.13%	83.43 kNm	−0.02%
FA bending moment	24.84 kNm	24.3 kNm	−2.17%	24.3 kNm	—
Blade 1 Root					
Flapwise bending moment	36.86 kNm	36.86 kNm	—	36.86 kNm	—
Edgewise bending moment	448.6 kNm	448.6 kNm	—	448.6 kNm	—

(i.e. $f_e = 1.8$ Hz). The responses of the generator during the inertial response with the tuned compensating torque is shown in Fig. 7.10. There are slight reductions in the initial torque, and correspondingly initial output power of the generator, because the compensating generator torque fluctuates more in the beginning to counteract the transient vibration of the drivetrain. As a result, the gears experience less oscillatory loads, as shown in Fig. 7.11.

The introduction of the compensating torque brings about improvements in the fatigue loads of the WT, as shown in Table 7.1. Compared with the loads without any compensation, the compensating torque reduces the coupled gears and yaw bearing SS fatigue loads by 0.40% and 0.26%, respectively. Although the improvement seems marginal, the difference can be beneficial in the long run over many occurrences of grid frequency decline. The effects of the compensation on the loads of other components are marginal because the small amplitude of the compensating torque does not affect the WT speed.

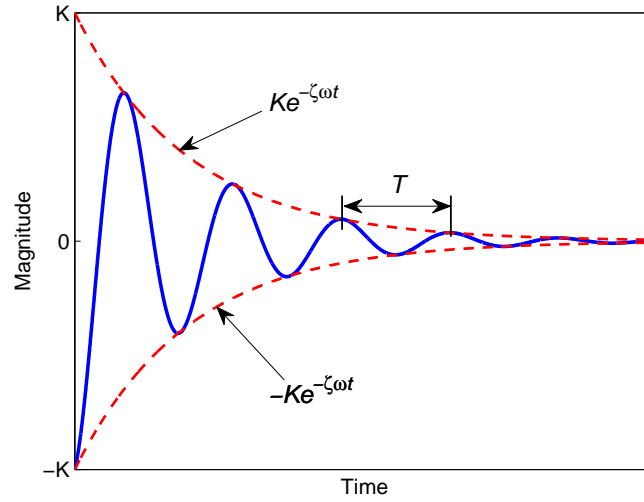


Figure 7.12: Parameters of the compensating torque based on damped harmonic oscillator.

7.5 Chapter Conclusions

The inertial response of type 3 WTs can be achieved through implementation of supplementary control loops so that additional energy obtained from the kinetic energy stored in the rotating mass of the WT can be injected to the grid during a frequency drop. However, the impacts of inertial response on the structural loads of a WT have not been given much attention. This chapter investigates the impacts using the high-fidelity GRC WT model. The results show that the inertial response increases the fatigue load of type 3 WT gears and the SS moment of the yaw bearing while reducing the fatigue loads of the FA moment of the yaw bearing, the SS and FA moments of the tower-base. Because of the increase in the gear fatigue load, this chapter proposes a torque controller based on the concept of damper harmonic oscillator to mitigate the vibrations of the gear during the inertial response. The high-fidelity WT model have enabled the design and validation of the proposed controller. It shows that the introduction of such compensation yields mitigation on the fatigue loads of the gears and the yaw bearing in the SS direction.

Chapter 8

Concluding Remarks

8.1 Thesis Conclusions

Following up Fig. 2.1, Fig. 8.1 summarizes the main contribution of this thesis. In this thesis, various controller designs and performance validations to mitigate the blade and drivetrain loads of type 3 (i.e., DFIG-based) WT have been presented. It has also been shown that the load mitigating controllers also yielded improvement in the quality of the output power. The controllers were designed to attenuate loads in ways that have not been paid much attention before and verified to yield superior load attenuation as compared with the ones achieved by industrial standards.

The blade loads are of primary concerns at high wind velocities above the rated wind velocity (i.e., region 3 operation). At such operating conditions, the blades are pitched to ensure that aerodynamic power is being extracted at the WT rating while the generator torque is kept constant at its rated value. In Chapter 3, a new control strategy was presented based on the concept of stochastic disturbance accommodating control for variable pitch WTs to compensate for the unmodeled dynamics, (i.e., the neglected modes during the design of the controller), changing wind velocity, and measurement noise. Kalman estimator was used in designing the SDAC for CPC to stabilize the WT that was otherwise unstable due to the unmodelled dynamic coupling between the drivetrain and other WT components. To investigate the performance of the proposed control scheme, simulations were performed under turbulent wind conditions with various mean velocities and turbulence intensities. It was shown that the SDAC was able to achieve better speed regulation and lower drivetrain loads under the tested wind conditions. It was expected that the additional objective of dampening the drivetrain load would increase the control cost. Nonetheless, due to the nature of turbulent wind and the implementation of integral anti windup in the GSPI controller,

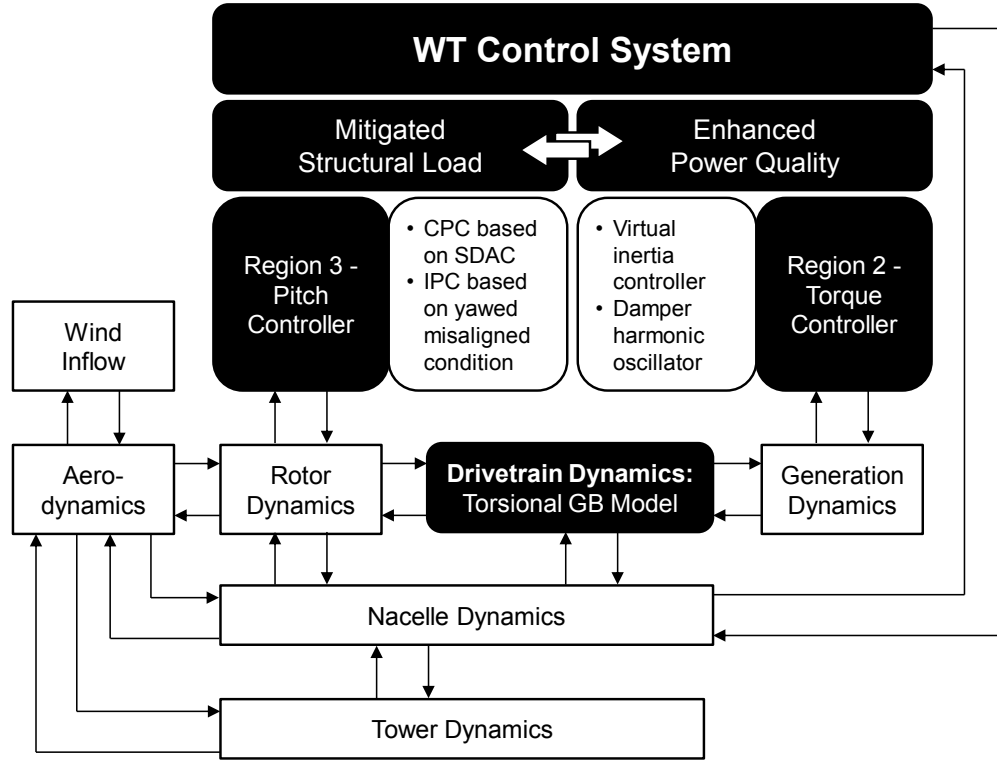


Figure 8.1: Contributions of the thesis: integration of drivetrain model as well as designs of pitch and generator torque controllers.

the proposed SDAC could sometime result in a lower control cost.

IPC is required because CPC is inherently not able to take into account the blade load variations caused by the vertical wind shear. So far in pitch controller designs, the wind field is assumed to have no misalignment with respect to the rotor plane. However, it was shown that yaw misalignment could yield significant reduction in blade moment variations caused by wind shear. Therefore, in Chapter 4 a novel LQR-based MIMO IPC was designed considering a WT model linearized at a yawed inflow condition. The proposed IPC was decoupled from the yaw controller, allowing implementation of conventional yaw controllers that aim to align the WT with the wind. Performance of the controller was compared with that of the baseline CPC and IPC through simulations under various turbulent wind conditions. The results showed that the proposed controller yielded significant attenuations in the blade-root OOP bending moments as well as tower-base FA and SS bending moments. Therefore, the proposed controller design could bring benefits in increasing the reliability of the overall WT components.

For wind velocities below the rated wind velocity, the WT operates to capture as much wind

energy as possible. At such operating conditions, there is an optimum WT rotor speed, which is a function of the oncoming wind velocity, that ensures maximum energy capture. This optimum WT rotor speed is achieved by controlling the generator torque while the blade pitch angles are fixed at the optimum value. While achieving the desired optimum speed, the WT is being exposed to various aerodynamic excitations on one hand and grid excitations on the other. To gain insights on the internal drivetrain loadings under such condition as well as to design and verify controllers focusing to mitigate them, a high-fidelity WT model is required.

In Chapter 5, an integrated WT model coupling high-fidelity aerodynamic, structural, drivetrain and electrical models was proposed. The capability of the FAST aeroelastic tool was enhanced through integration of a dynamic model of a WT drivetrain built using Simscape in the MATLAB/Simulink environment. Some applications of the developed model was demonstrated. The model could be simulated under different wind and grid conditions to yield further insight into the drivetrain dynamics in terms of predicting possible resonance excitations. The integrated model was able to simulate transient loads and their couplings across the drivetrain components. It could also be used to design the various flexible components of the drivetrain such that transmitted loads onto the gearbox could be reduced.

In Chapter 6, a novel torque control strategy was designed to manipulate the eigenfrequency of the WT drivetrain by introducing additional virtual inertia in the compensating torque. It was shown that the VIC shifted the eigenfrequency of the system only when the drivetrain passed through its inherent resonance due to the blade-pass frequency. Beyond the characteristic resonance region, there was no compensating torque required and the typical maximum power capture controller ran unchanged during normal operation. This is of importance because the baseline SDC suffers from a drawback of inducing additional load at the damped eigenfrequency. The simulation results showed the effectiveness of the VIC, which performed better under the range of tested wind velocities and frequency excitations. It was also shown that obviating resonance directly improves the power quality by mitigating the fluctuations in the output power.

In Chapter 7, the impacts of inertial response on the structural loads of a WT were investigated using the high-fidelity GRC WT model. The results showed that the inertial response increased the fatigue load of type 3 WT gears and the SS moment of the yaw bearing while reducing the fatigue loads of the FA moment of the yaw bearing, the SS and FA moments of the tower-base. Because of

the increase in the gear fatigue load, this chapter proposed a torque controller based on the concept of damper harmonic oscillator to mitigate the vibrations of the gear during the inertial response. The high-fidelity WT model have enabled the design and validation of the proposed controller. It showed that the introduction of such compensation yielded mitigation on the fatigue loads of the gears and the yaw bearing in the SS direction.

In summary, the works of this thesis have contributed into:

- New design of MIMO IPC based on recent findings by other researchers on the benefit of yawed inflow that can alleviate the out-of-plane bending moment of WT blades. The new IPC design can be implemented using the same input-output configurations of the existing IPC while shown to yield superior performance under simulated wind conditions.
- New application of stochastic control on disturbance accommodating control to stabilize the close-loop WT system that, in existing design, is unstable due to unmodeled dynamics. The application is illustrated through the use of Kalman Estimator in the design of SISO CPC that yield alleviated drivetrain loads compared to the baseline SISO PI-based CPC.
- New integration of higher fidelity drivetrain model to enhance the capability of FAST, a well-known and certified WT aero-elastic tool. The high fidelity drivetrain model has been verified through comparisons of eigenfrequencies against both well-known planetary gearbox models and several drivetrain test data on full-scale operating WTs.
- New insights on possible sources of deteriorating drivetrain loads from the integrated drivetrain model in FAST; such as resonant loads from wind excitations (low frequency excitations) and grid excitations (high frequency excitations). Further verifications using data from real operating WTs are essential to justify these findings. However, such data are hard to find.
- New proposed controller designs that add virtual inertia either to the drivetrain (to alleviate drivetrain resonant loads) or to the grid (to support the grid during frequency drops and to alleviate transient drivetrain vibrations). Such controllers are shown to effectively alleviate the drivetrain loads through simulations using the integrated high fidelity drivetrain model under realistic wind and grid conditions.

8.2 Recommendations

Further work might include coupling the pitch controller with the yaw controller to yield better blade load mitigation. Feedforward control strategies using advanced wind sensing technology such as LIDAR (Light Detection and Ranging) can be integrated to capture the incoming wind conditions. Although it may result in increased yaw rate and gyroscopic forces on the nacelle, the prospects of blade load mitigation are worth exploring.

The effectiveness of control strategies to mitigate resonance load due to high frequency excitations, higher than the discussed blade-pass frequency, can also be explored. Harmonic excitations from generator dynamics or from gear faults can excite higher drivetrain eigenfrequencies, the influence of which has not been much investigated.

The proposed damped harmonic oscillator is sensitive to the drivetrain properties. Robust control strategies can be explored in case the actual eigenfrequency and damping of the drivetrain are very different from the one used in the controller design.

References

- [1] R. Pernick, C. Wilder, and T. Winnie, *Clean Energy Trends 2012*. The Clean Edge Market Authority, 2012.
- [2] Stefan Gsänger, *Half-year Report*. World Wind Energy Association, 2014.
- [3] European Wind Energy Association, “Design limits and solutions for very large wind turbines,” Tech. Rep., UpWind, 2011.
- [4] M. Crawford, “Wind turbines get bigger and smarter,” July 2013. [Online]. Available: <https://www.asme.org/engineering-topics/articles/renewable-energy/wind-turbines-get-bigger-smarter>.
- [5] A. D. Wright, *Modern Control Design for Flexible Wind Turbines*. PhD thesis, University of Colorado at Boulder, 2004.
- [6] K. A. Kragh and M. H. Hansen, “Load alleviation of wind turbines by yaw misalignment,” *Wind Energy*, vol. 17, no. 7, pp. 971–982, 2014.
- [7] B. Hahn, M. Durstewitz, and K. Rohrig, “Reliability of wind turbines,” in *Wind Energy* (J. Peinke, P. Schaumann, and S. Barth, eds.), pp. 329–332, Springer Berlin Heidelberg, 2007.
- [8] S. Faulstich, B. Hahn, and P. J. Tavner, “Wind turbine downtime and its importance for offshore deployment,” *Wind Energy*, vol. 14, no. 3, pp. 327–337, 2011.
- [9] S. Sharma, S.-H. Huang, and N. Sarma, “System nertial frequency response estimation and impact of renewable resources in ERCOT interconnection,” in *2011 IEEE Power and Energy Society General Meeting*, pp. 1–6, Jul 2011.

- [10] J. Brisebois and N. Aubut, “Wind farm inertia emulation to fulfill Hydro-Québec’s specific need,” in *2011 IEEE Power and Energy Society General Meeting*, pp. 1–7, July 2011.
- [11] N. W. Miller, M. Shao, S. Venkataraman, C. Loutan, and M. Rothleder, “Frequency response of California and WECC under high wind and solar conditions,” in *2012 IEEE Power and Energy Society General Meeting*, pp. 1–8, July 2012.
- [12] J. M. Jonkman and M. L. J. Buhl, “FAST user’s guide,” Tech. Rep. NREL/EL-500-38230, The National Renewable Energy Laboratory, Golden, Colorado, 2008.
- [13] Germanischer Lloyd WindEnergie GmbH, “*FAST and ADAMS incl. AeroDyn Module*,” 2005. ZZ 001A-2005.
- [14] B. J. Jonkman, “*TurbSim Users Guide: Version 1.50*,” Tech. Rep. NREL/TP-500-46198, The National Renewable Energy Laboratory, Golden, Colorado, 2009.
- [15] IEC 61400-1, *Wind turbines Part 1: Design requirements*. Geneva, Switzerland: International Electrotechnical Commission, 3rd ed., 2005.
- [16] P. J. Moriarty and A. C. Hansen, “AeroDyn theory manual,” Tech. Rep. NREL/EL-500-38230, The National Renewable Energy Laboratory, Golden, Colorado, 2004.
- [17] J. Jonkman, S. Butterfield, W. Musial, and G. Scott, “Definition of a 5-MW reference wind turbine for offshore system development,” Tech. Rep. NREL/TP-500-38060, The National Renewable Energy Laboratory, Golden, Colorado, 2009.
- [18] F. Oyague, “*Gearbox Reliability Collaborative (GRC) Description and Loading*,” Tech. Rep. NREL/TP-5000-47773, The National Renewable Energy Laboratory, Golden, Colorado, November 2011.
- [19] M. Singh, E. Muljadi, V. Gevorgian, and S. Santoso, “Wind power generation,” in *Power Electronics for Renewable and Distributed Energy Systems* (S. Chakraborty, M. G. Simes, and W. E. Kramer, eds.), Green Energy and Technology, pp. 111–149, Springer London, 2013.

- [20] M. Singh, E. Muljadi, J. Jonkman, V. Gevorgian, I. Girsang, and J. Dhupia, "Simulation for wind turbine generator with FAST and MATLAB/Simulink modules," Tech. Rep. NREL/TP-5500-59195, The National Renewable Energy Laboratory, Golden, Colorado, 2009.
- [21] T. Burton, N. Jenkins, D. Sharpe, and E. Bossanyi, *Wind Energy Handbook*. John Wiley & Sons, 2011.
- [22] E. Muljadi and C. Butterfield, "Pitch-controlled variable-speed wind turbine generation," *Industry Applications, IEEE Transactions on*, vol. 37, pp. 240–246, Jan 2001.
- [23] E. L. van der Hooft, P. Schaak, and T. G. van Engelen, "Wind turbine control algorithms," Tech. Rep. ECN-C-03-111, The Energy Research Center of the Netherlands, 2003.
- [24] J. H. Laks, L. Y. Pao, and A. D. Wright, "Control of wind turbines: Past, present, and future," in *American Control Conference*, pp. 2096–2103, 2009.
- [25] L. Y. Pao and K. Johnson, "Control of wind turbines," *Control Systems, IEEE*, vol. 31, pp. 44–62, April 2011.
- [26] K. Pierce, "Control method for improved energy capture below rated power," in *3rd ASME/JSME Joint Fluids Engineering Conference*, pp. 1–6, 1999.
- [27] K. E. Johnson, L. J. Fingersh, M. J. Balas, and L. Y. Pao, "Methods for increasing region 2 power capture on a variable-speed wind turbine," *Journal of solar energy engineering*, vol. 126, no. 4, pp. 1092–1100, 2004.
- [28] E. A. Bossanyi, "Wind turbine control for load reduction," *Wind Energy*, vol. 6, no. 3, pp. 229–244, 2003.
- [29] A. D. Wright, L. J. Fingersh, and K. A. Stol, "Testing controls to mitigate fatigue loads in the controls advanced research turbine," in *17th Mediterranean Conference on Control and Automation*, (Thessaloniki, Greece), pp. 1275–1282, 2009.
- [30] J. M. Jonkman, *Dynamics Modeling and Loads Analysis of an Offshore Floating Wind Turbine*. PhD thesis, University of Colorado at Boulder, 2007.

- [31] I. P. Girsang and J. S. Dhupia, "Performance of linear control methods for wind turbines dealing with unmodeled structural modes," in *ASME Dynamic Systems and Control Conference*, vol. 3, (Fort Lauderdale, Florida), pp. 645–652, 2012.
- [32] H. Hendriks and B. Bulder, "Fatigue equivalent load cycle method. a general method to compare the fatigue loading of different load spectrums," Tech. Rep. ECN-95-074, The Energy Research Center of the Netherlands, October 1995.
- [33] F. Mouzakis, E. Morfiadakis, and P. Dellaportas, "Fatigue loading parameter identification of a wind turbine operating in complex terrain," *Journal of Wind Engineering and Industrial Aerodynamics*, vol. 82, no. 1, pp. 69–88, 1999.
- [34] G. Freebury and W. Musial, "Determining equivalent damage loading for full-scale wind turbine blade fatigue tests," in *19th American Society of Mechanical Engineers Wind Energy Symposium*, (Reno, Nevada), 2000.
- [35] S. D. Downing and D. Socie, "Simple rainflow counting algorithms," *International Journal of Fatigue*, vol. 4, no. 1, pp. 31–40, 1982.
- [36] G. J. Hayman and M. L. Buhl Jr., "MLife users guide for version 1.00," tech. rep., The National Renewable Energy Laboratory, Golden, Colorado, 2012.
- [37] C. D. Johnson, "Theory of disturbance accommodating controllers," *Control and Dynamic Systems*, vol. 12, pp. 387–489, 1976.
- [38] C. D. Johnson, "Disturbance-accommodating control; an overview," in *American Control Conference*, (Seattle, Washington), pp. 526–536, 1986.
- [39] K. Stol and M. J. Balas, "Periodic disturbance accommodating control for speed regulation of wind turbines," in *Proceedings of AIAA/ASME Wind Energy Symposium*, (Reno, Nevada), pp. 310–320, 2002.
- [40] M. Balas, Y. J. Lee, and L. Kendall, "Disturbance tracking control theory with application to horizontal axis wind turbine," in *Proceedings of AIAA/ASME Wind Energy Symposium*, (Reno, Nevada), pp. 95–99, 1998.

-
- [41] S. A. Frost, M. J. Balas, and A. D. Wright, "Direct adaptive control of a utility-scale wind turbine for speed regulation," *International Journal of Robust and Nonlinear Control*, vol. 19, no. 1, pp. 59–71, 2009.
- [42] M. M. Hand and M. J. Balas, "Blade load mitigation control design for a wind turbine operating in the path of vortices," *Wind Energy*, vol. 10, no. 4, pp. 339–355, 2007.
- [43] A. D. Wright and P. Fleming, "Refinements and tests of an advanced controller to mitigate fatigue loads in the controls advanced research turbine," in *Proceedings of the 49th AIAA Aerospace Sciences Meeting*, (Orlando, Florida), 2011.
- [44] J. George, P. Singla, and J. Crassidis, "Stochastic disturbance accommodating control using a kalman estimator," in *AIAA Guidance, Navigation and Control Conference and Exhibit*, (Honolulu, Hawaii), 2008.
- [45] H. E. Merritt, *Hydraulic Control Systems*. New York: Wiley, 1967.
- [46] P. F. Odgaard, J. Stoustrup, and M. Kinnaert, "Fault tolerant control of wind turbines a benchmark model," in *Proceedings of the 7th IFAC Symposium on Fault Detection, Supervision and Safety of Technical Processes*, (Barcelona, Spain), pp. 155–160, IFAC, 2009.
- [47] F. Dunne, L. Y. Pao, A. D. Wright, B. Jonkman, and N. Kelley, "Adding feedforward blade pitch control to standard feedback controllers for load mitigation in wind turbines," *Mechatronics*, vol. 21, no. 4, pp. 682 – 690, 2011.
- [48] D. Schlipf, L. Pao, and P. W. Cheng, "Comparison of feedforward and model predictive control of wind turbines using lidar," in *2012 IEEE 51st Annual Conference on Decision and Control*, pp. 3050–3055, 2012.
- [49] J. H. Laks, L. Y. Pao, A. D. Wright, N. Kelley, and B. Jonkman, "The use of preview wind measurements for blade pitch control," *Mechatronics*, vol. 21, no. 4, pp. 668 – 681, 2011.
- [50] IEC 61400-12, *Wind turbine generator systems - Part 12: Wind turbine power performance testing*. Geneva, Switzerland: International Electrotechnical Commission, first ed., 1996.

- [51] E. A. Bossanyi, "Individual blade pitch control for load reduction," *Wind Energy*, vol. 6, no. 2, pp. 119–128, 2003.
- [52] E. A. Bossanyi, "Further load reductions with individual pitch control," *Wind Energy*, vol. 8, no. 4, pp. 481–485, 2005.
- [53] E. Bossanyi, B. Savini, M. Iribas, M. Hau, B. Fischer, D. Schlipf, T. Engelen, M. Rossetti, and C. Carcangiu, "Advanced controller research for multi-MW wind turbines in the UPWIND project," *Wind Energy*, vol. 15, no. 1, pp. 119–145, 2012.
- [54] M. Jelavić, V. Petrović, and N. Perić, "Estimation based individual pitch control of wind turbine," *Automatika*, vol. 51, no. 2, pp. 181–192, 2010.
- [55] T. G. van Engelen, "Design model and load reduction assessment for multi-rotational mode individual pitch control (higher harmonics control)," in *European Wind Energy Conference*, (Athens, Greece), 2006.
- [56] T. J. Larsen, H. A. Madsen, and K. Thomsen, "Active load reduction using individual pitch, based on local blade flow measurements," *Wind Energy*, vol. 8, no. 1, pp. 67–80, 2005.
- [57] K. A. Stol, A. D. Wright, and W. Zhao, "Individual blade pitch control for the controls advanced research turbine (CART)," *Journal of Solar Energy Engineering*, vol. 128, no. 4, pp. 498–505, 2006.
- [58] I. P. Girsang and J. S. Dhupia, "Pitch control for wind turbine in yawed inflow condition," in *ASME Dynamic Systems and Control Conference*, (San Antonio, Texas), 2014.
- [59] G. Bir, "Multiblade coordinate transformation and its application to wind turbine analysis," in *ASME Wind Energy Symposium*, (Reno, Nevada), 2008.
- [60] A. Pace, K. Johnson, and A. Wright, "Preventing wind turbine overspeed in highly turbulent wind events using disturbance accommodating control and light detection and ranging," *Wind Energy*, 2014.
- [61] E. A. Bossanyi, *GH Bladed version 3.51 User Manual*. Garrad Hassan and Partners Limited, June 2003. 282/BR/010.

-
- [62] T. J. Larsen and A. M. Hansen, *How 2 HAWC2, the User's Manual*. Technical University of Denmark, December 2007. Ris-R-1597(ver. 3-1).
- [63] F. Oyague, "Gearbox Modeling and Load Simulation of A Baseline 750-kW Wind Turbine using State-of-the-Art Simulation Codes," Tech. Rep. NREL/TP-500-41160, The National Renewable Energy Laboratory, Golden, Colorado, February 2009.
- [64] J. Helsen, F. Vanhollebeke, F. D. Coninck, D. Vandepitte, and W. Desmet, "Insights in wind turbine drive train dynamics gathered by validating advanced models on a newly developed 13.2 MW dynamically controlled test-rig," *Mechatronics*, vol. 21, pp. 737–752, 2011.
- [65] J. Helsen, F. Vanhollebeke, B. Marrant, D. Vandepitte, and W. Desmet, "Multibody modelling of varying complexity for modal behaviour analysis of wind turbine gearboxes," *Renewable Energy*, vol. 36, no. 11, pp. 3098 – 3113, 2011.
- [66] J. L. M. Peeters, D. Vandepitte, and P. Sas, "Analysis of internal drive train dynamics in a wind turbine," *Wind Energy*, vol. 9, no. 1-2, 2006.
- [67] Y. Guo, J. Keller, and R. Parker, "Dynamic analysis of wind turbine planetary gears using an extended harmonic balance approach," in *International Conference on Noise and Vibration Engineering*, pp. 1–18, September 2012.
- [68] Y. Guo and R. G. Parker, "Dynamic modeling and analysis of a spur planetary gear involving tooth wedging and bearing clearance nonlinearity," *European Journal of Mechanics-A/Solids*, vol. 29, no. 6, pp. 1022–1033, 2010.
- [69] M. Todorov, I. Dobrev, and F. Massouh, "Analysis of torsional oscillation of the drive train in horizontal-axis wind turbine," in *8th International Symposium on Advanced Electromechanical Motion Systems Electric Drives Joint Symposium*, pp. 1–7, July 2009.
- [70] Y. Xing and T. Moan, "Multi-body modelling and analysis of a planet carrier in a wind turbine gearbox," *Wind Energy*, vol. 16, no. 7, pp. 1067–1089, 2013.
- [71] Y. Guo, J. Keller, T. Moan, and Y. Xing, "Model fidelity study of dynamic transient loads in a wind turbine gearbox," in *Windpower Conference*, pp. 1–12, May 2013.

- [72] Y. Xing, M. Karimirad, and T. Moan, “Modelling and analysis of floating spar-type wind turbine drivetrain,” *Wind Energy*, vol. 17, no. 4, pp. 565–587, 2014.
- [73] The MathWorks, Inc., *Simscape Users Guide*, March 2012.
- [74] N. Miller, J. J. Sanchez-Gasca, W. Price, and R. Delmerico, “Dynamic modeling of ge 1.5 and 3.6 mw wind turbine-generators for stability simulations,” in *Power Engineering Society General Meeting, 2003, IEEE*, vol. 3, pp. 1977–1983, July 2003.
- [75] MathWorks, “Wind farm (DFIG phasor model).” Available: <http://www.mathworks.com/help/physmod/sps/examples/wind-farm-dfig-phasor-model.html>.
- [76] J. Peeters, *Simulation of dynamic drive train loads in a wind turbine*. PhD thesis, Department of Mechanical Engineering, Katholieke Universiteit Leuven, Leuven, Belgium, June 2006.
- [77] Deutsches Institut für Normung, “*Calculation of Load Capacity of Cylindrical Gears*,” 1987. DIN 3990.
- [78] International Standard, “ISO 6336-1. *Calculation of Load Capacity of Spur and Helical Gears*. Second edition 2006-09-01. Corrected version 2007-04-01.”
- [79] G. Mandic, A. Nasiri, E. Muljadi, and F. Oyague, “Active torque control for gearbox load reduction in a variable-speed wind turbine,” *IEEE Transactions on Industry Applications*, vol. 48, pp. 2424–2432, Nov 2012.
- [80] S. Gade, R. Schlombs, C. Hundedek, and C. Fenselau, “Operational modal analysis on a wind turbine gearbox,” in *Conference & Exposition on Structural Dynamics*, pp. 1–11, 2009.
- [81] J. Lin and R. Parker, “Analytical characterization of the unique properties of planetary gear free vibration,” *Journal of Vibration and Acoustics*, vol. 121, pp. 316–321, 1999.
- [82] R. G. Parker, V. Agashe, and S. M. Vijayakar, “Dynamic response of a planetary gear system using a finite element/contact mechanics model,” *Journal of Mechanical Design*, vol. 122, no. 3, pp. 304–310, 2000.

- [83] J. Lin and R. G. Parker, “Sensitivity of planetary gear natural frequencies and vibration modes to model parameters,” *Journal of Sound and Vibration*, vol. 228, no. 1, pp. 109 – 128, 1999.
- [84] J. Lin and R. G. Parker, “Natural frequency veering in planetary gears,” *Mechanics of Structures and Machines*, vol. 29, no. 4, pp. 411–429, 2001.
- [85] J. Lin and R. G. Parker, “Planetary gear parametric instability caused by mesh stiffness variation,” *Journal of Sound and Vibration*, vol. 249, no. 1, pp. 129 – 145, 2002.
- [86] E. A. Bossanyi, “The design of closed loop controllers for wind turbines,” *Wind Energy*, vol. 3, no. 3, pp. 149–163, 2000.
- [87] E. A. Bossanyi, “Controller for 5mw reference turbine,” Tech. Rep. 11539/BR/04, UpWind, Falmouth, Cornwall, July 2009.
- [88] A. Dixit and S. Suryanarayanan, “Towards pitch-scheduled drive train damping in variable-speed, horizontal-axis large wind turbines,” in *44th IEEE Conference on Decision and Control-European Control Conference*, pp. 1295–1300, Dec 2005.
- [89] Z. Xing, L. Liang, H. Guo, and W. Xiao-Dong, “Damping control study of the drive train of DFIG wind turbine,” in *International Conference on Energy and Environment Technology*, vol. 1, pp. 576–579, Oct 2009.
- [90] M. Molinas, J. Suul, and T. Undeland, “Torque transient alleviation in fixed speed wind generators by indirect torque control with statcom,” in *13th Power Electronics and Motion Control Conference*, pp. 2318–2324, Sept 2008.
- [91] F. Zhang, W. Leithead, and O. Anaya-Lara, “A combined controller design of power system stabilizer and wind turbine drive-train damping filter,” in *International Conference on Sustainable Power Generation and Supply*, pp. 1–6, Sep 2012.
- [92] J. Licari, C. Ugalde-Loo, J. Ekanayake, and N. Jenkins, “Damping of torsional vibrations in a variable-speed wind turbine,” *IEEE Transactions on Energy Conversion*, vol. 28, pp. 172–180, March 2013.

- [93] G. Lalor, A. Mullane, and M. O'Malley, "Frequency control and wind turbine technologies," *IEEE Transactions on Power Systems*, vol. 20, pp. 1905–1913, Nov 2005.
- [94] J. Ekanayake and N. Jenkins, "Comparison of the response of doubly fed and fixed-speed induction generator wind turbines to changes in network frequency," *IEEE Transactions on Energy Conversion*, vol. 19, pp. 800–802, Dec 2004.
- [95] J. Morren, J. Pierik, and S. W. de Haan, "Inertial response of variable speed wind turbines," *Electric Power Systems Research*, vol. 76, no. 11, pp. 980 – 987, 2006.
- [96] M. Kayikci and J. V. Milanovic, "Dynamic contribution of dfig-based wind plants to system frequency disturbances," *IEEE Transactions on Power Systems*, vol. 24, pp. 859–867, May 2009.
- [97] J. Mauricio, A. Marano, A. Gomez-Exposito, and J. Martinez Ramos, "Frequency regulation contribution through variable-speed wind energy conversion systems," *IEEE Transactions on Power Systems*, vol. 24, pp. 173–180, Feb 2009.
- [98] J. Morren, S. W. H. de Haan, W. L. Kling, and J. A. Ferreira, "Wind turbines emulating inertia and supporting primary frequency control," *IEEE Transactions on Power Systems*, vol. 21, pp. 433–434, Feb 2006.
- [99] R. de Almeida and J. Peas Lopes, "Participation of doubly fed induction wind generators in system frequency regulation," *IEEE Transactions on Power Systems*, vol. 22, pp. 944–950, Aug 2007.
- [100] S. Saylors, "Wind parks as power plants," in *2006 IEEE Power Engineering Society General Meeting*, 2006.
- [101] N. Miller and P. Marken, "Facts on grid friendly wind plants," in *2010 IEEE Power and Energy Society General Meeting*, pp. 1–7, July 2010.
- [102] MathWorks, "Wind farm-DFIG detailed model." Available: <http://www.mathworks.com/help/physmod/sps/examples/wind-farm-dfig-detailed-model.html>.

-
- [103] E. Ela, V. Gevorgian, P. Fleming, Y. Zhang, M. Singh, E. Muljadi, A. Scholbrook, J. Aho, A. Buckspan, L. Pao, V. Singhvi, A. Tuohy, P. Pourbeik, D. Brooks, and N. Bhatt, “Active power controls from wind power: Bridging the gaps,” Tech. Rep. NREL/TP-5D00-60574, The National Renewable Energy Laboratory, Golden, Colorado, January 2014.
- [104] X. Yingcheng and T. Nengling, “Review of contribution to frequency control through variable speed wind turbine,” *Renewable Energy*, vol. 36, no. 6, pp. 1671 – 1677, 2011.
- [105] L. Meirovitch, *Fundamentals of vibrations*. Waveland Press, 2010.

List of Publications

The list of publications both journals and conferences papers, derived from the development of the thesis are as follow

Journal Articles

- [J1] I. P. Girsang and J. S. Dhupia, "Collective pitch control of wind turbines using stochastic disturbance accommodating control," *Wind Engineering*, 37 (5): 517-534, October 2013.
- [J2] I. P. Girsang, J. S. Dhupia, E. Muljadi, M. Singh, and J. Jonkman, "Modeling and control to mitigate resonant load in variable-speed wind turbine drivetrain," *IEEE Journal of Emerging and Selected Topics in Power Electronics*, 1 (4): 277-286, December 2013.
- [J3] I. P. Girsang, J. S. Dhupia, E. Muljadi, M. Singh, and L. Y. Pao, "Gearbox and drivetrain models to study dynamic effects of modern wind turbines," *IEEE Transactions on Industry Applications*, 50 (6): 3777-3786, November/December 2014.
- [J4] I. P. Girsang and J. S. Dhupia, "Pitch controller for wind turbine load mitigation through consideration of yaw misalignment," *Mechatronics*, 32: 44-58, December 2015.
- [J5] I. P. Girsang, J. S. Dhupia, and E. Muljadi, "Dynamic loads of variable-speed wind turbine providing inertial response," Submitted to *IEEE Transactions on Energy Conversion*.

Conference Articles

- [C1] I. P. Girsang and J. S. Dhupia, "Performance of linear control methods for wind turbines dealing with unmodeled structural modes," in *Proc. ASME Dynamic Systems and Control Conference*, Fort Lauderdale, Florida, USA, October 2012.

- [C2] I. P. Girsang, J. S. Dhupia, E. Muljadi, M. Singh, and L. Y. Pao, “Gearbox and drivetrain models to study dynamic effects of modern wind turbines,” in Proc. IEEE Energy Conversion Congress and Exposition, Denver, Colorado, USA, September 2013.
- [C3] L. W. Y. Chua, I. P. Girsang, J. S. Dhupia, “Multi-SISO control to regulate constant power and mitigate drive-train load in wind turbine,” in Proc. 3rd IFToMM International Symposium on Robotics and Mechatronics, Singapore, October 2013.
- [C4] I. P. Girsang, J. S. Dhupia, M. Singh, V. Gevorgian, E. Muljadi, and J. Jonkman, “Impacts of providing inertial response on dynamic loads of wind turbine drivetrains,” in Proc. 2014 IEEE Energy Conversion Congress and Exposition, Pittsburgh, Pennsylvania, USA, September 2014.
- [C5] I. P. Girsang and J. S. Dhupia, “Pitch control for wind turbine in yawed inflow condition,” in Proc. 2014 ASME Dynamic Systems and Control Conference, San Antonio, Texas, USA, October 2014.
- [C6] I. P. Girsang and J. S. Dhupia, “Pitch control strategies considering yaw misalignment for wind turbine load mitigation,” Submitted to 2015 IEEE Conference on Decision and Control.

Technical Report

- [T1] M. Singh, E. Muljadi, J. Jonkman, V. Gevorgian, I. Girsang, and J. Dhupia. Simulation for wind turbine generator - with FAST and MATLAB/Simulink modules. National Renewable Energy Laboratory, Golden, Colorado, USA, Tech. Rep. NREL/TP-5500-59195.